INVESTIGATION OF ELECTRICAL CONDUCTIVITY CHARACTERISTICS AT THE VICINITY OF GANOS FAULT, NORTHWEST TURKEY BY MAGNETOTELLURICS

by
Mustafa Karaş
B.S., Geophysical Engineering, Istanbul Technical University, 2014

Submitted to Kandilli Observatory and Earthquake
Research Institute in partial fulfillment of
the requirements for the degree of
Master of Science

Graduate Program in Geophysics
Boğaziçi University
2017

INVESTIGATION OF ELECTRICAL CONDUCTIVITY CHARACTERISTICS AT THE VICINITY OF GANOS FAULT, NORTHWEST TURKEY BY MAGNETOTELLURICS

APPROVED BY:

Assoc. Prof. Dr. S. Bülent Tank ....
(Thesis Supervisor)

Prof. Dr. Hayrullah Karabulut ....

Prof. Dr. Aysan Gürer ....
(Istanbul University)

DATE OF APPROVAL: 07.06.2017

Dedicated to my mother

ACKNOWLEDGEMENTS

Firstly, I wish to thank my supervisor Assoc. Prof. Dr. S. Bülent Tank who gave me the opportunity to study magnetotellurics in my graduate education. He did not only support or guide me during this study, but also showed me how a scientist should be. I am grateful to him for his encouragement about this project, spending time with me in the field, during data acquisition and helps for discussing data.

I thank my friends and colleagues at Boğaziçi University, KOERI and Istanbul Technical University, Department of Geophysical Engineering, particularly Sinan Özaydın for his valuable support. Assist. Prof. Dr. Tuna Eken has always been supportive to this project and I would like to thank him for encouraging comments.

Prof. Dr. Aral I. Okay is sincerely thanked for fruitful discussions about the subject and reviewing the publication produced from this thesis.

I want to thank Prof. Weerachai Siripunvaraporn and Prof. Dr. Gary Egbert for providing the 3D inversion codes. Strike code is provided by Prof. Dr. Alan G. Jones. MTpy package was extensively used during the study. I am grateful Dr. Lars Krieger and Jared R. Peacock for their support.

This research was financially supported by Boğaziçi University, Scientific Research Projects (BAP) (No:10080). The preliminary results of this study were presented at EGU 2016 General Assembly in Vienna and 23th Electromagnetic Induction Workshop 2016 in Chiang Mai, Thailand. The travel and accommodation supports were provided by Istanbul Technical University, Faculty of Mines for both organizations.

I have to express my greatest gratitude to my beloved mother, Güler Karaş. Without her patience and support, none of my works even this thesis could not be possible. I will always be grateful for her dedication to my education. I am also grateful to my entire family for their support and encouragement during this study.

Finally, Aysu Ceren Okur deserves a special thank for her support and encouragement during my thesis. More than a friend, she always inspired me as an enviable scientist. I cannot thank Aysu enough for the meaning she brings to my life.

ABSTRACT

INVESTIGATION OF ELECTRICAL CONDUCTIVITY CHARACTERISTICS AT THE VICINITY OF GANOS FAULT, NORTHWEST TURKEY BY MAGNETOTELLURICS

As constituting the westernmost end of North Anatolian Fault, 45-km-long Ganos Fault acts as an active segment which represents a seismic gap. In this thesis, the first systematic magnetotellurics observations are made to reveal the electrical conductivity characteristics of locked Ganos Fault. Near the epicenter of last major event, 1912 Mürefte Earthquake; audiomagnetotelluric (AMT) data were collected through north-south aligned almost-continuous profile including twelve stations to decipher the shallow conductivity structure. Then, thirteen wide-band magnetotellurics (MT) stations surrounding the AMT profile as a grid were installed to investigate deeper structure. The dimensionality analyses performed on both AMT and wide-band MT datasets indicate a considerable agreement with previous geological and seismological observations. While the geo-electric strike angles were determined with Swift's method following Groom and Bailey decomposition, they were also calculated with phase tensor analyses independently. Both methods confirm each other and verified the strike directions as ∼N70°E for the AMT and ∼N60°E for wide-band MT data. Two- (Rodi and Mackie, 2001) and three-dimensional (Siripunvaraporn et al., 2005; Egbert and Kelbert, 2012) numerical modeling routines were used for inverse modeling. All modeling attempts illustrate highly conductive anomalies representing so-called "fault zone conductors" along the Ganos Fault. Three-dimensional models indicate that fluctuations in spatial extents of the FZC are observed along the fault. Subsidiary oblique faults around Ganos Fault which are represented as conductive structures with individual mechanically weak features merge in a greater damage zone and they constitute a wide fluid bearing environment. By concentrating on the southern side of the fault, the damage zone shows an asymmetry around main fault strand, which exhibits a distributed conduit behavior for fluid flow. A highly resistive block represents the ophiolitic basement beneath younger formations at a depth of 2 km, where the mechanically weak to strong transition occurs. Below this transition, the overt resistive structures at both side of the fault imply that the absence of fluid pathways through the seismogenic zone might be related to lack of seismicity in the region.

ÖZET

GANOS FAYI VE ÇEVRESİNİN ELEKTRİK İLETKENLİK YAPISININ MANYETOTELLÜRİK YÖNTEM İLE İNCELENMESİ

Kuzey Anadolu Fayı'nın en batıdaki kesimini oluşturan 45 km uzunluğundaki Ganos Fayı sismik boşluk olarak değerlendirilen aktif bir segmenttir. Bu tez çalışmasında, elektrik iletkenlik yapısının araştırılması amacıyla Ganos Fayı üzerindeki ilk sistemli manyetotellürik gözlemler gerçekleştirilmiştir. Bölgedeki son önemli aktivite olan 1912 Mürefte Depremi'nin merkez üssü yakınlarında, 12 istasyondan oluşan sürekli bir profil boyunca yüksek-frekanslı manyetotellürik yöntem (AMT) ölçümleri yapılarak, sığ elektrik iletkenlik yapısı incelenmiştir. Sonraki aşamada, AMT profilini çevreleyecek şekilde yerleştirilen 13 istasyonluk geniş-bant manyetotellürik (MT) ağı ile daha derin yapının ortaya çıkarılması amaçlanmıştır. Her iki veri kümesine de uygulanan boyutluluk analizleri, daha önce ortaya konulmuş olan jeolojik ve sismolojik gözlemlerle uyumlu sonuç vermiştir. Groom-Bailey dekompozisyonunu takiben uygulanan Swift metodu ile bulunan doğrultu açıları, faz tensörü analizi ile de ayrıca hesaplanmıştır. Her iki yöntem de birbirini doğrularken, doğrultu açıları AMT verisi için $\sim$K70^{o}D, geniş-bant MT verisi için $\sim$K60^{o}D olarak tespit edilmiştir. Ters çözüm modelleme çalışmaları iki- (Rodi ve Mackie, 2001) ve üç-boyutlu (Siripunvaraporn ve diğ., 2005; Egbert ve Kelbert, 2012) sayısal modelleme rutinleri ile gerçekleştirilmiştir. Bütün modelleme sonuçları, Ganos Fayı boyunca uzanan bir fay zonu iletkeninin varlığını işaret etmektedir. Üç-boyutlu modeller, fay zonu iletkeni boyutlarının fay boyunca kısa mesafelerde bile ani değişimler gösterdiğini işaret etmektedir. Ganos Fayı'nın çevresinde yer alan oblik tali faylar iletken yapılar olarak gözlenirken, neden oldukları birbirinden bağımsız zayıflık bölgeleri birleşerek sıvı ihtiva eden geniş bir hasar bölgesi oluşturmaktadır. Fayın güney

kesiminde yoğunlaşan bu hasar bölgesi asimetrik davranış göstererek, fayın dağınık geçirgen bir yapıya sahip olduğunu ortaya koymaktadır. Oldukça yalıtkan olduğu gözlenen ofiyolitik temel, genç formasyonların altında 2 km derinliğine kadar ulaşarak mekanik açıdan zayıf bir ortamdan güçlü bir ortama geçildiğini göstermektedir. Bu geçiş bölgesinin altında, fayın her iki yanında yer alan yalıtkan yapılar, sıvıların sismojenik zondan yukarı taşınmasına izin vermeyerek, bölgedeki sismik aktivite eksikliğinin sebebi olma ihtimalini taşımaktadır.

TABLE OF CONTENTS

LIST OF FIGURES

LIST OF TABLES

LIST OF SYMBOLS

$\mathbf{A}$	Local Anisotropy
$\mathbf{B}$	Magnetic flux density
C	Schmucker–Weidelt transfer function
$\mathbf{C}_d$	Data covariance matrix
$\mathbf{C}_m$	Model covariance matrix
$\mathbf{d}$	Data parameters
$\mathbf{D}$	Electric displacement
$\mathbf{D}'$	Distortion matrix
$\mathbf{D}_p$	Predicted data
e	Error
$\mathbf{E}$	Electric field
f	Frequency
F	Forward modeling function
g	Site gain
$\mathbf{H}$	Magnetic field
$\mathbf{J}$	Conduction current density
k	Wave number
$\mathbf{m}$	Model parameters
M_w	Moment Magnitude
q	Density of electric charge
$\mathbf{R}$	Rotation matrix
$\mathbf{S}$	Shear
T	Period
$\mathbf{T}$	Twist
$\mathbf{T}_x,\ \mathbf{T}_y$	Tipper functions
Vp/Vs	P- and S-wave velocity ratio
$\mathbf{X}$	Real part of impedance tensor
$\mathbf{Y}$	Imaginary part of impedance tensor

$\mathbf{Z}$	Impedance

α	Non-invariant angle
α'	Horizontal smoothing parameter
β	Skew angle
δ	Skin depth
ε	Electric permittivity
κ	Skew
μ	Magnetic permeability
μ_0	Magnetic permeability of free space
ρ	Resistivity
ρ_{app}	Apparent resistivity
λ	Smoothing (trade-off) parameter
σ	Electric conductivity
τ	Regularization parameter
ϕ	Phase
Φ	Phase tensor
ω	Angular frequency

LIST OF ACRONYMS/ABBREVIATIONS

AMT	Audiomagnetotellurics
CF	Carboneras Fault
EAF	East Anatolian Fault
FZC	Fault zone conductor
GB	Groom and Bailey decomposition
GF	Ganos Fault
IAF	İzmit-Adapazarı Fault
IMF	İznik-Mekece Fault
Hz	Hertz
MT	Magnetotellurics
NAF	North Anatolian Fault
NLCG	Non-linear conjugate gradient
PF	Punchbowl Fault
SAF	San Andreas Fault
TE	Transverse electric
TM	Transverse magnetic

1. INTRODUCTION

Ganos Fault (GF) is the westernmost part of the 1200-km-long-dextral North Anatolian Fault (NAF) (Şengör et al., 2005). This active segment is the northernmost branch of NAF which shows a relatively complex structure after reaching the Marmara Sea near İzmit. While acting as a seismic gap, GF exits the sea near Gaziköy, Tekirdağ and then, it vanishes again in the Saros Bay. This particular 45 km segment produced the M_w 7.4 Şarköy-Mürefte earthquake in 1912 (Ambraseys and Finkel, 1987; Ambraseys, 2002). Since major activities along NAF have occurred with centennial cycles in the history, they showed a strong tendency to propagate from east to west (Parsons et al., 2000; Şengör et al., 2005). After the disastrous 1999 İzmit and Düzce earthquakes, there is a consensus among the geoscience community that the next important event is expected on the western part of NAF, especially on segments within the Marmara Sea and/or GF (Şengör et al., 2005).

Previously; geological, geodetic and seismological studies were performed to decipher the nature of GF (Okay et al., 1999; Rockwell et al., 2001; Yaltırak and Alpar, 2002; Okay et al., 2004; Seeber et al., 2004; Motagh et al., 2007; Janssen et al., 2009; Okay et al., 2010; Özcan et al., 2010; Öztürk et al., 2015). Although the fault-fluid relations at GF was examined as well as its tectonic evolution, morphological and structural properties; a detailed electrical resistivity structure is still undetermined due to absence of detailed surveys.

With the aim of revealing the shallow and deep electrical characteristic of active and fossil fault zones, magnetotelluric (MT) method yields valuable results with its practicality and efficiency (Unsworth et al, 1997; Bedrosian et al., 2002; 2004; Becken et al., 2008; 2011; Wannamaker et al., 2009; Meqbel et al., 2016). This geophysical tool utilizes the naturally occurring electromagnetic fields to investigate the electrical properties of the subsurface. By the way of ionic transfer; saline fluids, brines, meteoric water, metamorphic fluids and partial melts impose fluid interconnection within the crust and upper mantle which can be sensitively identified by the MT method (Becken and Ritter, 2012). The electrical conductivity values are highly increased by the pore fluids, and become convenient to be explored with the MT at the vicinity of fault zones (Unsworth and Bedrosian, 2004). Another mechanism is electronic transfer which suggests the transfer of electrical currents through metallic ores (such as graphites and sulfides) (Jödicke, 1992).

Presence of hydraulic conduits determines the mechanism behind fracturing processes since fluid invasion has important impact on rheological properties of upper crustal structures within the scale range between fissured rocks to large faults (Zhang et al., 2002). New stress elements are imposed by intrusion of fluids into fault zones, thus a region can become seismically activated through changing rheological, chemical and frictional properties (Hickman et al., 1995). This mutual effect between seismicity and fluid intrusion triggers an ongoing and evolving deformation. It shapes the internal geometry of a fault zone, where fluid presence is established by structures with relevant permeability. Depending on petrological properties of its protolith (Evans, 1990), spatial variations of the fault's core and damage zone can be categorized with four end-member fault zone architectural styles. This end-members are localized barrier, localized conduit, distributed conduit and combined conduit-barrier. By considering any physical example with this categorization, a description of a qualitative position can be made. Defining a ratio of fault zone components determines the faults fluid flow behavior which changes between these end-members (Caine et al., 1996).

MT method has proved its capability to imaging highly conductive regions at the vicinity of fault zones which are often called as "fault zone conductors" (FZC) (Unsworth et al., 1997; 1999; 2000, Bedrosian et al., 2002; 2004 Ritter et al., 2005, Becken et al., 2012). Initially, "Electromagnetic Research Group for the Active Fault" (1982) successfully complete the first observations on a fault zone regarding its high conductivity at Yamasaki Fault, Japan. The first systematic MT observations were made by Unsworth et al., (1997; 2000) to identify a possible conductive zone located on the partly (surface to 3 km) creeping segment of San Andreas Fault (SAF), north of Parkfield, California. At these studies, they made the definition of the FZC and linked the established FZC to saline fluid bearing porous formations. According to Unsworth et al., (1997; 2000) these anomalous features found near Parkfield do not correspond to seismic activity and favors fault-weakening behavior of fluids at such depths. Additionally, central creeping segment of SAF at Hollister was also investigated with the MT method. In Hollister, corresponding resistivity structures were well-correlated with high Vp/Vs ratios, which is another indicator of the fluid presence at a fault zone (Bedrosian et al., 2002; 2004). Moreover, earthquakes may be triggered by another fluid invasion mechanism rather than stimulus of creeping motion within much greater depths and relevantly particular rheological environments. Becken et al. (2011) subsequently pictured the highly conductive zone which is related with dehydration of a serpentinite mantle wedge beneath Parkfield and Cholame region where non-volcanic tremor events are intensified. Lateral fluid pathways through the seismogenic zone of SAF were interpreted as hydraulic fracturing caused by super-hydrostatic pressure. This result agrees with the previous studies and suggests that the seismicity at Parkfield is fluid-driven (Thomas et al, 2009) with very precise recurrent events (Johnson and McEvilly, 1995). This situation highlights the importance of revealing the origins of the fluid flux, either meteoric or metamorphic (Irwin and Barnes, 1975; Byerlee, 1993). On the other hand, MT studies clarifies that high resistivity structures on both sides of the fault that are corresponding to mechanically strong formations are located at the vicinity of a locked fault (Unsworth et al., 1999; Goto et al., 2005). When they are compared with weaker faults, FZC at locked faults are relatively small and they have low lateral-conductance values (Hoffmann-Rothe et al., 2004). Unsworth et al. (1999) directly made this comparison between locked Carizzo Plain and Parkfield. Since GF is known as a seismically inactive segment, one might expect similar attributes which are seen in the previous examples.

MT studies with an aim to decipher electrical resistivity structures along NAF were performed multiple times (Honkura et al., 2000; 2013; Oshiman et al., 2002; Tank et al., 2003; 2005; Tank, 2012; Türkoğlu et al., 2008; Kaya et al, 2009; 2013). In this thesis, the first detailed magnetotelluric data which particularly concentrated on Ganos region were collected to be analyzed with two- and three-dimensional numerical modeling routines. To portray a comprehensive picture of the area, the study was carried out by acquisition of data in high frequencies within shorter time intervals (2-3 hours, audiomagnetotellurics (AMT)) and mid-range frequencies within relatively longer time intervals (18 hours - 27 hours, wide-band MT). Here, electrical resistivity structure of GF is examined on the basis of several data analysis techniques and modeling results in order to achieve a more accurate interpretation for geological and rheological properties of the region.

The theoretical information about MT method and steps of application are introduced in the following chapter. The sources of MT method, basic concepts, dimensionality and theory of data processing are also presented in Chapter 2. Chapter 3 describes the study field in the light of detailed information about tectonic setting and geology. Starting from data acquisition, all data processing stages are given in Chapter 4. This chapter includes every step that are mentioned in Chapter 2. Then, the outcomes of dimensionality analyses and resistivity models are interpreted in the Chapter 5 to present a new physical approach to the area of interest. Finally, to complete this thesis, the results are briefly summarized in Chapter 6.

2. THEORY OF MAGNETOTELLURICS

2.1. Introduction

Magnetotelluric (MT) method is a passive source geophysical technique which depends on measuring the variations of natural electric and magnetic field from the surface of Earth. Magnetotelluric method aims to reveal the electrical characteristic of Earth at a wide range of depth. The basis of magnetotelluric theory was independently explained by Rikitake (1948), Tikhonov (1950) and Cagniard (1953) as electrical conductivity can be determined by comparison of simultaneously-measured electric and magnetic fields. All of these studies were based on Maxwell equations and clarified that extended sounding periods provide deeper electromagnetic responses. This principle is called as “electromagnetic skin depth” and approximately gives the depth where amplitudes of electromagnetic fields at the surface decreases to e^{-1} of it as in the terms of the sounding period, T and the average resistivity of medium ρ_{app}:

$$\delta \cong 503.2(\mathrm{T}\rho_{app})^{\frac{1}{2}} \tag{2.1}$$

This relation between the depth and sounding period overcomes the limitations of active source geophysical methods. Electromagnetic fields which are utilizable for magnetotelluric method can range between 10^{-3} and 10^{5} seconds and create a potential to investigate hundreds of kilometers depth.

Electromagnetic fields can arise from two origins. Electromagnetic fields with periods longer than 1 second are originated by interaction between solar wind and the magnetosphere of the Earth. Solar wind causes variations in the magnetosphere while facing to magnetopause that is the boundary of magnetosphere and these variations generate magnetic and electric fields. These fields must penetrate into ionosphere before reaching the surface of the Earth so they expose to modifications which cause to generate the new magnetic and electric fields inside the Earth.

On the other hand, meteorological activities are the second source of electromagnetic fields which are related with audiomagnetotellurics (AMT). Electromagnetic fields with periods shorter than 1 second, are generally created by lightning discharges. In every seconds approximately hundreds of lightning occur all around the world, especially in equatorial regions.

Activities on the magnetosphere and the ionosphere cause time-dependent alterations on the Earth's magnetic field. These natural alterations induce telluric currents in the conductive body of the Earth. This induction mechanism is triggered by attenuation of electromagnetic fields which are assumed as plane waves (Cagniard, 1953). Despite plane wave assumption was discussed by Wait (1952) and Price (1962), Madden and Nelson (1964) showed the validity of the assumption at mid-latitudes for periods less than 10^4 seconds.

Depending on the electrical conductivity properties of the materials at the crust and mantle, MT method can provide information about geo-electric structure even down to core-mantle boundary of the Earth (Rikitake, 1966; Bott 1982). Beyond active electromagnetic methods, covering a broad range of depth provides an advantage to MT method for exploring numerous geological and structural environments. According to progress on the last four decades, widespread and successful applications of the method prove the reliability of magnetotellurics. Books focus on magnetotellurics can provide detailed information about the theory and application of the method (Kaufmann and Keller, 1981; Berdichevsky and Zhdavov, 1984; Vozoff, 1991; Zhdanov and Keller, 1994; Simpson and Bahr, 2005; Chave and Jones, 2012).

2.2. Principles of Magnetotellurics

2.2.1. Maxwell Equations

Maxwell Equations can be used for describing propagation of electromagnetic waves in the atmosphere and the Earth:

$$\nabla \times \mathbf{E} = \frac{-\partial \mathbf{B}}{\partial t} \tag{2.2}$$

$$\nabla \times \mathbf{H} = \mathbf{J} + \frac{\partial \mathbf{D}}{\partial t} \tag{2.3}$$

$$\nabla \cdot \mathbf{B} = 0 \tag{2.4}$$

$$\nabla \cdot \mathbf{D} = q \tag{2.5}$$

where **E** is the electric field (in Vm^{-1}), **B** is the magnetic flux density (in T), **H** is the magnetic field (in Am^{-1}), **J** is the conduction current density (in Am^{-2}), **D** is the electric displacement (in Cm^{-2}) and q is the density of electric charges (in Cm^{-3})(Ward and Hohmann, 1987).

First equation (2.2) is the mathematical presentation of the Faraday's Law, which states that a time-varying magnetic flux induce an electric field. Second equation (2.3) is the Ampere's Law with the Maxwell's correction of displacement current term. This equation gives the relation between a current and proportional magnetic field to the total flow. The third (2.4) and fourth (2.5) equations are the magnetic and the electric laws of Gauss. While third equation states that no magnetic monopole exists, fourth equation explains that electric charges emit electric field.

Three material equations which define a homogeneous and isotropic medium are necessary to solve Maxwell equations:

$$\mathbf{B} = \mu \mathbf{H} \tag{2.6}$$

$$\mathbf{D} = \varepsilon \mathbf{E} \tag{2.7}$$

$$\mathbf{J} = \sigma \mathbf{E} \tag{2.8}$$

where μ is the magnetic permeability (in Hm^{-1}), ε is the electric permittivity (in Fm^{-1}) and σ is the electric conductivity (in Sm^{-1}). By using the material equations, first and second equations of Maxwell can be written in a form of

$$\nabla \times \mathbf{E} = -\mu \frac{\partial \mathbf{H}}{\partial t} \tag{2.9}$$

$$\nabla \times \mathbf{H} = \sigma \mathbf{E} + \varepsilon \frac{\partial \mathbf{E}}{\partial t} \tag{2.10}$$

By applying vector identity

$$\nabla \times \nabla \times \mathbf{A} = \nabla(\nabla \cdot \mathbf{A}) - \nabla \cdot \nabla \mathbf{A} = \nabla\nabla \cdot \mathbf{A} - \nabla^2 \mathbf{A} \tag{2.11}$$

and assuming that there are no free charges within the Earth

$$\nabla \cdot \mathbf{E} = 0 \tag{2.12}$$

after taking the curl of equations (2.9) and (2.10), they can be written as Helmholtz Equations

$$\nabla^2\mathbf{E} = \mu\frac{\partial}{\partial t}(\nabla\times\mathbf{H}) = \mu\sigma\frac{\partial\mathbf{E}}{\partial t} + \varepsilon\mu\frac{\partial^2\mathbf{E}}{\partial t^2} \tag{2.13}$$

$$\nabla^2\mathbf{H} = -\sigma(\nabla\times\mathbf{E}) - \varepsilon\frac{\partial}{\partial t}(\nabla\times\mathbf{E}) = \mu\sigma\frac{\partial\mathbf{H}}{\partial t} + \varepsilon\mu\frac{\partial^2\mathbf{H}}{\partial t^2} \tag{2.14}$$

Assuming that a surface amplitudes of a plane wave is $\mathbf{E}_0$ and $\mathbf{H}_0$ and it has a harmonic time dependence as $e^{-i\omega t}$, the Helmholtz Equations can be evaluated as:

$$\nabla^2\mathbf{E} = i\omega\mu\sigma\mathbf{E} - \omega^2\varepsilon\mu\mathbf{E} \tag{2.15}$$

$$\nabla^2\mathbf{H} = i\omega\mu\sigma\mathbf{H} - \omega^2\varepsilon\mu\mathbf{H} \tag{2.16}$$

High conductivity contrast between air and Earth causes reflection of majority of incident waves and only a few number of waves penetrate into conductive Earth. Because of displacements currents are very small when compared to conductivity currents ($\omega^2\varepsilon\mu \ll i\omega\mu\sigma$), they can be neglected at lower frequencies. Then electromagnetic induction in the Earth is carried out by diffusion process and Helmholtz Equations can be considered as diffusion equations

$$\nabla^2\mathbf{E} = i\omega\mu\sigma\mathbf{E} \tag{2.17}$$

$$\nabla^2\mathbf{H} = i\omega\mu\sigma\mathbf{H} \tag{2.18}$$

2.2.2. Concepts of Skin Depth and Transfer Function

A uniform half-space underlying an air layer with zero conductivity can be used as a reasonable model to understand concepts of penetration depth and impedance. A plain electromagnetic wave which penetrates the half-space vertically has an angular frequency as $\omega = 2\pi f$. While the electric field is polarized in the x-direction, derivatives of $\mathbf{E}_x$ respect to x- and y-directions is zero. Then equation (2.16) can be written as

$$\frac{\partial^2 \mathbf{E}_x}{\partial z^2} = -i\omega\mu\sigma \mathbf{E}_x(z) \tag{2.19}$$

The general solution for the equation (2.18) is

$$\mathbf{A}k^2 e^{kz} = -i\omega\mu\sigma \mathbf{A}e^{kz}(z) \tag{2.20}$$

If $k^2 = -i\omega\mu\sigma$, the equation (2.20) is satisfied and there are positive and negative square roots can be found in the solution.

$$\mathbf{E}_x(z) = \mathbf{E}_1 e^{-kz} + \mathbf{E}_2 e^{+kz} \tag{2.21}$$

$\mathbf{E}_1$ and $\mathbf{E}_2$ are constant values and k is named as wave number. While depth variation goes to infinity in vertical direction, $\mathbf{E}_x(z)$ must be bounded. This situation causes the elimination of the positive component and the equation can be given as

$$\mathbf{E}_x(z) = \mathbf{E}_1 e^{-kz} \tag{2.22}$$

by replacing wave number:

$$\mathbf{E}_x(z) = \mathbf{E}_1 e^{-(1-i)\sqrt{\frac{\omega\mu\sigma}{2}}z} \tag{2.23}$$

So the electromagnetic skin depth can be determined by using the real part of wave number as

$$\delta = \sqrt{\frac{2}{\omega \mu_0 \sigma}} \tag{2.24}$$

where it can be used in more practical manner with the terms of sounding period and apparent resistivity as given at equation (2.1).

The inverse of wave number is named as the Schmucker - Weidelt transfer function (Weidelt,1972; Schmucker 1973) and given as

$$C = \frac{1}{k} = \frac{\delta}{2} - \frac{i\delta}{2} \tag{2.25}$$

C is also frequency dependent and has dimensions of length as skin depth but it is given with a complex value. The magnitudes of real and imaginary parts of C is equal in a uniform half-space. The transfer function is a term that describes the linear relationship between the observed physical parameters. By applying equations (2.2) and (2.22)

$$\frac{\partial \mathbf{E}_x}{\partial z} = -\frac{\partial \mathbf{B}_y}{\partial t} = -i\omega \mathbf{B}_y = -k\mathbf{E}_x \tag{2.26}$$

Thus measured $\mathbf{E}_x$ and $\mathbf{B}_y$ values can be used for calculating C in frequency domain

$$C = \frac{\mathbf{E}_x}{i\omega \mathbf{B}_y} = -\frac{\mathbf{E}_y}{i\omega \mathbf{B}_x} = \frac{1}{k} \tag{2.27}$$

On the other hand, the electrical resistivity of a uniform half-space can also be calculated from a certain transfer function (Simpson and Bahr, 2005)

$$\rho = \frac{1}{\sigma} = \frac{1}{|k|^2}\mu_0 \omega = |C|^2 \mu_0 \omega \tag{2.28}$$

2.2.3. Multilayered Half-space: The Concepts of Apparent Resistivity and Phase

In a multilayered half-space, every layer is represented with a diffusion equation which contains the conductivity value of the layer (σ_n). However, each layer has a definite depth in that model and all components of equation (2.21) are included in calculation. For an nth layered model, transfer function of each layer is given as

$$C_n(z) = \frac{\mathbf{E}_{xn}(z)}{i\omega\mathbf{B}_{yn}(z)} \tag{2.29}$$

where the wave number is $k = \sqrt{i\mu\sigma_n\omega}$. Multilayered half-space is a more realistic model to illustrate electrical characteristic of the Earth rather than uniform half-space. From bottom to top, resistivity of each layer can be calculated by Wait's recursion formula (Wait, 1954)

$$C_n(z_{n-1}) = \frac{1}{k_n}\frac{k_nC_{n+1}(z_n) + tanh(k_nl_n)}{1 + k_nC_{n+1}(z_n) + tanh(k_nl_n)} \tag{2.30}$$

here l_n is $z_n - z_{n-1}$ (Simpson and Bahr, 2005). Due to determine equation (2.29) the transfer function the lowermost layer should be defined as a uniform half-space by using equation (2.27). Therefore, equation (2.30) will be applied n-1 times to achieve the transfer function at the surface of the model.

The average resistivity of an equivalent uniform half-space which is calculated from transfer function is called as apparent resistivity

$$\rho_{app}(\omega) = |C(\omega)|^2\,\mu_0\omega \tag{2.31}$$

Generally in MT community, the ratio of $\mathbf{E}_x$ and $\mathbf{B}_x$ which is named as electromagnetic impedance in frequency domain is used instead of C and the relationship between C

and the impedance is

$$\mathbf{Z} = \frac{\mathbf{E}_x}{\mathbf{H}_y} = \frac{\mu_0 \mathbf{E}_x}{\mathbf{B}_y} = i\omega\mu_0 C \tag{2.32}$$

While resistivity of a uniform half-space can be calculated with impedance as

$$\rho = \frac{1}{\mu_0 \omega} |\mathbf{Z}|^2 = \frac{0.2}{f} \left| \frac{\mathbf{E}_x}{\mathbf{B}_y} \right|^2 \tag{2.33}$$

this equation is named as "Cagniard-Tikhonov formula" and apparent resistivity is presented by

$$\rho_{app}(\omega) = \frac{0.2}{f} \left| \frac{\mathbf{E}_x(\omega)}{\mathbf{B}_y(\omega)} \right|^2 \tag{2.34}$$

Impedance phase is another parameter which can be utilized by using the complexity of transfer function. The phase difference between $\mathbf{E}_x$ and $\mathbf{B}_y$ is calculated as

$$\phi = arg(\mathbf{Z}) \tag{2.35}$$

and it can be written as

$$\phi_{1\text{-}D} = tan^{-1}(\frac{\mathbf{E}_x}{\mathbf{B}_y}) \tag{2.36}$$

for a uniform half-space which can be considered as one-dimensional earth model.

Due to real and imaginary components of impedance equal to each other the phase value is 45° in a uniform half-space. While values larger than 45° represent increasing resistivity with the depth, impedance phase indicates decrease in resistivity values if being less than 45° (Vozoff, 1991; Simpson and Bahr, 2005).

2.2.4. Two-dimensional Earth Model

For a uniform or multilayered half-space, components of impedance will be equal to each other in the one-dimensional resistivity model due to their orthogonality. However, there is a need of more complicated model to define the real cases in the Earth. A vertical discontinuity which juxtaposes two structures with different electrical resistivity values is a simple example to two-dimensional model (Figure 2.1). Induction at such a discontinuity is based on conservation of current. The current density is determined as

$$\mathbf{J}_y = \sigma \mathbf{E}_y \tag{2.37}$$

at the boundary. Due to the conservation of the current, chancing conductivity requires a discontinuity at the electric field while the rest of electromagnetic fields are continuous.

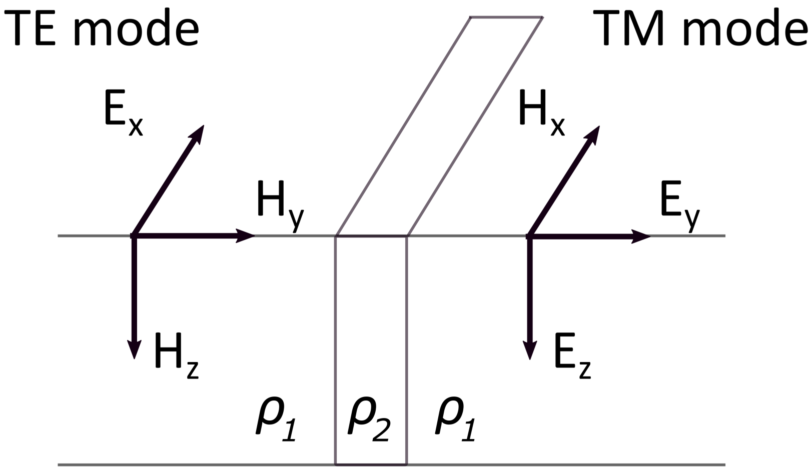

Figure 2.1. Representation of the modes for two-dimensional Earth model.

For an optimum two-dimensional model, two different modes yielded due to orthogonality between electric and magnetic fields. In the first mode electric field is parallel to discontinuity and it is perpendicular in the second one. These modes can be specified by using the terms of Maxwell equations.

When electric current flows parallel to discontinuity, electric field is parallel and magnetic field is perpendicular to the strike. This case is named as TE mode (**E**-polarization, transverse electric) and defined with equations of

$$\frac{\partial \mathbf{E}_x}{\partial y} = \frac{\partial \mathbf{B}_z}{\partial t} = i\omega \mathbf{B}_z$$

$$\frac{\partial \mathbf{E}_x}{\partial z} = \frac{\partial \mathbf{B}_y}{\partial t} = -i\omega \mathbf{B}_y \tag{2.38}$$

$$\frac{\partial \mathbf{B}_z}{\partial y} - \frac{\partial \mathbf{B}_y}{\partial t} = \mu_0 \sigma \mathbf{E}_x$$

In the other mode where electric current flows perpendicular to discontinuity, magnetic field is parallel and electric field is perpendicular to the strike. This case is named as TM mode (**B**-polarization, transverse electric) and defined with equations of

$$\frac{\partial \mathbf{B}_x}{\partial y} = \mu_0 \sigma \mathbf{E}_z$$

$$-\frac{\partial \mathbf{B}_x}{\partial t} = \mu_0 \sigma \mathbf{B}_y \tag{2.39}$$

$$\frac{\partial \mathbf{E}_z}{\partial y} - \frac{\partial \mathbf{E}_y}{\partial z} = i\omega \mathbf{B}_x$$

Therefore, the impedances including term of $\mathbf{E}_y$ will be discontinuous and the non-zero component in a basic two-dimensional model causes a discontinuity in calculated apparent resistivity values after applying equation (2.31). As a result of this, resistivity values achieved from TM mode are more efficient to detect lateral conductivity changes while TE mode responds vertical boundaries more sensitively.

2.2.5. Impedance Tensor

All horizontal components of observed electromagnetic fields can be represented with a complex impedance tensor in magnetotellurics:

$$\begin{bmatrix} \mathbf{E}_x \\ \mathbf{E}_y \end{bmatrix} = \begin{bmatrix} \mathbf{Z}_{xx} & \mathbf{Z}_{xy} \\ \mathbf{Z}_{yx} & \mathbf{Z}_{yy} \end{bmatrix} \begin{bmatrix} \mathbf{B}_x \\ \mathbf{B}_y \end{bmatrix} \tag{2.40}$$

Beside its function at calculation of apparent resistivity and phase, impedance tensor also provides information about strike direction and dimensionality. For a one-dimensional Earth model, diagonal elements of impedance tensor are zero and off-diagonal elements have same magnitudes with opposite signs.

$$\mathbf{Z}_{xx} = \mathbf{Z}_{yy} = 0 \text{ and } \mathbf{Z}_{xy} = -\mathbf{Z}_{yx} \tag{2.41}$$

For two-dimensional Earth model, conductivity values also chance along one of the horizontal directions besides the depth. In this case diagonal elements of impedance tensor have same magnitudes with opposite signs and off-diagonal elements are completely different from each other.

$$\mathbf{Z}_{xx} = -\mathbf{Z}_{yy} \text{ and } \mathbf{Z}_{xy} \neq \mathbf{Z}_{yx} \tag{2.42}$$

Even if the observations are made through the strike direction or impedance rotation is applied, the diagonal elements will become zero and off-diagonal elements will correspond to TE and TM modes, respectively.

For three-dimensional Earth model which is most realistic case, all elements of impedance tensor are different from each other and zero.

$$\mathbf{Z}_{xx} \neq \mathbf{Z}_{xy} \neq \mathbf{Z}_{yx} \neq \mathbf{Z}_{yy} \tag{2.43}$$

In this case, conductivity values change in all directions and the impedance tensor cannot be mathematically rotated reducing diagonal elements to zero.

2.3. Dimensionality

2.3.1. Skew

Dimensionality of MT data can be determined by applying different mathematical approaches. Analyzing the impedance tensors provide the information about which interpretation technique is required for the data. Skew is a parameter which is derived to examine the dimensionality of a given frequency. It is calculated with a basic relationship between the diagonal and off-diagonal components of the impedance tensor

$$\kappa = \frac{\mid \mathbf{Z}_{xx} + \mathbf{Z}_{yy} \mid}{\mathbf{Z}_{xy} - \mathbf{Z}_{yx}} \tag{2.44}$$

This rotationally invariant parameter, should be equal to zero for ideal one- or two-dimensional cases because off-diagonal components vanish (Swift, 1967). In practice, the data is considered as three-dimensional when κ has a value greater than 0.3 (Ledo et al., 1998; Hoffmann-Rothe et al., 2004)

2.3.2. Impedance Tensor Rotation

In most magnetotelluric cases, observed data comprise non-zero values at diagonal elements of impedance tensor. Presence of data errors, galvanic effects and three dimensional structures can restrain two-dimensional approach for several cases. However, to determine the strike direction and reducing the observed data to a possible two-dimensional model, impedance tensor can be rotated with a mathematical approach in ideal situations.

Rotating coordinate frames from (x,y) to $(x_r\ ,y_r)$ until diagonal elements of impedance tensor will become zero, makes off-diagonal elements maximum. The relation between rotated and observed fields can be written as

$$\mathbf{E}^R = \mathbf{R} \cdot \mathbf{E} \;\text{ and }\; \mathbf{B}^R = \mathbf{R} \cdot \mathbf{B} \tag{2.45}$$

where rotation matrix is

$$\mathbf{R} = \begin{bmatrix} \cos\theta & \sin\theta \\ \text{-}\sin\theta & \cos\theta \end{bmatrix} \tag{2.46}$$

After the rotation, the new impedance tensor can be written as

$$\mathbf{Z}^R = \mathbf{R} \cdot \mathbf{Z} \cdot \mathbf{R}^T \tag{2.47}$$

Then the rotated impedance elements are

$$\mathbf{Z}'_{xx} = \frac{\mathbf{Z}_{xx} + \mathbf{Z}_{yy}}{2} - \mathbf{Z}_0(\theta - \frac{\pi}{4})$$

$$\mathbf{Z}'_{yy} = \frac{\mathbf{Z}_{yy} + \mathbf{Z}_{xx}}{2} + \mathbf{Z}_0(\theta + \frac{\pi}{4}) \tag{2.48}$$

$$\mathbf{Z}'_{yx} = \frac{\mathbf{Z}_{yx} - \mathbf{Z}_{xy}}{2} - \mathbf{Z}_0(\theta)$$

where

$$\mathbf{Z}_0(\theta) = \frac{\mathbf{Z}_{xx} + \mathbf{Z}_{yy}}{2}\cos2\theta - \frac{\mathbf{Z}_{xx} - \mathbf{Z}_{yy}}{2}\sin2\theta \tag{2.49}$$

θ is the angle between rotated and observed data and the value that makes $|\mathbf{Z}_{xx}|^2 + |\mathbf{Z}_{yy}|^2$ minimum will give the strike angle. This angle was defined as

$$\tan(4\theta) = \frac{(\mathbf{Z}_{xx} - \mathbf{Z}_{yy})(\mathbf{Z}_{xy} + \mathbf{Z}_{yx})^* + (\mathbf{Z}_{xx} + \mathbf{Z}_{yy})^*(\mathbf{Z}_{xy} - \mathbf{Z}_{yx})}{|\mathbf{Z}_{xx} - \mathbf{Z}_{yy}|^2 - |\mathbf{Z}_{xy} + \mathbf{Z}_{yx}|^2} \tag{2.50}$$

by Swift (1967) and Vozoff (1976). However, this angle can contain an ambiguity with 90^o and its times. Therefore, before appointing TE and TM modes for definite impedance tensor elements, establishing the existing geoelectric strike becomes an important step. Another difficulty on Swift tensor rotation is variation of strike directions depending on chancing frequency. Due to complications of Swift tensor rotation, different approaches were developed in mathematical ways.

2.3.3. Groom-Bailey Decomposition

Local small-scale three-dimensional bodies can distort electric currents and this channelling affects the regional strike direction. Groom and Bailey (GB) decomposition (Groom and Bailey, 1989) is conventionally used to remove galvanic distortion from regional information. Following the distortion removal, geo-electric strike angle can be calculated correctly.

In GB decomposition, impedance tensor is factorized by using the terms of rotation matrix and distortion tensor. The distortion tensor is a 2x2 matrix which is a product of a scalar (site gain g) and three tensor sub-operators (twist $\mathbf{T}$, shear $\mathbf{S}$ and local anisotropy $\mathbf{A}$)

$$\mathbf{C} = g \cdot \mathbf{T} \cdot \mathbf{S} \cdot \mathbf{A} \tag{2.51}$$

Effects of these sub-operators are depicted in Figure 2.2. General expression of GB decomposition can be written as

$$\mathbf{Z}_{obs} = \mathbf{R} \cdot \mathbf{C} \cdot \mathbf{Z}_{2\text{-}D} \cdot \mathbf{R}^T \tag{2.52}$$

where $\mathbf{Z}_{2\text{-}D}$ represents the regional two-dimensional impedance tensor.

In GB decomposition, galvanic distortion is characterized with twist and shear matrices while anisotropy matrix and site gain are related with static shift. Considering the assimilation of anisotropy and site gain into impedance tensor, possibly changes the amplitudes of impedances but it has no effect on strike direction. Therefore, determining the twist and shear matrices will be sufficient to find a unique-solution for decomposition theoretically.

Examining the distortion parameters can be yielded to recover the regional two-dimensional Earth model without effects of local small-scale three-dimensional bodies. Potential misfits such as including noise, can be reduced by using numerical and statistical techniques. McNeice and Jones (2001) developed the GB decomposition for determining the best-fitting strike direction by using the twist and shear values of multiple sites and frequencies.

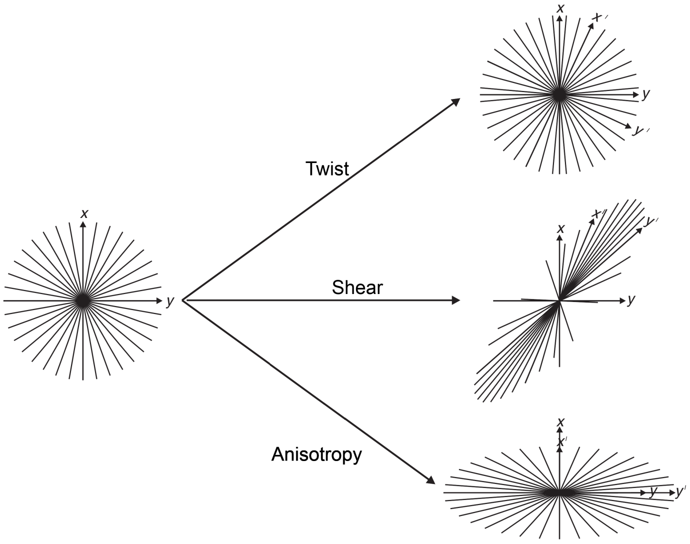

Figure 2.2. Graphical representations of twist, shear and anisotropy effects (Taken from Simpson and Bahr, 2005).

2.3.4. Phase Tensor

The phase information of the observed MT data conserves the actual response of region without effects of galvanic distortion. The phase relations of impedance tensor can be represented with a second-rank tensor and calculation of this tensor requires no assumptions about dimensionality (Caldwell et al., 2004).

The local horizontal electric field can be given as

$$\mathbf{E} = \mathbf{D}' \cdot \mathbf{E}_R = \mathbf{D}' \cdot (\mathbf{Z}_R \cdot \mathbf{B}_R) = (\mathbf{D}' \cdot \mathbf{Z}_R) \cdot \mathbf{B}_R \tag{2.53}$$

where $\mathbf{D}'$ is the 2x2 distortion matrix and regional field is presented with R-subscripted terms. The relation of the observed data with the regional impedance tensor is

$$\mathbf{Z} = \mathbf{D}' \cdot \mathbf{Z}_R \tag{2.54}$$

After impedance tensor is separated into its real and imaginary parts, it can be written as

$$\mathbf{Z} = \mathbf{X} + i\mathbf{Y} \ \text{ and } \ \mathbf{Z}_R = \mathbf{X}_R + i\mathbf{Y}_R \tag{2.55}$$

From equation (2.53)

$$\mathbf{X} = \mathbf{D}' \cdot \mathbf{X}_R \ \text{ and } \ \mathbf{Y} = \mathbf{D}' \cdot \mathbf{Y}_R \tag{2.56}$$

By applying the idea that the ratio of real and imaginary parts of a complex number representing its phase, the phase tensor can be defined as

$$\Phi = \mathbf{X}^{-1}\mathbf{Y} \tag{2.57}$$

By using equations (2.55) and (2.56), relationship between phase tensors can be obtained for the observed and regional impedance tensors (Figure 2.3).

$$\Phi = (\mathbf{D}'\mathbf{X}_R)^{-1}(\mathbf{D}'\mathbf{Y}_R) = \mathbf{X}_R^{-1}\mathbf{D}'^{-1}\mathbf{D}'\mathbf{Y}_R = \mathbf{X}_R^{-1}\mathbf{Y}_R = \Phi_R \tag{2.58}$$

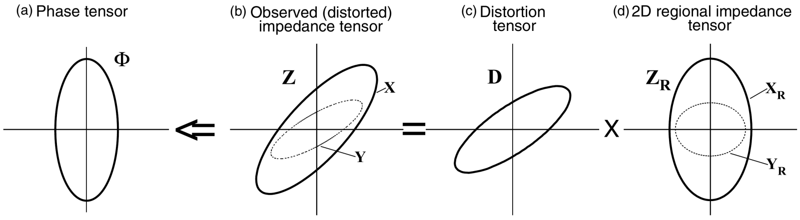

Figure 2.3. Graphical representation of the tensors involved in the galvanic distortion of a 2-D impedance tensor. The coordinate axes are aligned parallel and perpendicular to the strike of the two-dimensional conductivity structure. (a) shows the ellipse representing the phase tensor, which is derived from the real (solid line) and imaginary (dotted line) parts of the distorted impedance tensor in (b). The ellipse in (b) is characterized by the distortion tensor represented by the ellipse in (c) and 2-D regional impedance tensor which is given in (d) (Taken from Caldwell et al., 2004).

Then, the phase tensor calculated from observed data corresponds to real response of the region. Real and imaginary components of impedance tensor can be used to write the phase tensor as a matrix

$$\begin{bmatrix} \Phi_{11} & \Phi_{12} \\ \Phi_{21} & \Phi_{22} \end{bmatrix} = \frac{1}{\det(\mathbf{X})} \begin{bmatrix} X_{22}Y_{11} - X_{12}Y_{21} & X_{22}Y_{12} - X_{12}Y_{22} \\ X_{11}Y_{21} - X_{21}Y_{11} & X_{11}Y_{22} - X_{21}Y_{12} \end{bmatrix} \tag{2.59}$$

where $\det(\mathbf{X}) = X_{11}Y_{22} - X_{21}Y_{12}$ represents determinant of $\mathbf{X}$. To present phase tensor in terms of ellipse parameters, four elements of phase tensor are determined. These are the minimum (Φ_{min}) and maximum (Φ_{max}) tensor values, the skew angle (β) and the non-invariant angle (α) (Figure 2.4). Caldwell et al. (2004) algebraically described three tensor invariants which are named as trace, skew and determinant of the matrix, to represent these elements.

$$\begin{aligned} \mathrm{tr}(\Phi) &= \Phi_{11} + \Phi_{22} \\ \mathrm{sk}(\Phi) &= \Phi_{12} - \Phi_{21} \\ \det(\Phi) &= \Phi_{11} + \Phi_{22} \end{aligned} \tag{2.60}$$

After writing all invariants as the first order functions

$$\begin{aligned}\Phi_1 &= \mathrm{tr}(\Phi)/2\\ \Phi_2 &= [\det(\Phi)]^{1/2}\\ \Phi_3 &= \mathrm{sk}(\Phi)/2\end{aligned} \tag{2.61}$$

obtained quantities can be used to calculated Φ_{min}, Φ_{max} and β.

$$\Phi_{min} = (\Phi_1^2 + \Phi_3^2)^{1/2} - (\Phi_1^2 + \Phi_3^2 - \Phi_2^2)^{1/2} \tag{2.62}$$

$$\Phi_{max} = (\Phi_1^2 + \Phi_3^2)^{1/2} + (\Phi_1^2 + \Phi_3^2 - \Phi_2^2)^{1/2} \tag{2.63}$$

$$\beta = \frac{1}{2}\tan^{-1}(\frac{\Phi_3}{\Phi_1}) \tag{2.64}$$

The last parameter α can be defined as

$$\alpha = \frac{1}{2}\tan^{-1}(\frac{\Phi_{12} + \Phi_{21}}{\Phi_{11} - \Phi_{22}}) \tag{2.65}$$

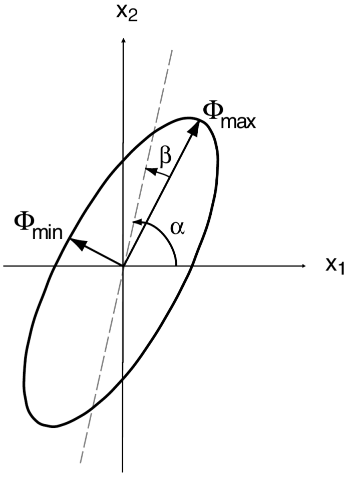

Figure 2.4. Graphical representation of the phase tensor including four elements. (Taken from Caldwell et al., 2004).

For one-dimensional Earth model, the regional phase is determined by a single element and represented with a circle of unit radius for all periods graphically. In two-dimensional Earth model, phase tensor is symmetric and β is zero. The strike direction is determined by α where Φ_{min} and Φ_{max} corresponds TE- and TM-mode phases. Large values of β is an indicator of three-dimensional resistivity structure. The phase tensor is illustrated as ellipse in three-dimensional Earth model and the angle of the major axis which determines the strike direction, is given as α-β.

2.3.5. Induction Arrows

The relationship between vertical and horizontal magnetic fields can be used to figure out lateral changes in conductivity. Vertical transfer functions (or tipper) are calculated by using complex ratios of the field components (Parkinson, 1959; Wiese, 1962).

$$\mathbf{B}_z = \begin{bmatrix} \mathbf{T}_x & \mathbf{T}_y \end{bmatrix} \begin{bmatrix} \mathbf{B}_x \\ \mathbf{B}_y \end{bmatrix} \tag{2.66}$$

In vector form, these function is presented as induction arrows which point out the closest anomalous conductor for relevant frequencies in Parkinson convention (Parkinson, 1959).

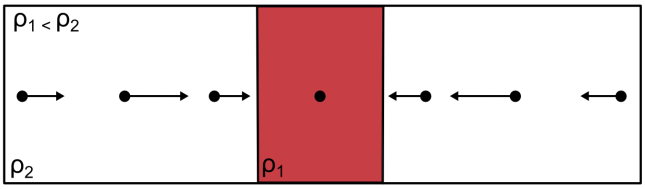

Figure 2.5. Behaviour of real parts of induction arrows in two-dimensional Earth model.

Because lateral conductivity variations give rise to vertical magnetic fields, induction arrows are only related with TE mode in two-dimensional Earth model due to equations (2.38) and (2.39). Presence of a conductor-resistor boundary characterizes the induction arrows in both magnitude and direction. While the orientations of the arrows are perpendicular to the boundary, magnitudes are equivalent to strength of the anomalous conductor (Jones and Price, 1970). Across the boundary, induction arrows tend to become larger until they reach the center of conductor. Induction arrows evanish in the center of conductor and eventually reverse their character after moving away on the other side (Figure 2.5).

2.4. Modeling

Modeling of data is one of the most important steps in a magnetotelluric survey. By utilizing the impedance or information derived from it and tipper data, an electrical resistivity model can be obtained in actual spatial dimensions. This process includes two interrelating operations which are forward and inverse modeling. While forward modeling of MT data aims to calculate the resistivity and phase values for a given Earth model, the inverse modeling iteratively compares the observed and calculated data by minimizing the misfit between them. Dependence of inversion algorithms and the parameters used causes non-uniqueness for inverse modeling and different models can be produced from an identical MT dataset.

Following the design of an initial resistivity model, predicted data (**D**) is calculated from this model. While **m** represents model parameters and F is forward modeling function, their relation with predicted data presents the general form of forward modeling

$$\mathbf{D}_p = \mathrm{F}(\mathbf{m}) \tag{2.67}$$

Observed data (**d**) and model parameters (**m**) are presented as vectors with a length of M and N, respectively

$$\mathbf{m} = [m_1, m_2, m_3, ..., m_M]^T \quad \text{and} \quad \mathbf{d} = [d_1, d_2, d_3, ..., d_N]^T \tag{2.68}$$

where T indicates the transpose of matrices. Then the inverse problem can be written in a form of

$$\mathrm{F}(\mathbf{d}, \mathbf{m}) = \mathbf{d} - \mathrm{F}(\mathbf{m}) + \mathrm{e} \tag{2.69}$$

where e represents the error in the equation.

Code of Rodi and Mackie (2001) (herein RM2001) is a nonlinear conjugate gradients (NLCG) algorithm for two-dimensional inversion of MT data and have options to operate apparent resistivity and phase information for both TE- and TM-modes, in addition to tipper data (Rodi and Mackie, 2001). Due to inversion algorithms mostly handle more model parameters than relevant data, an underdetermined problem occurs. To solve the inverse problem then, new constraints are established into resistivity model as optional conditions. RM2001 deals with the inverse problem by using the approach of Tikhonov and Arsenin (1977) which seeks a regularized solution to be a model with increasing spatial smoothness while minimizing an objective function. General form of regularized inversion through gradient-based minimization of a objective function (Egbert and Kelbert, 2012) can be given in form of

$$\Psi(\mathbf{m}, \mathbf{d}) = (\mathbf{d} - \mathrm{F}(\mathbf{m}))^T \mathbf{C}_d^{-1} (\mathbf{d} - \mathrm{F}(\mathbf{m})) + \lambda (\mathbf{m} - \mathbf{m}_0)^T \mathbf{C}_m^{-1} (\mathbf{m} - \mathbf{m}_0) \qquad (2.70)$$

where λ representing smoothing (trade-off) parameter while $\mathbf{C}_d$ and $\mathbf{C}_m$ are the covariance matrices of data and model parameters, respectively. Depending on NLCG, two different parameters controls the smoothing of the algorithm: the regularization parameter (τ) and horizontal smoothing parameter (α'). While τ manage the general smoothing of the model, α' decides the horizontal evolution. Higher values force the model to be smoother but the fit of data decrease correspondingly.

WSINV3DMT is a three-dimensional inversion algorithm which executes Occam approach on data-space to reduce computational time and required memory. Minimizing the penalty function in data-space, eliminates the parameters which are ineffectual on the data thus decrease the number of required equations (Siripunvarporn et al., 2005). With the certain reduction in the computational costs, usage of Occam approach become possible for three-dimensional modeling implementations. Since the inversion of MT data requires non-uniqueness, Occam approach searches for the simplest or smoothest model to illustrate the results in a correct way (Constable et al., 1987). WSINV3DMT can utilize full impedance tensor (both real and imaginary parts) and tipper information and works on two different phases. In the first phase the algorithm seeks for target RMS values, subsequently it proceeds to second phase by achieving desired misfit. In this stage the code maintains the misfit at same level and starts to search for a minimum-norm model. With this purpose it uses different Lagrange multipliers by changing λ values in each iteration (Siripunvaraporn et al., 2005)

ModEM is a three-dimensional inversion algorithm which using NLCG scheme for parameter search. This modular system is based on finite-difference approach and discretizes the forward problem for numerical solution (Egbert and Kelbert, 2012). The aim of ModEM is minimizing penalty functional during model updating (Kelbert el al., 2014). Beyond the Jacobian of the mapping from model parameters to data is a key element in electromagnetic inversion methods, ModEM factorizes the Jacobian into different components to reduce computational disadvantages. (Egbert and Kelbert, 2012). ModEM can utilize full impedance tensor (both real and imaginary parts) and tipper information. In the algorithm, smoothing is governed by λ parameter and deciding the value of λ is a crucial step. During the inversion, potential changes of the parameter may cause misdirection for searching path while usage of certain values prevent the algorithm to overcome the local minima (Meqbel et al., 2016).

3. STUDY FIELD

3.1. Introduction

Turkey is one of the most affected countries by earthquake activity in the world. Due to the convergence between Eurasian and Arabian plates, Anatolia have become one of the most dynamic regions tectonically. Two principal faults hosted in the region, North Anatolian (NAF) and East Anatolian (EAF) Faults, have caused the majority of devastating earthquakes in the last century. As one of the largest active faults in the world, NAF is a 1200 km long strike-slip fault which attaches the East Anatolian convergent area with the Hellenic subduction zone. This dextral intracontinental transform fault began forming 13–11 Ma ago near Karlıova in the east and reached Marmara Sea in last 200 ka (Şengör et al., 2005).

NAF breaks into three active branches while entering the Marmara Sea near İzmit and demonstrate a more complex structure at the northwest Anatolia. The northernmost strand follows Marmara Sea before exiting near Gaziköy, Tekirdağ and it vanishes again in the Saros Bay. This 45 km long segment is named as Ganos Fault (GF) and produced the M_w 7.4 Şarköy-Mürefte earthquake in 1912 (Ambraseys and Finkel, 1987; Ambraseys, 2002). With periodical centennial cycles, seismic activities along NAF tend to propagate from east to west (Parsons et al., 2000; Şengör et al., 2005). In the history, salient earthquakes (e.g. October 18, 1343 and August, 5 1766 events) has been generated by GF however there is a certain lack of seismicity (Tüysüz, 1998; Janssen et al., 2009; Öztürk et al., 2015), since the 1912 Şarköy-Mürefte earthquake. Therefore, GF can be considered as a seismic gap that is unable to produce large events between earthquake cycles. Following the destructive 1999 İzmit and Düzce earthquakes, the next important event is potentially expected on the western part of NAF, especially on segments within the Marmara Sea and/or GF. (Şengör et al., 2005).

Paleoseismological studies at GF state that seismic activities ($M>7$) have repeated in 323±142 years with an average coseismic slip rate of 5.25 m (Meghraoui et al., 2012). The interseismic deformation pattern along GF is established through visco-elastic and elastic half-space models which created with inversion schemes based on geodetic data (Motagh et al., 2007). The estimated locking depth is found as ~8-17 km with both models, which is in good agreement with the earthquake data.

3.2. Tectonic Setting

The driving forces behind the neotectonic evolution of Turkey are roll-back of Hellenic subduction zone and collision of Anatolian and Arabian plates. Slab roll-back of Hellenic subduction zone pulls the Anatolian Plate towards west and causes extension in the Aegean region. Besides, collision of Anatolian and Arabian Plates along Bitlis-Zagros suture zone contributes the westward escape of Anatolian Plate (Figure 3.1). Therefore, Anatolian Plate moves along dextral NAF and sinistral EAF into the north-south-extending of Aegean region (Okay et al, 1999; Cavazza et al., 2009).

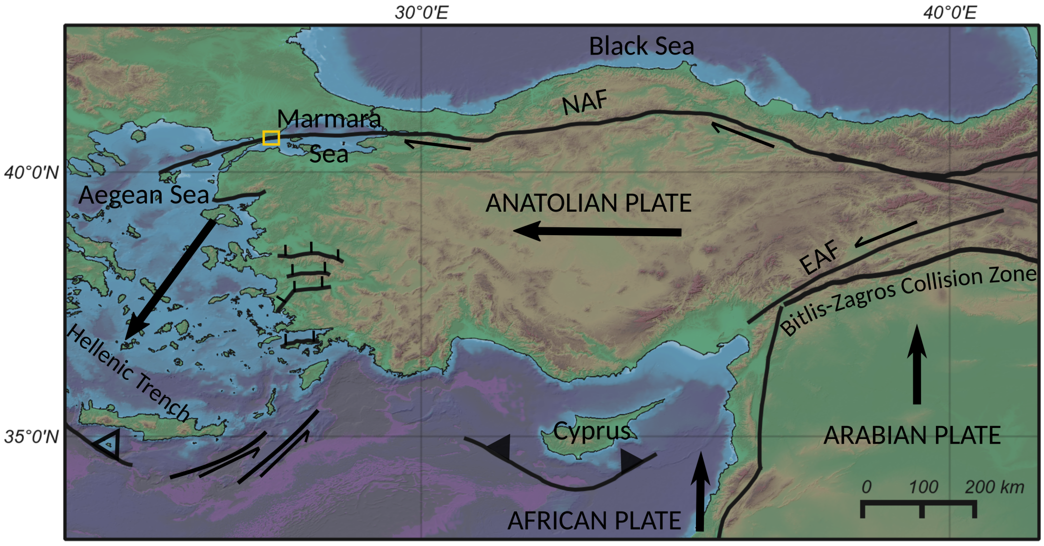

Figure 3.1. Tectonic setting of Turkey edited from Okay et al., 1999. Yellow square shows the study field. Arrows indicate the direction of plate motions.

In the Northwest Anatolia, NAF constitute distinctive structures from rest of its scope such as deep marine strike-slip basins on the sea and NW-trending major dextral strike slip faults on the land. This structures are created by the transpressional and transtensional activities of the fault (Okay et al., 1999). GF proceeds parallel to Ganos Mountain which is a significant uplift structure related to transpressional strain (Okay et al., 2004).

Besides the neotectonic activities of NAF, evolutionary processes of prominent features in the area trace to prior of its arrival to the region (Zattin et al., 2005). When stress regime of NAF reached out west enough to capture this mechanically weak area, which is now known as GF, the fault system was activated as a strike-slip fault in the late Pliocene. By establishing an obliquity for the fault, this crustal weakness may provoke complex kinematic variations (Seeber et al., 2004). From Oligocene to mid-Miocene, a plausible environment for shortening that conducts uplift of the Ganos Mountain have been generated as a result of the interchanging stress regime between the tectonic stages of GF system.

Even though, there is no clear evidence to understand driving force of the preceding events, it is possibly linked to the far-field stress regime caused by Intra-Pontide subduction and the rotation of Anatolian Plate accommodated with Aegean subduction rollback (Zattin et al., 2005). Displacement vectors which are modeled with geodetic measurements reveal that the obliquity is only $3^o \pm 1$ on GF and $14^o \pm 3$ on Western Central Marmara Fault. Under these circumstances the weak transpressive behavior changes into strong transtensive one while moving eastwards along NAF. The transition between the two different deformation types is constituted by the Ganos bend which rotates $\sim 17^o$ to south in the fault plane moving westwards (Okay et al., 2004).

3.3. Geology

The geological structure of north and south of GF show different attributes, which are analogous to the tectonic setting described above. Since the geological formations at two sides of the fault overlie different basement types, their ages and contents determine the electrical resistivity characters (Figure 3.2).

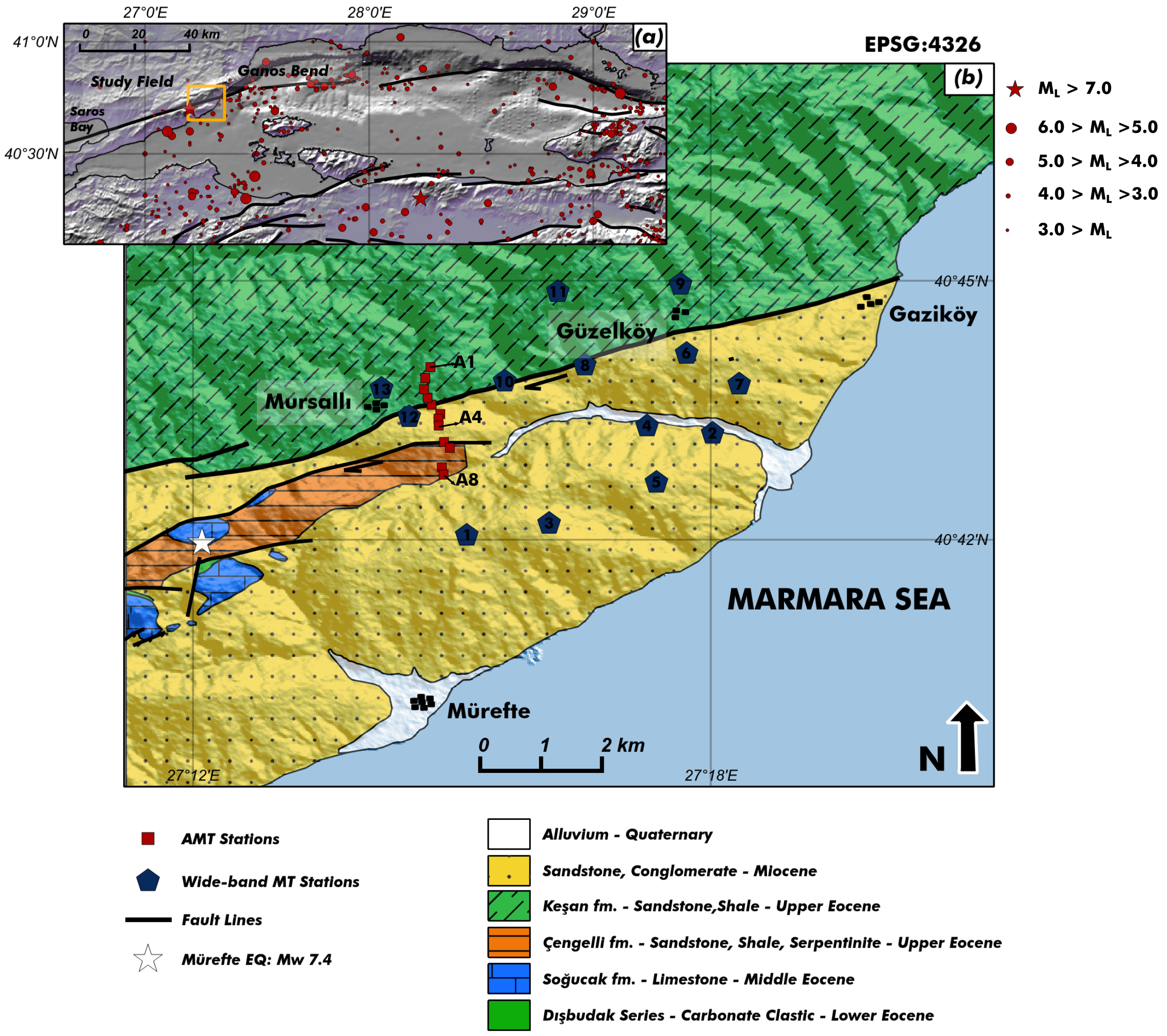

Figure 3.2. (a) Topographic map of Marmara Region, overlain by active fault branches and earthquake data (taken from Kandilli Observatory and Earthquake Research Institute's Earthquake catalog). Yellow rectangle shows the position of the study field. Ganos bend and Saros Bay are also indicated as the two ends of terrestrial GF. (b) Geology map of the study area edited from Okay et al, 2010.

Keşan Formation is the prominent stratum on the north made up of Upper Eocene - Oligocene aged shale, sandstone and siltstone intercalation. This formation represents the Ganos Mountain which is an anomalous uplift located at the eastern end of GF.

With a maximum relief of 2000 m, Ganos Mountain ends with a steep slope (up to 50°) on the south. Gaziköy Formation is the oldest one in the study area and this Eocene aged shale and siltstone sequence is overlaid by Keşan Formation (Okay et al., 2004).

On the other hand, there is a more complicated structure appears on the south of GF. Here, Dışbudak series beneath Çengelli and Soğucak formations represent a sequence from Lower Eocene to Lower Oligocene and ophiolitic rocks constitute a basement. The Eocene units in the study area mainly consist of sandstone, shale and olistoliths, in addition to small contents of serpentinite, limestone and gabbro. Another important geological feature is highly porous large mid-Miocene sandstone blocks unconformably overlying the Eocene- Oligocene aged units (Figure 3.2, Okay et al., 2010; Özcan et al., 2010).

4. DATA PROCESSING

4.1. Magnetotelluric Data Acquisition

The magnetotelluric data in this study, were collected with two separated field campaigns. First campaign was planned to establish an AMT profile that aims to focus on electrical resistivity structure of first 1000 meters and reveal the potential fault zone conductor. The continuous 2.5 km-long AMT profile across Ganos Fault was completed with north-south aligned twelve observation points in the east of Mursallı town. AMT data process was followed by the wide-band MT study to understand deeper electrical resistivity structure. The wide-band MT survey consists of thirteen stations which were arranged to form a grid inclosing the AMT profile (Figure 3.2).

Two Phoenix Geophysics systems (MTU – 5A) with the compatible magnetic coils (AMTC – 30) were utilized to record five channel AMT data. The frequency of this systems range between 10400 Hz. – 1 Hz. Electric field measurements were done with non-polarizing Pb-PbCl_2 electrodes. Dipole lengths were generally 50-60 meters for each electrode array and electrodes were buried below the surface for better contact. Signs of noise which was caused by a radio antenna near the study field, were detected between range of 2000 s. – 1000 s. in the test observations. In order to reduce the local magnetic noise with remote reference technique (Gamble et al., 1979), both systems were simultaneously worked.

In the second campaign, wide-band MT observations were performed with 320 Hz. – 2000 s. frequency-ranged MTU – 5 systems with compatible MTC – 50 coils of Phoenix Geophysics. Non-polarizing Pb-PbCl_2 electrodes were used to measure electric fields in the five-channel wide-band MT stations which were located between Mursallı and Güzelköy towns. All electrodes and magnetic coils were buried and logger instruments were placed into boxes for avoiding noise and ensuring safety. Two wide-band MT stations were deployed per each day in this seven-day campaign and stations were moved to next locations after the data was successfully recorded.

4.1.1. Remote Reference Method

Eliminating noise from observed MT data is an important step to improve data quality and help to achieve more accurate models after inversion. Although, least square and robust processing techniques can be utilized to remove biasing effects of noise, they generally have auto-powers in equations. Because components are coherent with themselves, the noise contained in the components are heightened.

Where the observed electric and magnetic fields that contain noise is represented as

$$\mathbf{E}_{xobs} = \mathbf{E}_x + \mathbf{E}_{xnoise} \text{ and } \mathbf{B}_{xobs} = \mathbf{B}_x + \mathbf{B}_{xnoise} \tag{4.1}$$

auto spectra of a field is

$$\begin{aligned}
\langle \mathbf{E}_{xobs}\mathbf{E}_{xobs}{}^* \rangle &= \langle \mathbf{E}_x + \mathbf{E}_{xnoise} \rangle \langle \mathbf{E}_x{}^* + \mathbf{E}_{xnoise}{}^* \rangle \\
\langle \mathbf{E}_{xobs}\mathbf{E}_{xobs}{}^* \rangle &= \langle \mathbf{E}_x\mathbf{E}_x{}^* \rangle + 2\underbrace{\langle \mathbf{E}_x\mathbf{E}_{xnoise} \rangle}_{=0} + \langle \mathbf{E}_{xnoise}\mathbf{E}_{xnoise}{}^* \rangle \\
\langle \mathbf{E}_{xobs}\mathbf{E}_{xobs}{}^* \rangle &= \langle \mathbf{E}_x\mathbf{E}_x{}^* \rangle + \langle \mathbf{E}_{xnoise}\mathbf{E}_{xnoise}{}^* \rangle
\end{aligned} \tag{4.2}$$

where * denotes its complex conjugate. Because they are incoherent with each other, only $\langle \mathbf{E}_x\mathbf{E}_{xnoise} \rangle$ term equals to zero in this equation and the noise containing element is still present.

Besides the auto-spectra, all noise containing elements in the equation of cross spectra are evanished and only the unbiased data is preserved.

$$\begin{aligned}
\langle \mathbf{E}_{xobs}\mathbf{B}_{y_{obs}}{}^{*}\rangle &= \langle \mathbf{E}_{x} + \mathbf{E}_{xnoise}\rangle\langle \mathbf{B}_{y}{}^{*} + \mathbf{B}_{y_{noise}}{}^{*}\rangle \\
\langle \mathbf{E}_{xobs}\mathbf{B}_{y_{obs}}{}^{*}\rangle &= \langle \mathbf{E}_{x}\mathbf{B}_{y}{}^{*}\rangle \underbrace{\langle \mathbf{E}_{x}\mathbf{B}_{y_{noise}}{}^{*}\rangle}_{=0} \underbrace{\langle \mathbf{E}_{xnoise}\mathbf{B}_{y}{}^{*}\rangle}_{=0} \underbrace{\langle \mathbf{E}_{xnoise}\mathbf{B}_{y_{noise}}{}^{*}\rangle}_{=0}
\end{aligned} \tag{4.3}$$

To use the advantage of this mathematical property, remote reference method (Gamble et al., 1979) can be utilized on field surveys. By installing additional sensors to a location far from observation point, new electromagnetic components that are unaffected by noise at the target area can be simultaneously measured. Therefore, the noise which is uncorrelated between both sites, can be eliminated by using required components of remote reference site.

Because showing more homogeneity at the vicinity of lateral heterogeneities, being more unsusceptible against polarization and low-level of contained noise; remote references method favors magnetic fields rather than electric fields. Elements of impedance tensor which is given in Equation (2.39) can be calculated by using cross-spectra terms including measured data from the remote site:

$$\begin{aligned}
\mathbf{Z}_{xx} &= \frac{\langle \mathbf{E}_{x}\mathbf{B}_{xr}{}^{*}\rangle\langle \mathbf{B}_{y}\mathbf{B}_{y_{r}}{}^{*}\rangle - \langle \mathbf{E}_{x}\mathbf{B}_{y_{r}}{}^{*}\rangle\langle \mathbf{B}_{y}\mathbf{B}_{xr}{}^{*}\rangle}{DET} \\
\mathbf{Z}_{xy} &= \frac{\langle \mathbf{E}_{x}\mathbf{B}_{y_{r}}{}^{*}\rangle\langle \mathbf{B}_{x}\mathbf{B}_{xr}{}^{*}\rangle - \langle \mathbf{E}_{x}\mathbf{B}_{xr}{}^{*}\rangle\langle \mathbf{B}_{x}\mathbf{B}_{y_{r}}{}^{*}\rangle}{DET} \\
\mathbf{Z}_{yx} &= \frac{\langle \mathbf{E}_{y}\mathbf{B}_{xr}{}^{*}\rangle\langle \mathbf{B}_{y}\mathbf{B}_{y_{r}}{}^{*}\rangle - \langle \mathbf{E}_{y}\mathbf{B}_{y_{r}}{}^{*}\rangle\langle \mathbf{B}_{y}\mathbf{B}_{xr}{}^{*}\rangle}{DET} \\
\mathbf{Z}_{yy} &= \frac{\langle \mathbf{E}_{y}\mathbf{B}_{y_{r}}{}^{*}\rangle\langle \mathbf{B}_{x}\mathbf{B}_{xr}{}^{*}\rangle - \langle \mathbf{E}_{x}\mathbf{B}_{y_{r}}{}^{*}\rangle\langle \mathbf{B}_{y}\mathbf{B}_{xr}{}^{*}\rangle}{DET}
\end{aligned} \tag{4.4}$$

where the determinant is

$$DET = \langle \mathbf{B}_x \mathbf{B}_{xr}{}^{*} \rangle \langle \mathbf{B}_y \mathbf{B}_{y_r}{}^{*} \rangle - \langle \mathbf{B}_x \mathbf{B}_{y_r}{}^{*} \rangle \langle \mathbf{B}_y \mathbf{B}_{xr}{}^{*} \rangle \tag{4.5}$$

The impedance tensor computed with these equations will be unbiased by the noise in the main observation point. However, a strong correlation between naturally-induced fields of main and remote sites is necessary. While application of remote reference method highly improves data quality, it can be impractical in electrically multi-dimensional environments. Since the cross-spectra terms are affected by noise as much as auto-spectra, more advance techniques might be used for data reduction.

4.2. Time Series Analyses

The magnetotelluric data is recorded as a function of time in the field. (Figure 4.1) shows an example from AMT time series collected at station MUR005 near Ganos Fault. As seen in the example time series represent five components and product a large dataset to work. On the contrary a transfer function such as the complex impedance tensor is more practical due to containing limited frequencies.

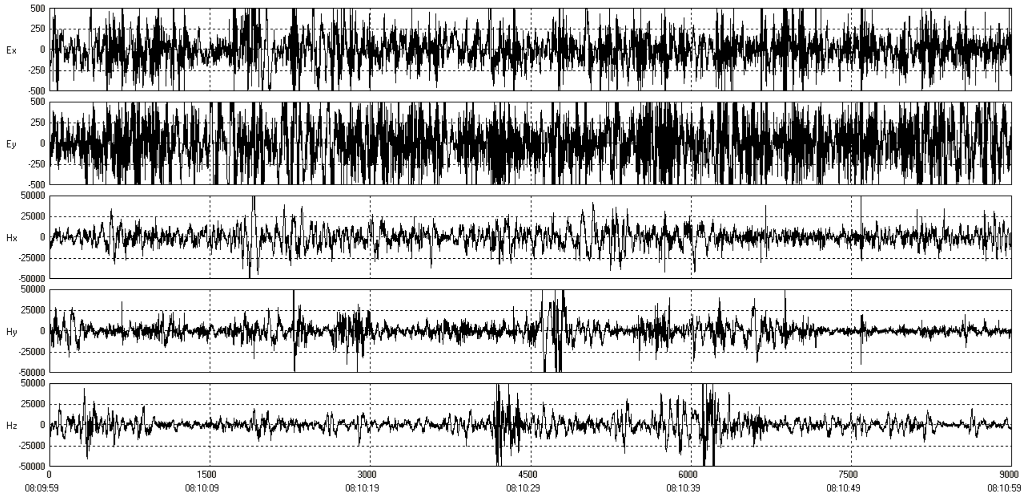

Figure 4.1. One minute sequence of recorded time series for five components of station MUR005.

Fourier transformation is the major way for transferring the data from time series to frequency domain. By following the trend removal and filtering, Fast Fourier Transform is applied to data set. The data reduction is provided by averaging of chosen evaluation frequencies. Auto- and cross-power density spectra are used for averaging procedure but the MT data is still biased by noise. Statistical techniques such as least square or robust estimation of transfer function can improve the data quality. On the other hand, the remote references method led to significant improvements in data quality.

Following the application of remote references method to the data, transfer functions of each station is presented via apparent resistivity and impedance phase graphs. Both of graphics are plotted against frequency on the logarithmic scale. Figure 4.2 shows the apparent resistivity and impedance phase graphs of station MUR003 for both raw and corrected versions.

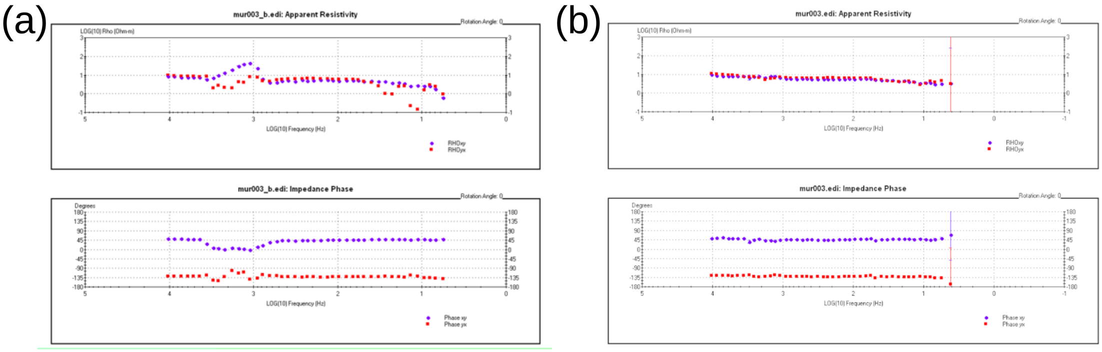

Figure 4.2. Apparent resistivity and phase curves of station MUR003 for (a)raw data and (b) corrected with remote references method.

4.3. Dimensionality Analyses

Once apparent resistivity and phase values are computed from impedance tensor, dimensionality analysis is the next stage in magnetotelluric data processing. In this study, the dimensionality of the data is investigated with the techniques described in the Chapter 2. While AMT dataset is evaluated to make required assumptions for two-dimensional modeling with a conventional attitude, the purpose of analyzing wide-band MT dataset is understanding the nature of data in physical manner.

To provide preliminary information, firstly, skew parameters calculated for both datasets. Although it is not a sufficient criterion to decide the dimensionality of the data, skew values indicate a potential three-dimensional structure at only higher periods. For AMT data, skew values are generally close to zero until the periods longer than 0.5 s (Figure 4.3).

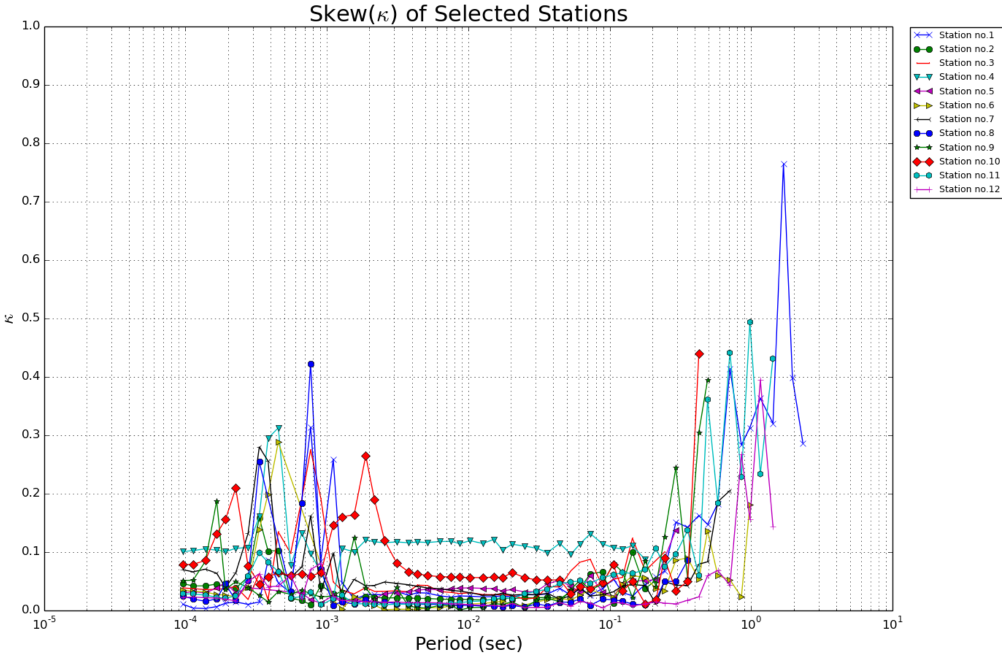

Figure 4.3. Skew values for AMT stations.

Figure 4.4 shows the graph of wide-band MT dataset where the skew values consistently remain lower than 0.3 until they tend to be greater after 5 s. Since most of sites have low skew values except at much longer periods, this situation implies that the overall electrical structure in the study area can be characterized as one- or two-dimensional cases.

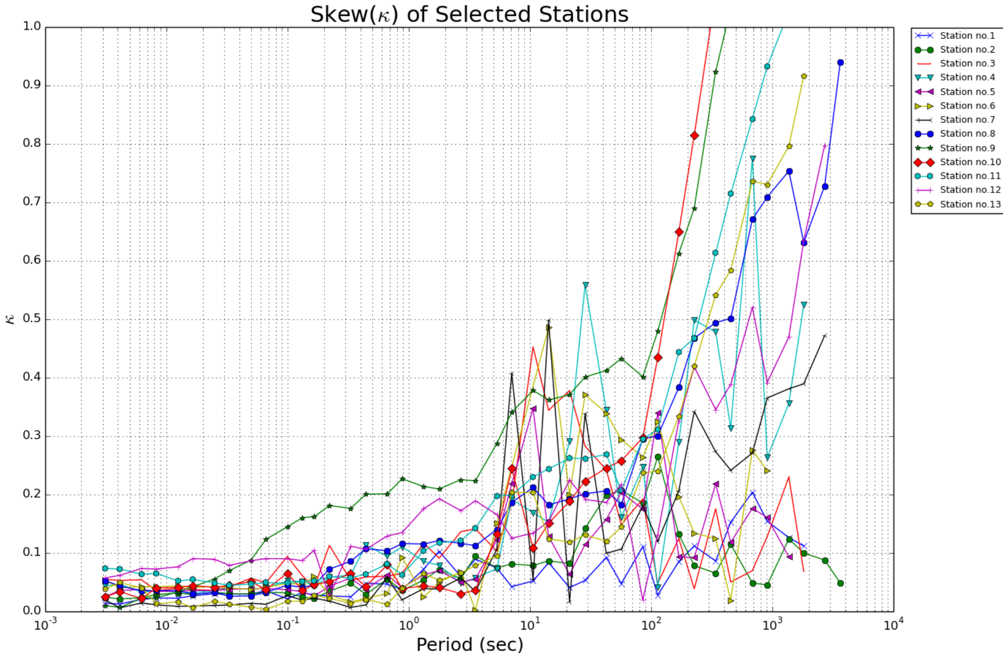

Figure 4.4. Skew values for wide-band MT stations.

In this study, AMT data was gathered on profile which gives a chance to both two- and three-dimensional modeling, although wide-band MT data was collected in a form of grid to be processed with three-dimensional approach. Therefore, determining the strike direction is the crucial step in the dimensionality analyses before applying two-dimensional modeling. For this purpose, Groom and Bailey (GB) decomposition is applied to AMT data by using the “Strike” code of McNeice and Jones (2001). After all combinations of sites and frequencies are checked separately, so-called single-site-multi-frequency approach presents consistent strike directions for all stations. Then multi-site-multi-frequency approach yields an overall geo-electric strike angle as ∼N70°E for the region. Frequencies above 2500 Hz which are irrelevant in determination of the geo-electric strike direction at the seismogenic depths, are ignored in this calculation.

Phase tensor analyses developed by Caldwell et al. (2004) is then applied as another way to investigate the dimensionality of the MT data. Since bringing the advantage of verifying distortion-free dimensionality information, phase tensor analyses results are presented in the form of rose diagrams and phase tensor ellipses in this study. In a good agreement with GB decomposition, phase tensor analyses yield the strike direction as N70°E for AMT dataset (Figure 4.5).

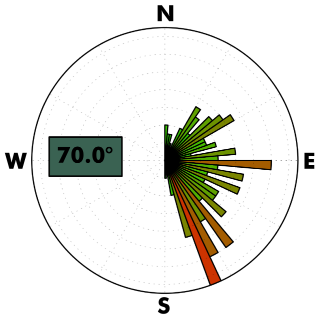

Figure 4.5. Rose diagram presentation of strike angles yielded by phase tensor analyses for AMT dataset.

For MT dataset, rose diagrams of each decade are given separately in Figure 4.6. Lower frequencies corresponding to the seismogenic depths (100 – 0.01 Hz) appears similarly towards the geo-electrical strike while higher frequencies are effected by local features in the region.

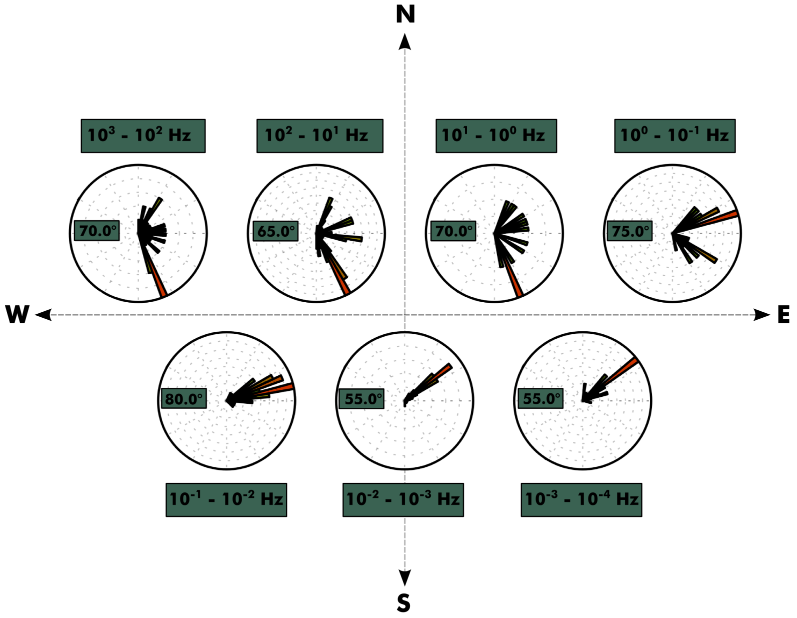

Figure 4.6. Rose diagram presentation of strike angles yielded by phase tensor analyses for wide-band MT data for all decades distinctively.

In Figure 4.7 phase tensors are graphically presented by ellipses in which the major axes show the polarization direction and β values (i.e. skew angles) give the essential information about dimensionality. Higher and lower β values which indicate three-dimensionality, are specified with extreme colors (dark red and dark blue) within these ellipses. To display the change depending to depth, phase tensor ellipses are drawn for frequencies 40 Hz, 4.5 Hz, 0.75 Hz, and 0.141 Hz. Although low β values appears at higher frequencies when the phase tensor ellipses are examined, a highly three-dimensional electrical structure becomes obvious for the deeper parts, especially frequencies lower than 0.2 Hz. The only exception for this situation in the region, can be observed at station 10 which shows consistently high β values at all examined frequencies.

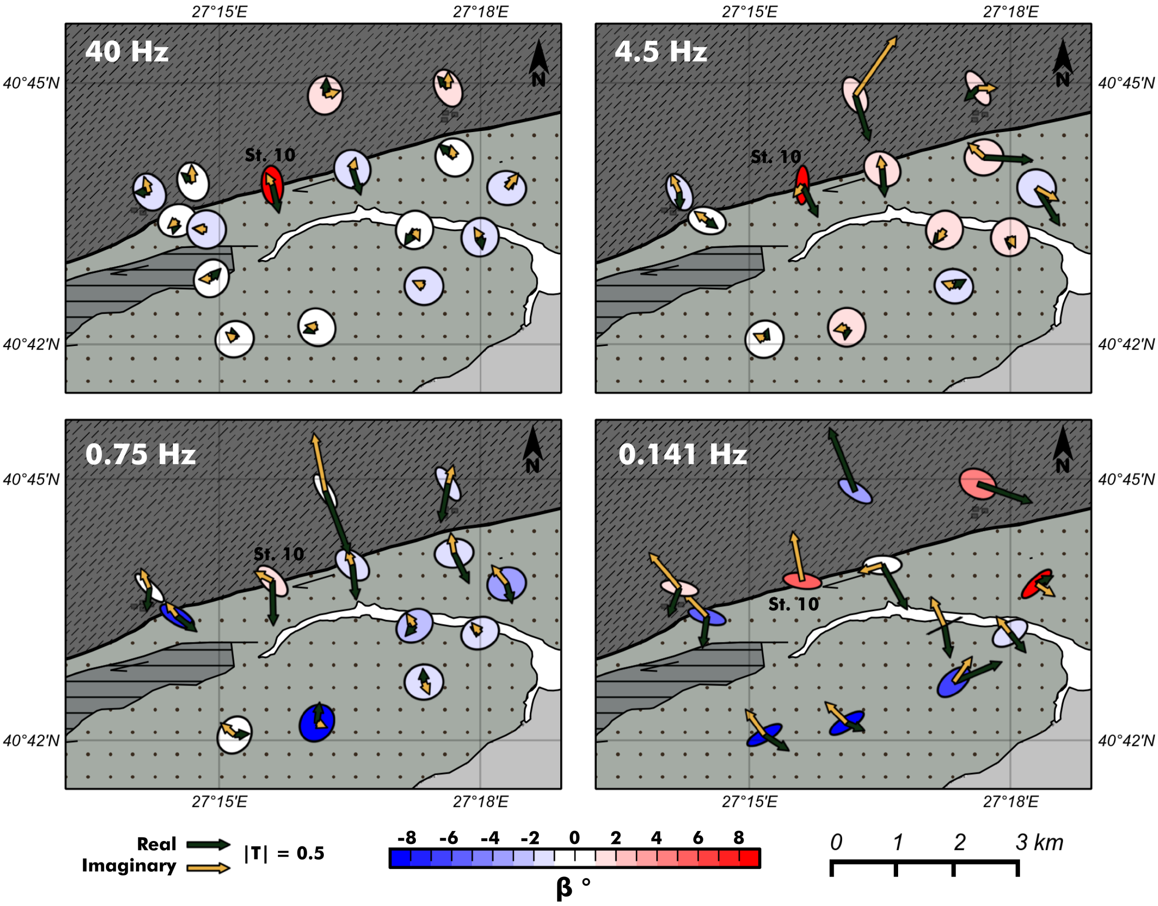

Figure 4.7. Map view of phase tensor with real and imaginary induction arrows at frequencies 40 Hz, 4.5 Hz, 0.75 Hz and 0.141 Hz. Phase tensor ellipses are colored with β angles, where any value other than zero is indicative of a three-dimensional electrical structure and the degree of it increases as the angle takes extreme values at both sides.

In addition to GB decomposition and phase tensor analyses, induction arrows are also utilized to investigate dimensionality of data. Parkinson convention where the real components of the arrows point to the conductor, is used in this study. For AMT data, the real components of induction arrows for chosen frequencies 57 Hz, 27.5 Hz and 9.4 Hz at each station across the fault, are shown in Figure 4.8. While induction arrows in the north of the fault point towards south-southwest, arrows in the south have north-northeast directions. As mentioned in Chapter 2, decreasing magnitudes while moving from both sides indicates presence of a conductor in the middle as portrayed in the classical characterization of induction arrows for two-dimensional Earth.

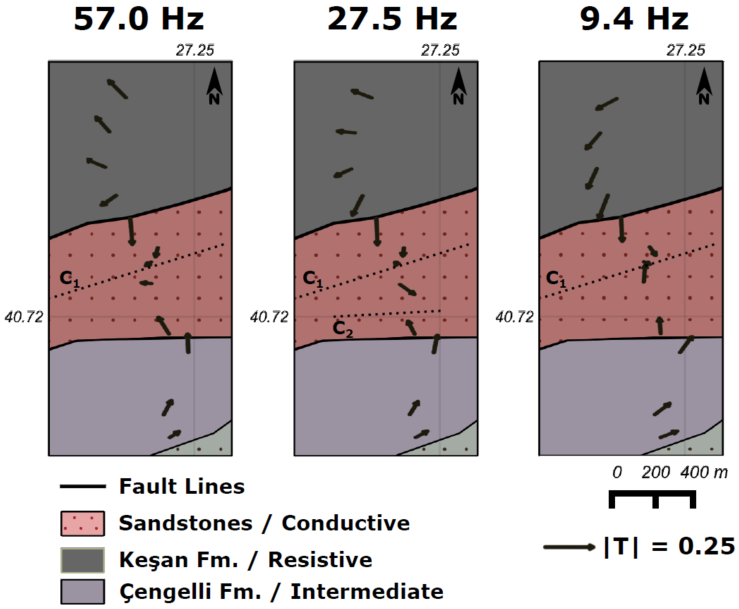

Figure 4.8. The real induction arrows of AMT data for frequencies 9.4 Hz, 27.5 Hz, 57 Hz plotted on geology map colored with relative resistivity values. C_1 and C_2 are the interpreted centers of the conductive structures.

For all wide-band MT stations and additional three AMT stations, the real and imaginary induction arrows alongside with corresponding phase tensor ellipses mention above are shown as a map view in Figure 4.7. Extreme tenacity of induction arrows to Marmara Sea at frequencies lower than 0.1 Hz, settle a threshold where the tipper data is greatly biased by coast effect. Above the frequency of 0.1 Hz, real parts of induction arrows point to conductive areas where are potentially driven by the fault related structures while imaginary parts lie anti-parallel to them, thus justify the idea of two-dimensional electrical character.

4.4. Modeling of Data

As mentioned in previous chapter, modeling of data is the ultimate step in an MT survey. Following the data reduction and dimensionality analyses, producing a final model by using forward and inverse algorithms convert the data into true spatial dimensions. In this thesis, two- and three-dimensional modeling routines are used to invert the observed data. Profile-based AMT dataset was evaluated with both two- and three-dimensional algorithms, while only three-dimensional modeling was applied to grid-based wide-band MT dataset. Since two-dimensional modeling requires the elimination of impedance tensor's diagonal components, the data was rotated to a new coordinate frame by considering the determined geo-electric strike angle in dimensionality analyses.

In two-dimensional modeling, RM2001 was applied to AMT data to perform joint inversion for TE- and TM-modes. The mesh size was taken as 199 x 141 while a uniform half-space with 100 Ωm electrical resistivity was used as an initial model. The error floors were chosen as 10% for apparent resistivity and 2.89° for phase. The regularization parameter (τ) and horizontal smoothing parameter (α') were chosen as 3 and 1, respectively. RM2001 reached the RMS value of 2.5 and produce the final model given in Figure 4.9.

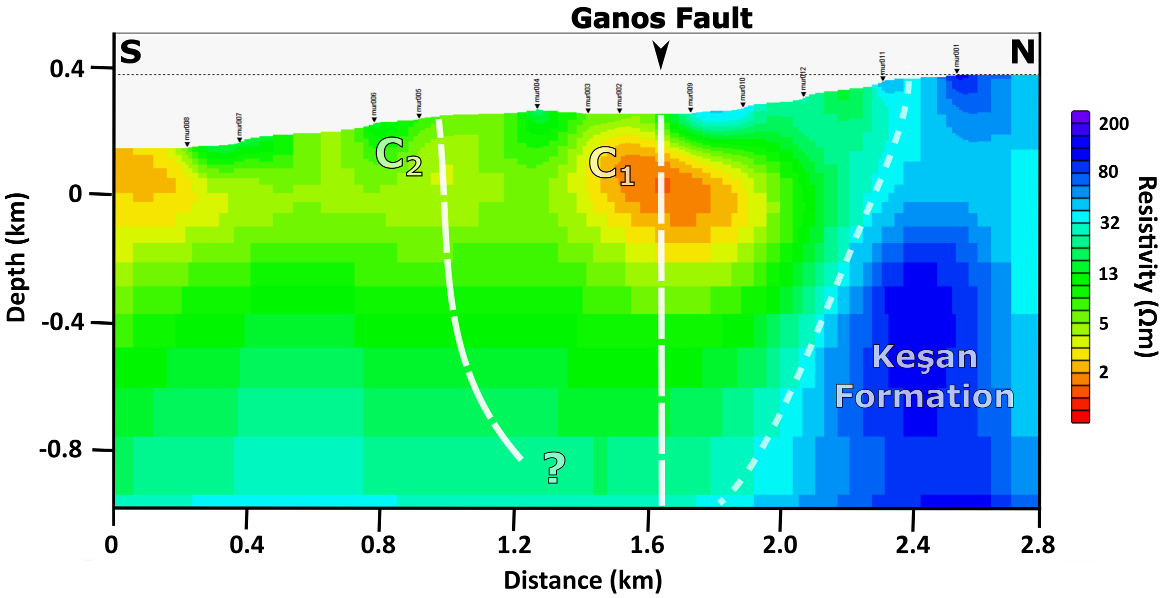

Figure 4.9. The resistivity model of AMT dataset developed by RM2001.

The second stage in evaluating AMT data is modeling with three-dimensional numeric routine of WSINV3DMT. The mesh was designed with evenly spaced 50 m grid nodes near the center of study field, while mesh size was taken as 48 x 28 x 50 including 7 air layers. With a similar approach to two-dimensional modeling, a uniform initial model with homogeneous 100 Ωm electrical resistivity was used. The thickness of first layer was selected as 10 m and the cell sizes were designed with a vertical increment factor of 1.3. For AMT data, WSINV3DMT ran with three periods per decade (17 in total) and error floors of the diagonal and off-diagonal components were chosen as 10.0 % and 5.0 %, respectively. The code ran 5 iterations until target RMS of 1.95 was acquired (Figure 4.10).

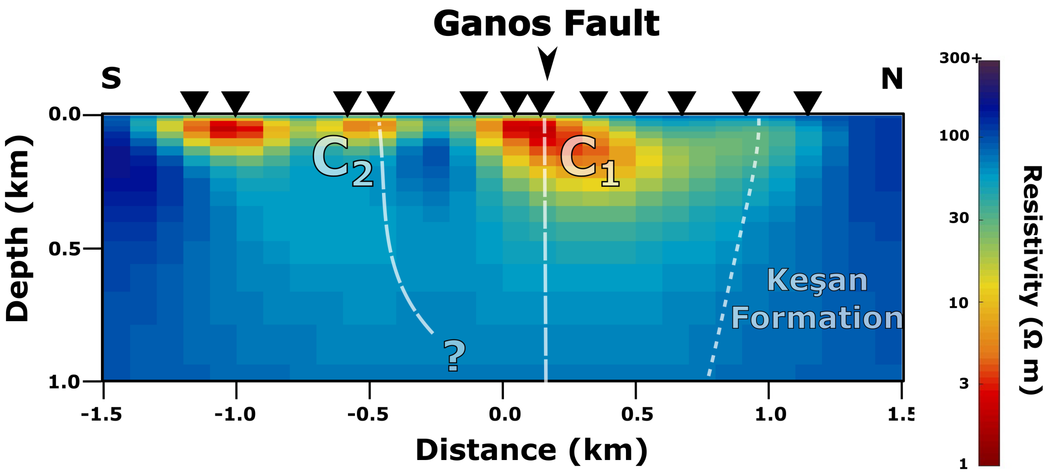

Figure 4.10. The resistivity model of AMT dataset developed by WSINV3DMT. Black triangles show the station locations. Thick dashed-lines indicates the fault locations. C1 and C2 anomalies are fault zone conductors of main Ganos Fault and subsidiary oblique strike-slip structure on the south, respectively. Color scale for the resistivity is logarithmic.

Evaluation of wide-band MT data required more complicated efforts because of larger data size (22 frequencies) and inherent coast effect (Parkinson, 1959). To represent Marmara Sea, eastern and southern sides of the initial model were fixed with 0.3 Ωm cells to overcome the coast effect. While the mesh size was taken as 52 x 52 x 50 (including 7 air layers) for MT data, the rest of the mesh was represented 100 Ωm cells. Evenly spaced 200 m grid nodes near the center of study field were used and the cell size increase with a factor of 1.3 again. Run of the code finished after 5^{th} iteration by finalizing at a model with RMS of 4.7 (Figure 4.11 and Figure 4.12).

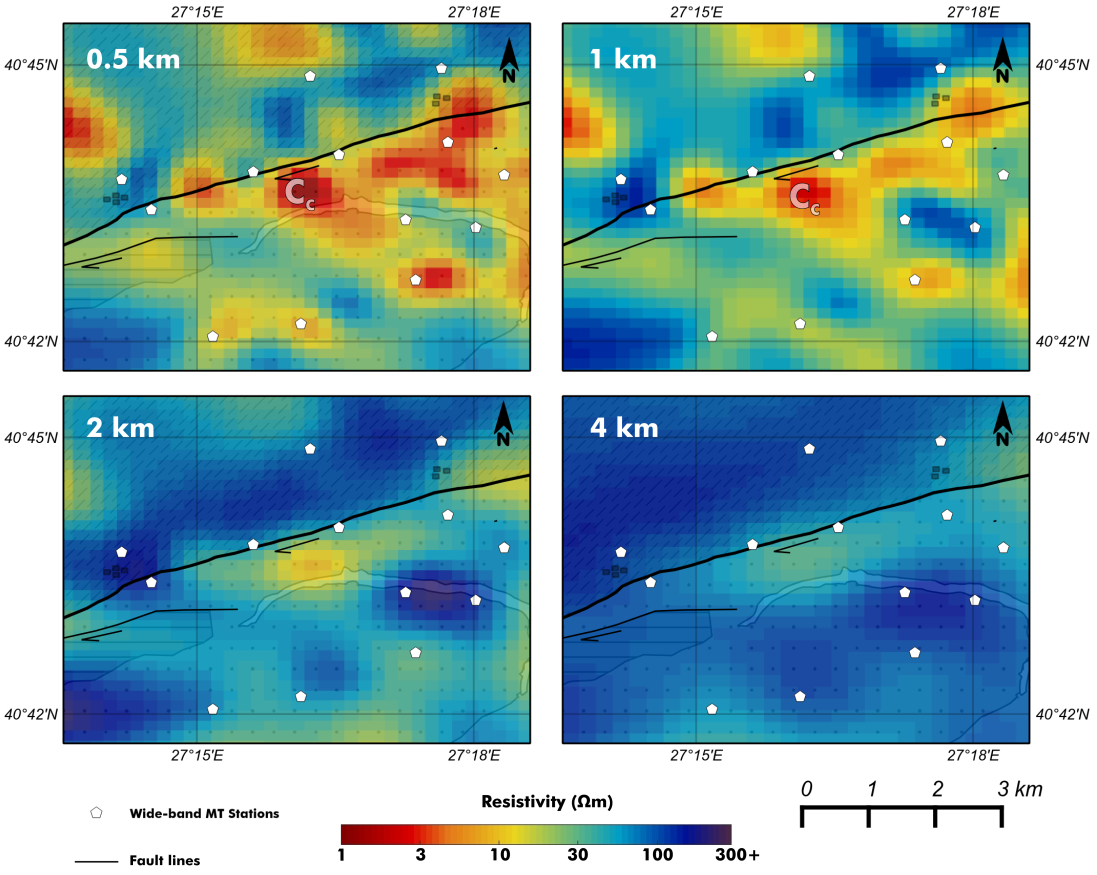

Figure 4.11. Resistivity depth sections obtained from inversion of wide-band MT data for 0.5 km, 1 km, 2 km and 4 km. Wide-band stations are indicated with white signs. Cc is the central conductor, a relatively more conductive region among the fault zone. Solid black lines illustrates the major faults in the region. Color scale for the resistivity is logarithmic.

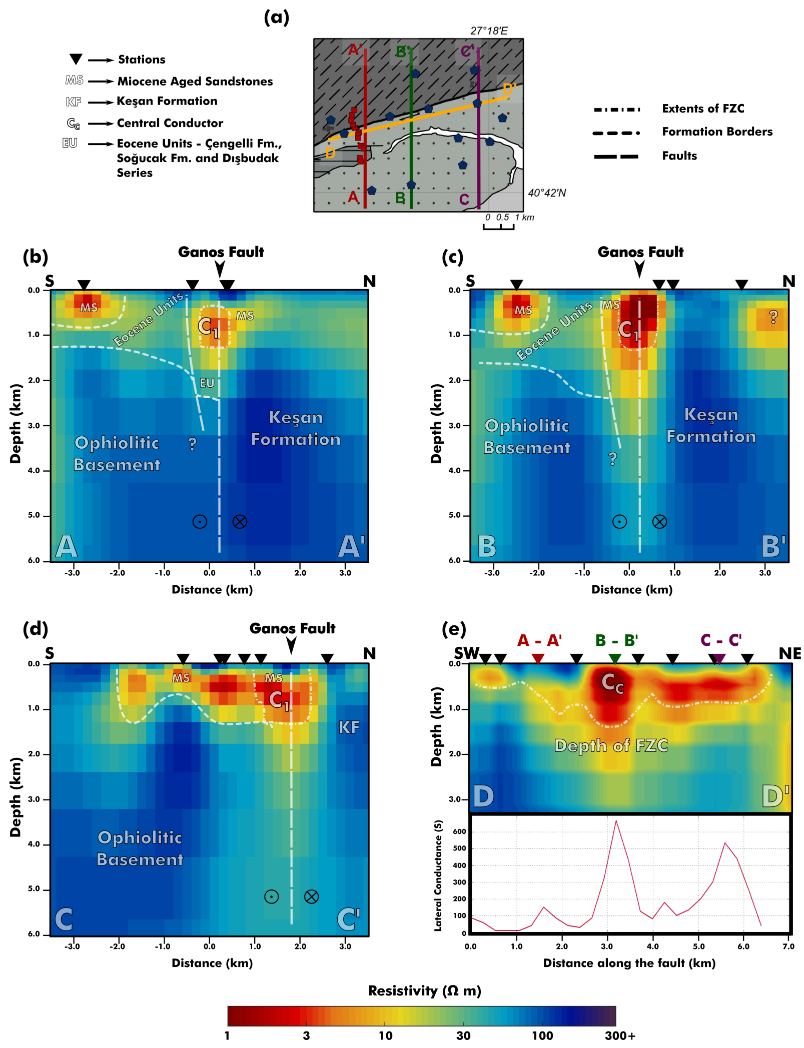

Figure 4.12. Cross sections of (b) - (d) extracted from resistivity model obtained from inversion of wide-band MT data with WSINV3DMT. (a) is the map representation of the locations of cross-sections. (b), (c) and (d) are the north-south aligned cross sections showing the spatial differentiation along the Ganos Fault for the geological structures, especially the damage zone. At all cross-sections, conductive C1 represents the fault zone conductor (FZC) of the main fault. (e) is a trans-section that goes parallel to the Ganos Fault that outlines the depth variation of FZC with additional information on lateral conductance values along the fault zone. Cc , central conductor, represents a relatively higher conductive region among the fault zone. Descriptions of different dashed lines,symbols and acronyms are given in the legend. Color scale for the resistivity is logarithmic.

In addition to WSINV3DMT; both datasets were modeled with another three-dimensional modeling routine, ModEM, to crosscheck the obtained results. Because purpose of using another routine is not to compare the modeling algorithms, different attributes were used for modeling process of ModEM. The error floors were assigned as 5% of square root $|\mathbf{Z}_{xy}\ \mathbf{Z}_{yx}|$ for all impedance tensor components. The mesh of ModEM was designed with evenly spaced 100 m grid nodes near the center of study field. Mesh size were determined as 39 x 21 x 30 with a uniform half-space made up by 100 Ωm valued cells increasing with a factor of 1.3 while the thickness of first layer was chosen as 10 m. ModEM iterated 22 times and obtained the final model with RMS of 2.8 (Figure 4.13).

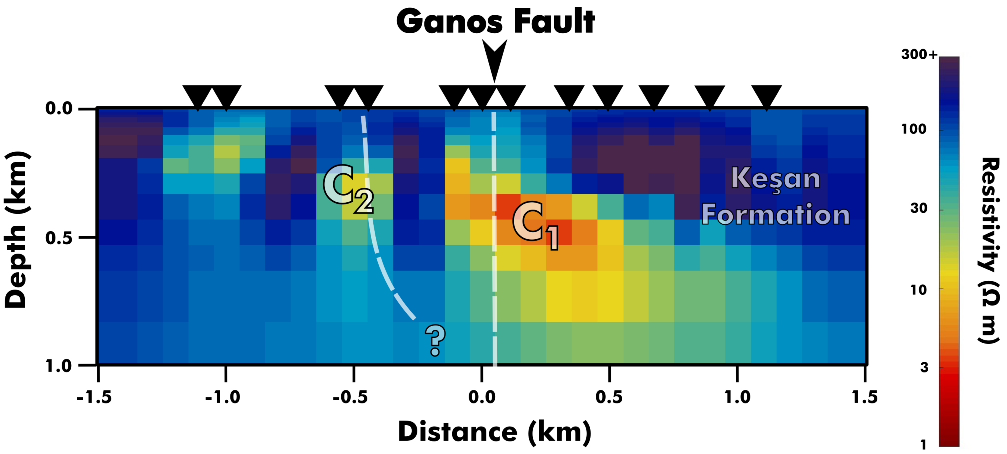

Figure 4.13. The resistivity model of AMT dataset developed by ModEM

For wide-band MT modeling of ModEM; mesh design was parallel to AMT processes. Almost the same geometrical approach with a broader structure was applied. The thickness of first layer was chosen as 100 m and the mesh was designed with evenly spaced 200 m grid nodes near the center of study field. Number of grid nodes were selected as 43 x 45 x 37 (including 7 air layers). Coast effect was implemented in similar manner parallel to WSINV3DMT modeling by fixing the values of the eastern- and southern-most cells to 0.3 Ωm. Run of ModEM attained in the resulting model at 112^{th} iteration with a final RMS of 3.4. Figure 4.14 shows the same four resistivity depth sections from ModEM that can be seen in Figure 4.11. The cross sections obtained from ModEM which are taken from same positions seen at Figure 4.12(a) are presented in Figure 4.15.

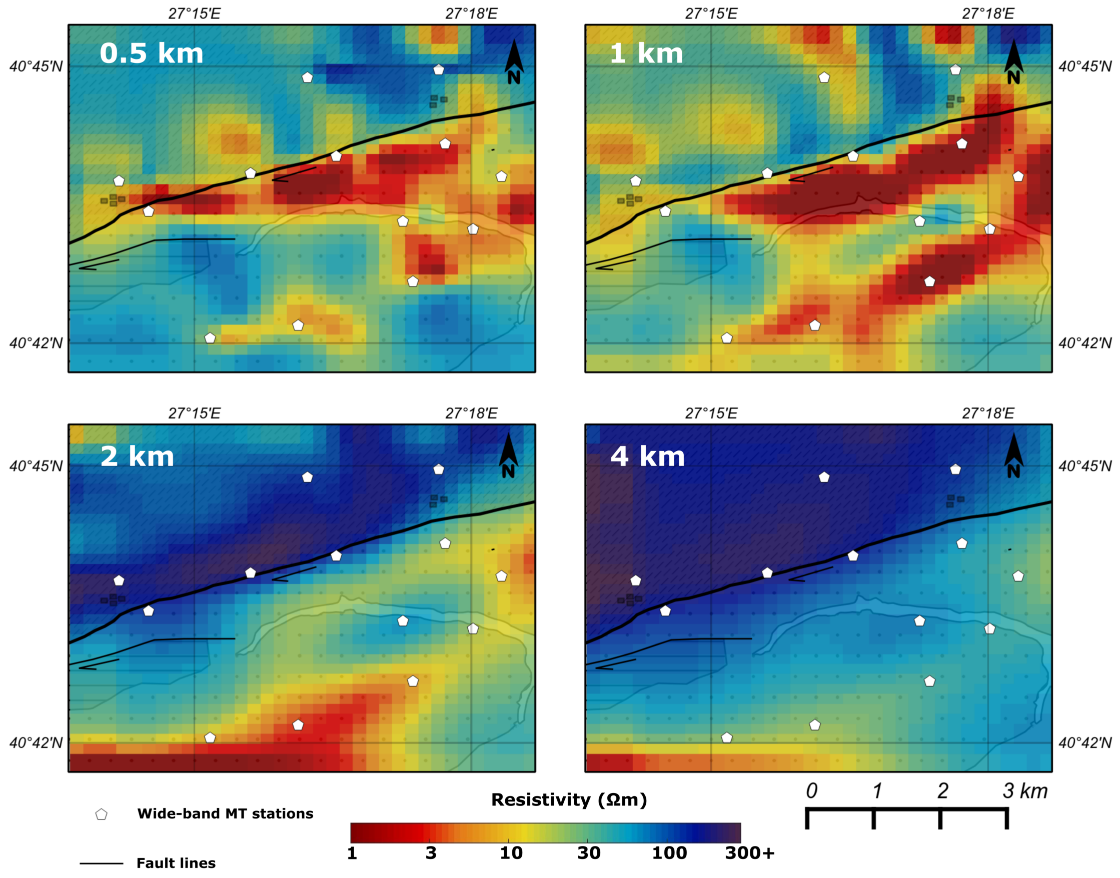

Figure 4.14. Resistivity depth sections obtained from inversion of wide-band MT data with ModEM for 0.5 km, 1 km, 2 km and 4 km

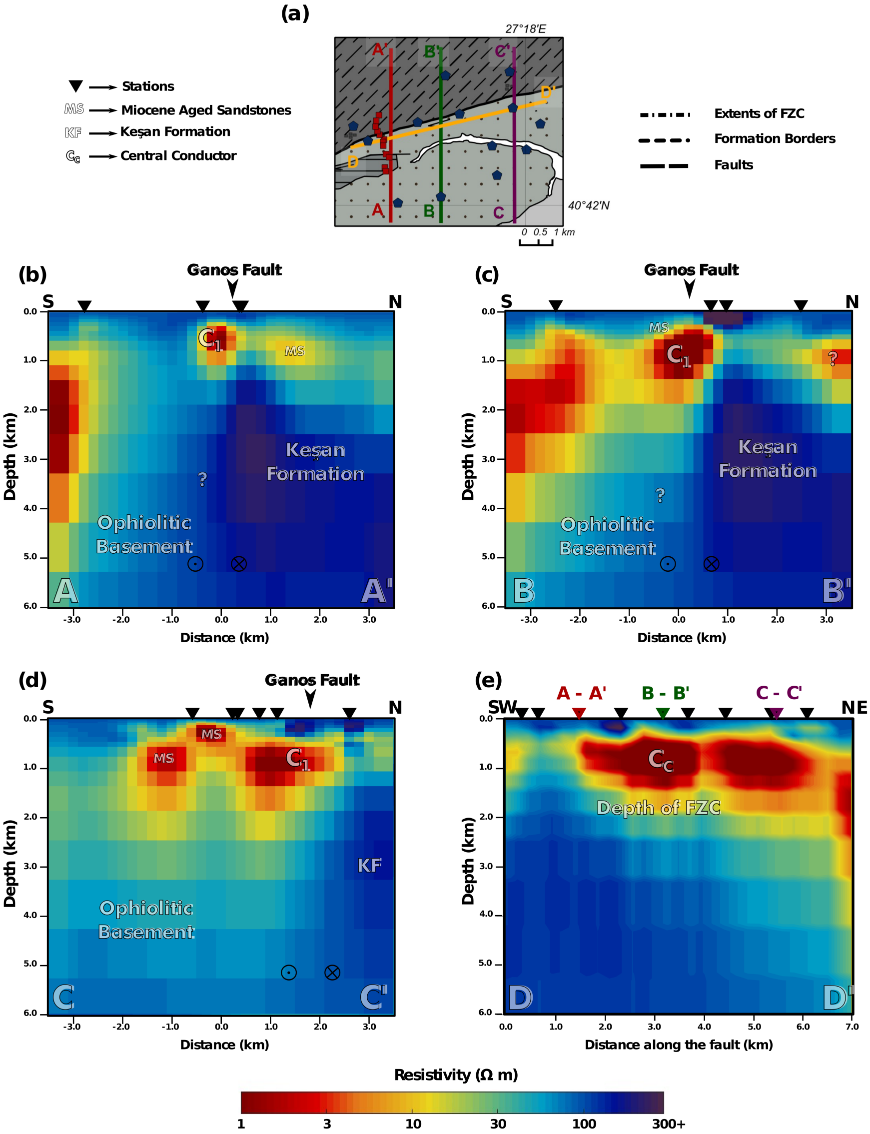

Figure 4.15. Cross sections of (b) - (d) extracted from resistivity model obtained from inversion of wide-band MT data with ModEM. (a) is the map representation of the locations of cross-sections. (b), (c) and (d) are the north-south aligned cross sections showing the spatial differentiation along the Ganos Fault for the geological structures, especially the damage zone. At all cross-sections, conductive C1 represents the fault zone conductor (FZC) of the main fault. (e) is a trans-section that goes parallel to the Ganos Fault that outlines the depth variation of FZC. Cc , central conductor, represents a relatively higher conductive region among the fault zone. Descriptions of different dashed lines,symbols and acronyms are given in the legend. Color scale for the resistivity is logarithmic.

When the results of two different three-dimensional modeling algortihms for both datasets, a good agreement between them can be easily noticed. Although they were utilized with independent parameters and ModEM includes additional tipper data, there is no significant discrepancy occurs that can cause misinterpretation if the models are considered individually.

4.4.1. Analyses of Models

Once the final resistivity models are presented, validity of results should be analyzed with fitting of data and additional tests. Here; in addition to pseudosections and fitting curves of all datasets, two sensitivity tests for three-dimensional modeling is given to check the credibility of modeling results.

Figure 4.16 illustrates the observed and calculated apparent resistivity and phase pseudosections of TE- and TM-modes after the rotation to N70^{o}E for two-dimensional modeling. In joint inversion of RM2001, both modes almost deliver a good fit for apparent resistivity and phases except little differences for the apparent resistivity of TE-mode at lower frequencies.

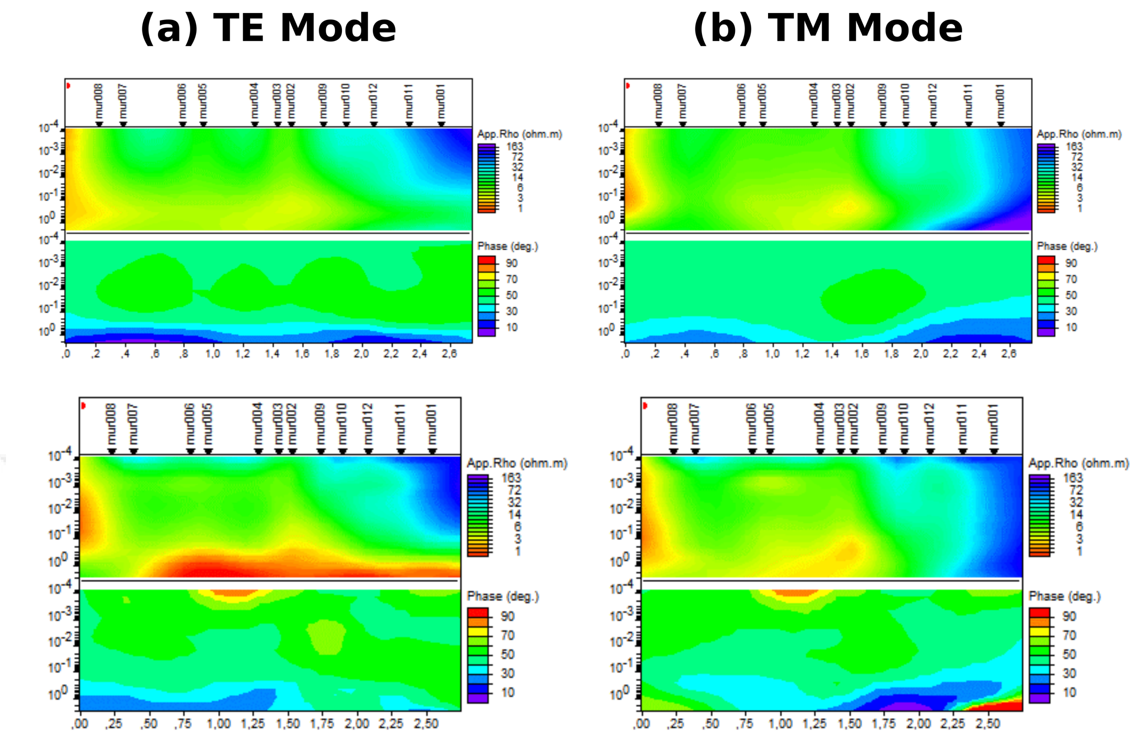
(a) TE Mode

(b) TM Mode

Figure 4.16. Calculated (top) and observed (bottom) apparent resistivity and phase pseudosections for (a) TE mode (b) TM mode.

In Figure 4.17, the presentation of the observed and calculated off-diagonal impedance components projected onto E-W and N-S oriented two pseudosections are given for wide-band MT data. The recovery of all components generally exhibits high levels, but some unwanted effects can be seen in the lower frequencies corresponding to very deeper parts which are not considered as target depth.

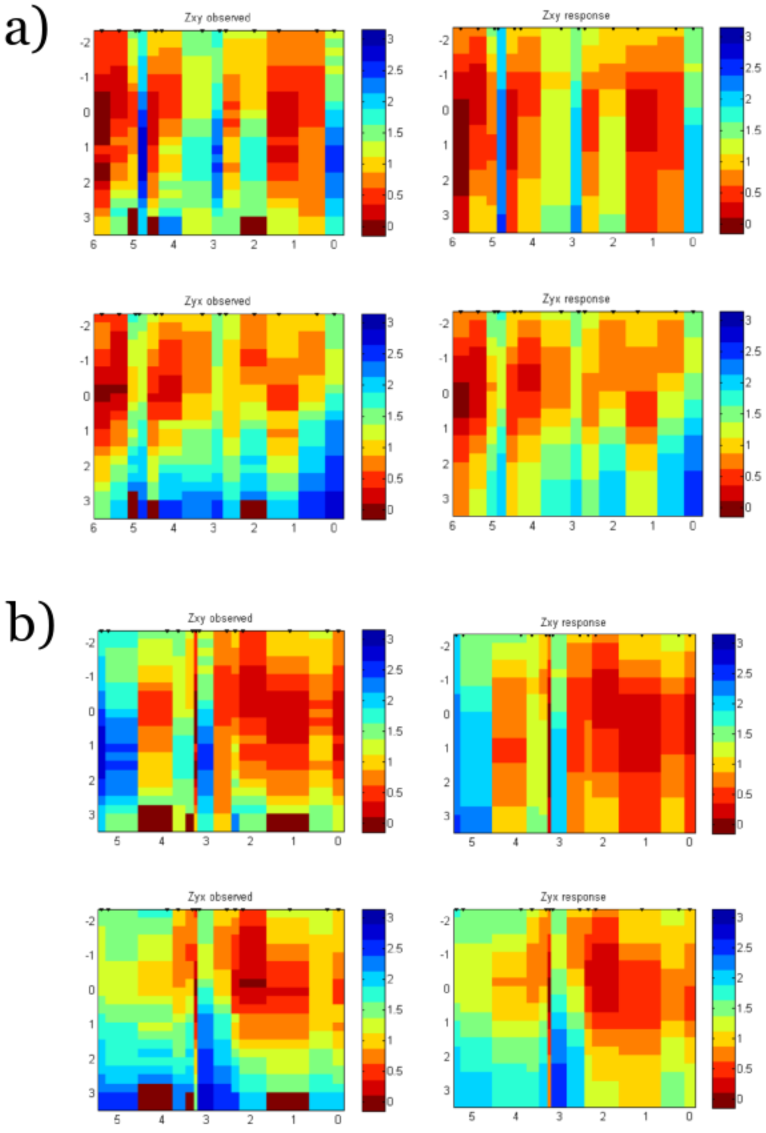

Figure 4.17. Comparison of observed and calculated impedance values as pseudosections in (a) E-W (b) N-S direction. All stations are projected on an corresponding arbitrary lines.

When fitting curve each station is independently examined, well coherency between observed and calculated impedance components can be seen for AMT dataset.

Taking into consideration that the diagonal components have very small values, their contribution will be less effective in the modeling. Since off-diagonal elements play more important role, correlation between their observed and calculated apparent resistivity and phase values determines the validity of modeling (Figure 4.18).

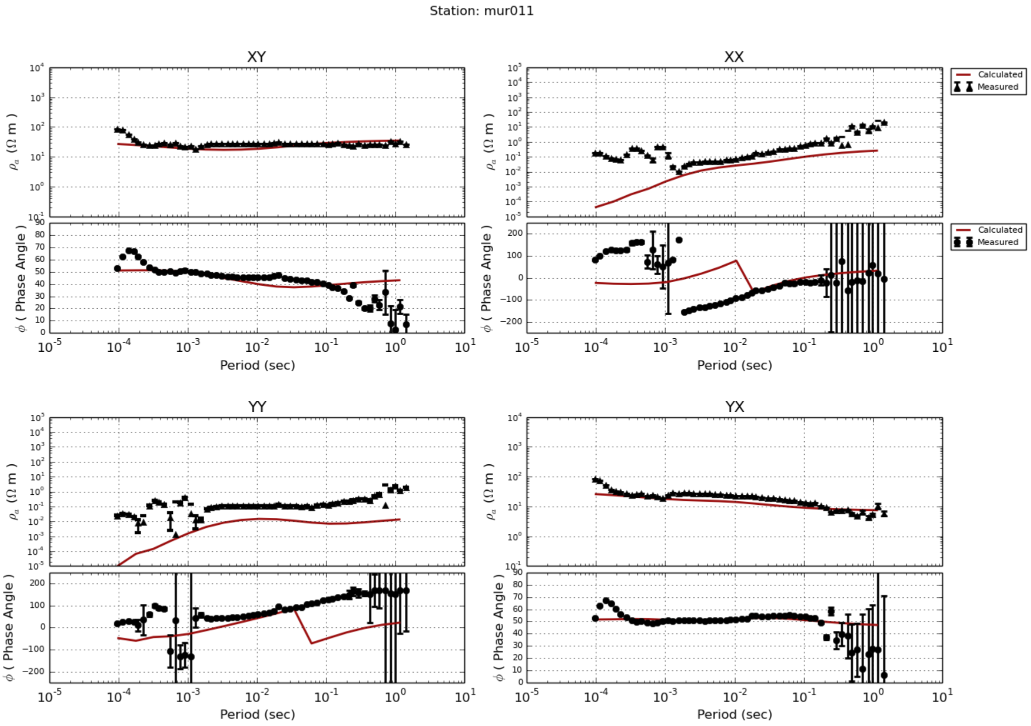

Figure 4.18. Apparent resistivity and phase fitting curves of station MUR011, attained from three-dimensional modeling for all components.

Similar well correlations are also seen for wide-band MT data especially in higher frequencies which are corresponding to target depth. Considering the very conductive structure of study field in the light of skin depth phenomena, an extenuated target depth will become acceptable. Moreover, presence of powerful coast effect in the study area is previously detected with induction arrows. This situation explains the decline in the coherence of apparent resistivity and phase values with respect to decreasing frequencies (Figure 4.19).

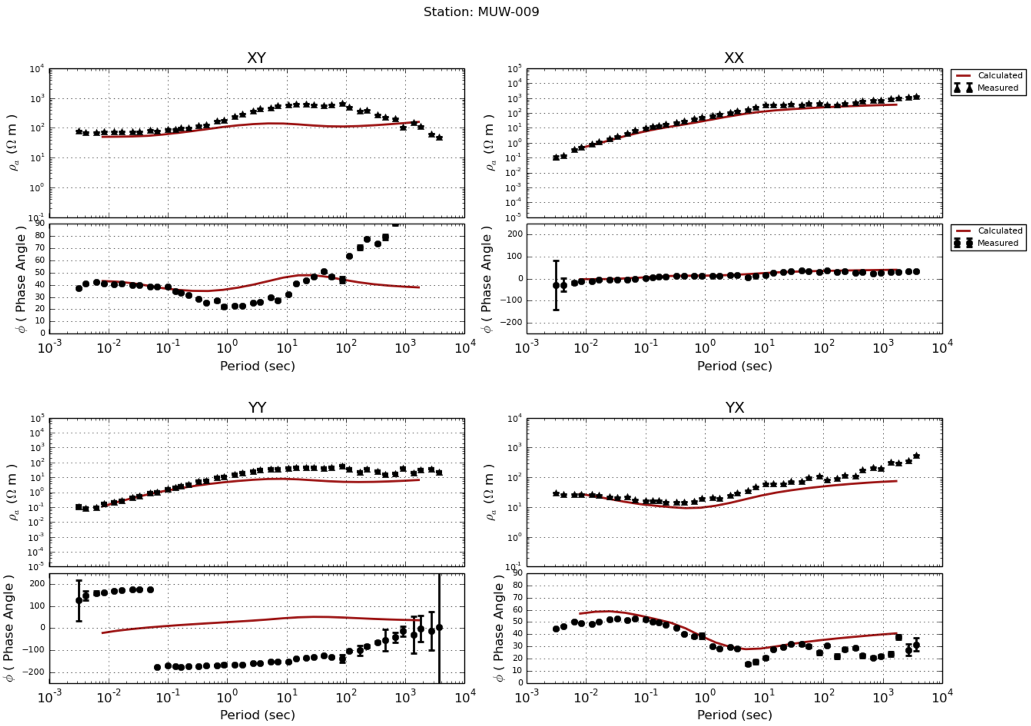

Figure 4.19. Apparent resistivity and phase fitting curves of station MUW-009, attained from three-dimensional modeling for all components.

To test the validity and dimensions of the conductive areas in the final wide-band MT model, different sensitivity tests were applied. In the first test, the forward modeling responses were computed to check the validity of the conductive areas in WSINV3DMT model. A block with 300 Ωm resistivity was embedded into the model to replace the conductive areas reaching to a depth of 2000 m from the surface. This test certified the requirement for a conductive zone along the fault. Another sensitivity test was executed to identify the thickness of the conductive areas. In this test, forward responses were calculated for four different conditions with a deep resistive block (with 300 Ωm resistivity) present at different depths (1800 m, 1200 m, 600 m and 300 m). Figure 4.20 shows the model responses for these forward runs for two sites that are positioned above the anomalous region. This second test reveals that the conductive areas reach to a depth of approximately 600 to 1200 m, while being shallower at the west of the study area.

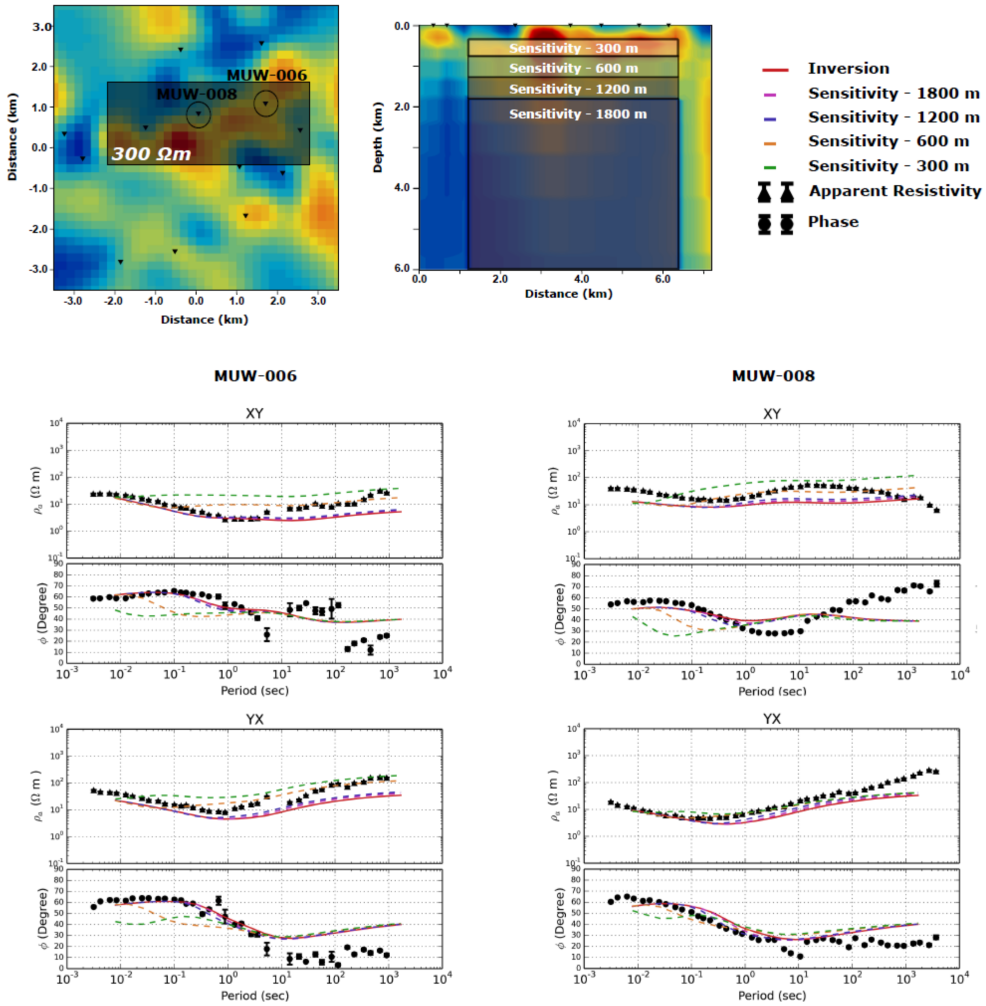

Figure 4.20. Results of the sensitivity tests at stations MUW-006 and MUW-008 for WSINV3DMT model. The inversion responses and different sensitivity experiments are indicated with individually colored curves.

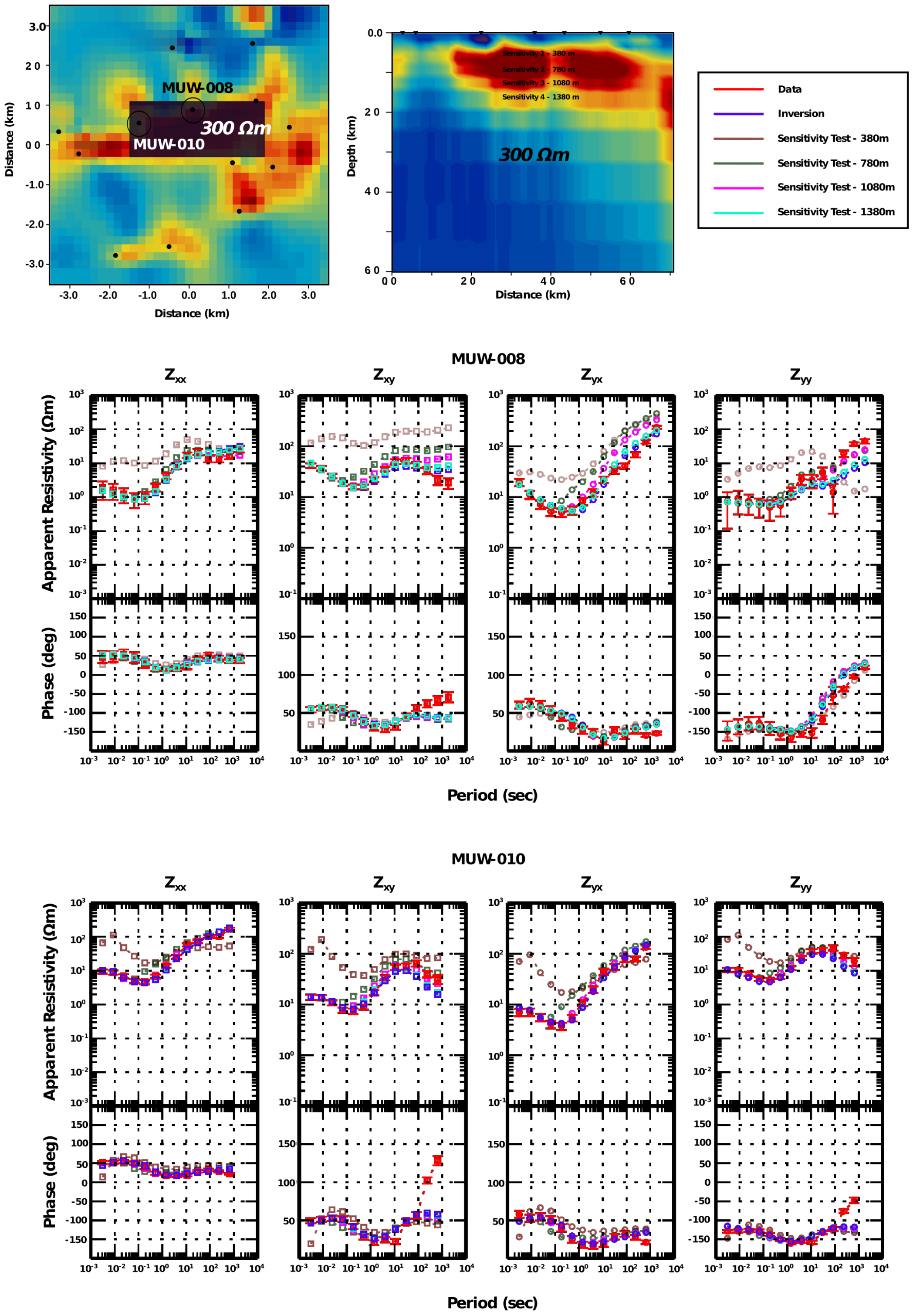

Figure 4.21. Results of the sensitivity tests at stations MUW-006 and MUW-008 for ModEM model. The inversion responses and different sensitivity experiments are indicated with individually colored curves.

For ModEM results, validity of the FZC was tested on the final model with another sensitivity test. To determine the spatial dimensions of the FZC, inversion responses after one iteration were computed for four different cases with a deep resistive block (with 300 Ωm) starting from different depths (1380 m, 1080 m, 780 m and 380 m) to the base of the model. Installing a resistive block up to the shallower depths where FZC reaches, caused an increment at the RMS values. Corresponding values are as follows: 1380 m: 3.42, 1080 m: 3.72, 800 m: 4.6 and finally 380 m: 7.77. Model responses for these inversions are shown on Figure 4.21 for two sites that are located above the anomalous region. In addition to RMS values, fitting of the data clarified that model is sensitive to the relevant anomalies and conductor has a valid presence.

5. DISCUSSION

In this study, electrical conductivity structure of Ganos Fault is revealed by evaluating two- and three-dimensional models of high-resolution AMT and wide-band MT data. With a geological point of view, one may have prima facie claims to locate the potential fault line on the obvious resistivity contrast. Nevertheless, induction arrows clearly suggest the presence of a cogent anomaly just south of this conductive-resistive boundary. This anomaly refers the idea of Bedrosian et al. (2004) and Ritter et al. (2005) over the indications about the vertical transfer function data and fault zones, thus points out a more accurate location for the fault. By confirming induction arrow results, both two- and three-dimensional AMT models also exhibit a highly conductive anomaly (C1) for the same location. According to these models, the anomaly can be approved as the fault zone conductor (FZC) of the main fault, that has 700 m width while extending to depth of $\sim$300 m.

Lateral conductance is a derived parameter which is basically calculated as the width over average resistivity of the FZC. Since the FZC which is determined in AMT models has a lateral conductance value of $\sim$80 S, section from the wide-band MT model at the same location gives values between 40–85 S. This range of lateral conductance values and depth extent of FZCs prove that AMT and MT results promote each other in a way that models conform with the previous descriptions of correlations between fault characteristics and FZC properties (Table 5.1)(Hoffmann-Rothe et al., 2004; Ritter et al., 2005). On the other hand, lateral conductance values along the GF vary between 40 - 515 S when they are calculated from wide-band MT model (Figure 4.12). These fluctuating values might be related to lightly consolidated and widely distributed Miocene sandstones located at the south of the fault, as well as an asserted subsidiary branch which starts from the central conductor (C_c) (Figure 4.11) until ending near Gaziköy (Aksoy et al., 2010). The central conductor (C_c) is located on a position where the highest lateral conductance (Figure 4.12) and β values (Figure 4.7) are detected. While moving to west from this anomaly, characteristics of FZC starts to change both in depth extent and conductivity, thus suggests a presence of a particular geological setting. Maximum rupture in 1912 Mürefte earthquake (Aksoy et al., 2010; Meghraoui et al., 2012) was potentially seen near this zone, but still further geological discussions are required to clarify the dynamic meaning of this large conductive area.

Table 5.1. Comparison of MT studies across the Arava Fault (Dead Sea Transform, Lebanon), the West fault system (Chile), the San Andreas Fault (United States of America) and Ganos Fault. The current state of deformation at the segments are referred as recent activity (Edited from Hoffmann-Rothe et al., 2004 and Ritter et al., 2005.).

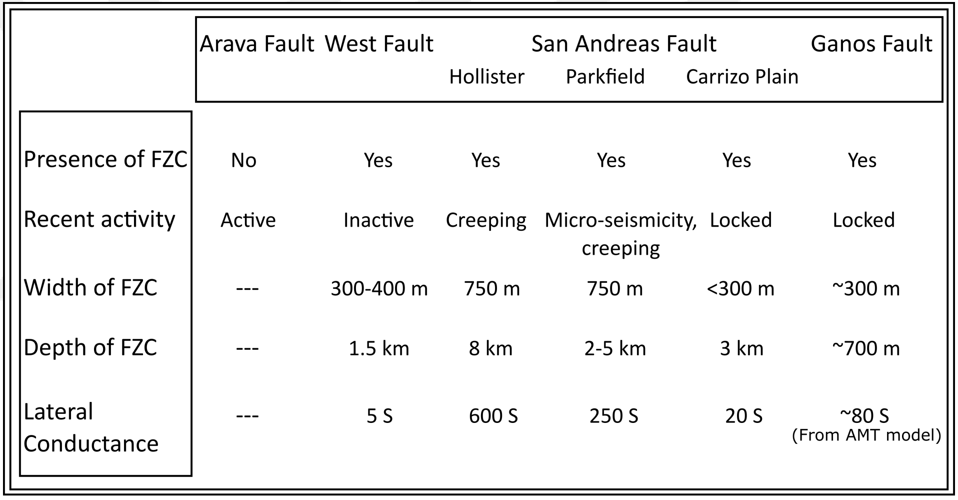

	Arava Fault	West Fault	San Andreas Fault			Ganos Fault
			Hollister	Parkfield	Carrizo Plain	
Presence of FZC	No	Yes	Yes	Yes	Yes	Yes
Recent activity	Active	Inactive	Creeping	Micro-seismicity, creeping	Locked	Locked
Width of FZC	---	300-400 m	750 m	750 m	<300 m	~300 m
Depth of FZC	---	1.5 km	8 km	2-5 km	3 km	~700 m
Lateral Conductance	---	5 S	600 S	250 S	20 S	~80 S (From AMT model)

Investigating the properties of FZCs plays an important role to understand seismic characteristics of faults. Tank (2012) compared the FZCs of two different faults which are seismically active İzmit–Adapazarı Fault (IAF) and dormant İznik-Mekece Fault (IMF). Although both fault branches associate with the same fluid source at the seismogenic depths (Tank et al., 2005), the shallow structures have different attributes, which are linked with seismicity and related deformation. Two profiles along IMF reveal that the FZC properties can show difference for being related with local geological structures. In this study, FZC lateral conductance homogeneity along the fault is determined as unequable at fluid-rich zones especially, due to the rapid deviations arise in short distances. However, depth extent of FZC may provide more useful information to interpret seismicity where it governs the rheological response of fault zones as a controlling parameter.

The damage zone of GF is broadly distributed over conductive areas in the resistivity models. As stated in fault fluid-flow models of Caine et al. (1996), it is unlikely to remark a barrier-like mechanisms at GF, because the damage zone occupies a very large place when it is compared with core's width. Hence, fluid transfer behavior of GF can be categorized as distributed conduit in reference to its spatial extensions. Previously, Janssen et al. (2009) suggested that the damage zone of GF consists of anastomosing strands of fault gouges, which was observed at the Carboneras Fault (CF) in Spain (Faulkner et al., 2003) instead of a continuous main fault. Despite resolving the subsidiary gouge layers through the resistivity models needs complex efforts; to verify such a model, high electrical anisotropy levels should dominate all around the study area. Such a situation was also previously suggested by Ritter et al., (2005) over the investigations on Waterberg Fault, Namibia (Weckmann et al., 2003). However, there is no confirmation for such levels of anisotropy at GF when the stability of geoelectric strike directions for different decades was examined with phase tensor analyses of wide-band data. In addition to low levels of anisotropy, the FZC of the main fault is relatively dominant than the subsidiary FZCs. In terms of both geometrical positioning and fracture density, therefore, the fault zone structure of GF is more similar to Punchbowl Fault (PF), Southern California (Schulz and Evans, 2000) rather than CF.

Damage zone of GF is asymmetrical around the axes determined by core's alignment and almost-merely densifies on the south of this axes. Because of the difference between lithology of relevant geological structures, asymmetric damage zones exhibit mechanical strength contrast between two sides of faults (Ritter et al., 2005). This strength contrast occurs between poorly-lithified Miocene sandstones on the south and Eocene aged consolidated sandstone -shale intercalation which is named as Keşan Formation on the north (Okay et al., 2010). A plausible environment for the creation of an asymmetric damage zone may be provided by this strength contrast at shallow depths. As previously seen at PF, the same distinctive characteristic of GF is the possession of an asymmetry which is created by a large number of overlapping damage zones. However, fractures at the vicinity of PF have a denser distribution rather than subsidiary faults around GF, as a consequence a wide interconnected gouge system is not developed for GF. Yaltırak and Alpar (2002) and Okay et al. (2010) suggested the presence of several auxiliary faults in the study area and conductive C_2 anomaly represents the most prominent subsidiary fault on the south of GF (Figure 4.9 and Figure 4.10). Damage zones of these faults merge together as conductive areas and form a negative flower structure around GF. However, this wide weakness area only reaches a maximum at $\sim$1000 m depth. This situation defines the position of a mechanically strong protolith which corresponds to the ophiolitic basement (Figure 4.12).

Projecting earthquake hypocenters onto resistivity models allows the examination of relationship between fluids and occurrence rate of earthquakes. Although there are a few studies that advocate other options, most of MT studies reveal that earthquake activity in fault systems tends to concentrate near conductive-resistive interfaces, generally in the resistive side (Unsworth et al., 1997; 1999; Ogawa et al., 2001; Mitsuhata et al., 2001; Bedrosian (et al., 2002; Goto et al., 2005; Tank et al., 2005; Gürer and Bayrak, 2007). This situation was reasoned by effective normal stress reduction or rheological alteration in the boundary by fluid migration from conductive zones through resistive blocks (Wannamaker et al., 2004). General distribution of local earthquakes is lined up just north of the GF which is represented as resistive side whereas some outliers draw attention on the south of our study area. However, making such a conceptual consideration will cause misguidance because of lacking seismic and micro-seismic events recorded (Janssen et al., 2009; Öztürk et al., 2015). Here, earthquake occurrence rate shows gradual decline while moving from Marmara Sea to the terrestrial GF. Between Gaziköy and Mursallı, presence of several oblique-thrust systems surrounding the GF is suggested by Kalafat, (1995); Yaltırak and Alpar, (2002) and Okay et al. (2004). Probably, most of the earthquakes in the region were generated by these subsidiary faults rather than the main fault.

Wide-band MT models clarify that no fluid pathways derived from greater depths provide the fluid supply at shallow fault zone. Therefore, the FZC of the fault must consist of meteoric fluids as previously suggested by geochemical analyses of Janssen et al. (2009). Miocene aged poorly-lithified sandstone which appears in highly conductive areas, acts as a reservoir and entraps meteoric fluids at the vicinity of the fault. Although GF juxtaposes the resistive northern rocks with the conductive and mechanically weak formations which lie at shallower areas, the resistivity contrast diminishes with respect to depth and highly resistive blocks start to stand out at both sides of the fault. This situation points out an absence of fluids that impose additional pressure into stress equilibrium of the fault. Without any fluid-assisted weakening, the frictional stress of asperities can be maintained by stable formations (Brodsky and Kanamori, 2001) and thus plausible environment for a conspicuously inactive locked fault is provided. Here, the scarcity of seismic activity on the main fault may be elucidated by fault-fluid relations observed on this segment which is characterized by the absence of fluid flow into fault zone at seismogenic depths. In the Figure 5.1 the conceptual tectonic sketch summarizes the electrical properties of the region explicated from the results mentioned above. To develop a clearer picture on fluid's role on seismicity of GF, a more detailed investigation targeting at greater depths should be carried out.

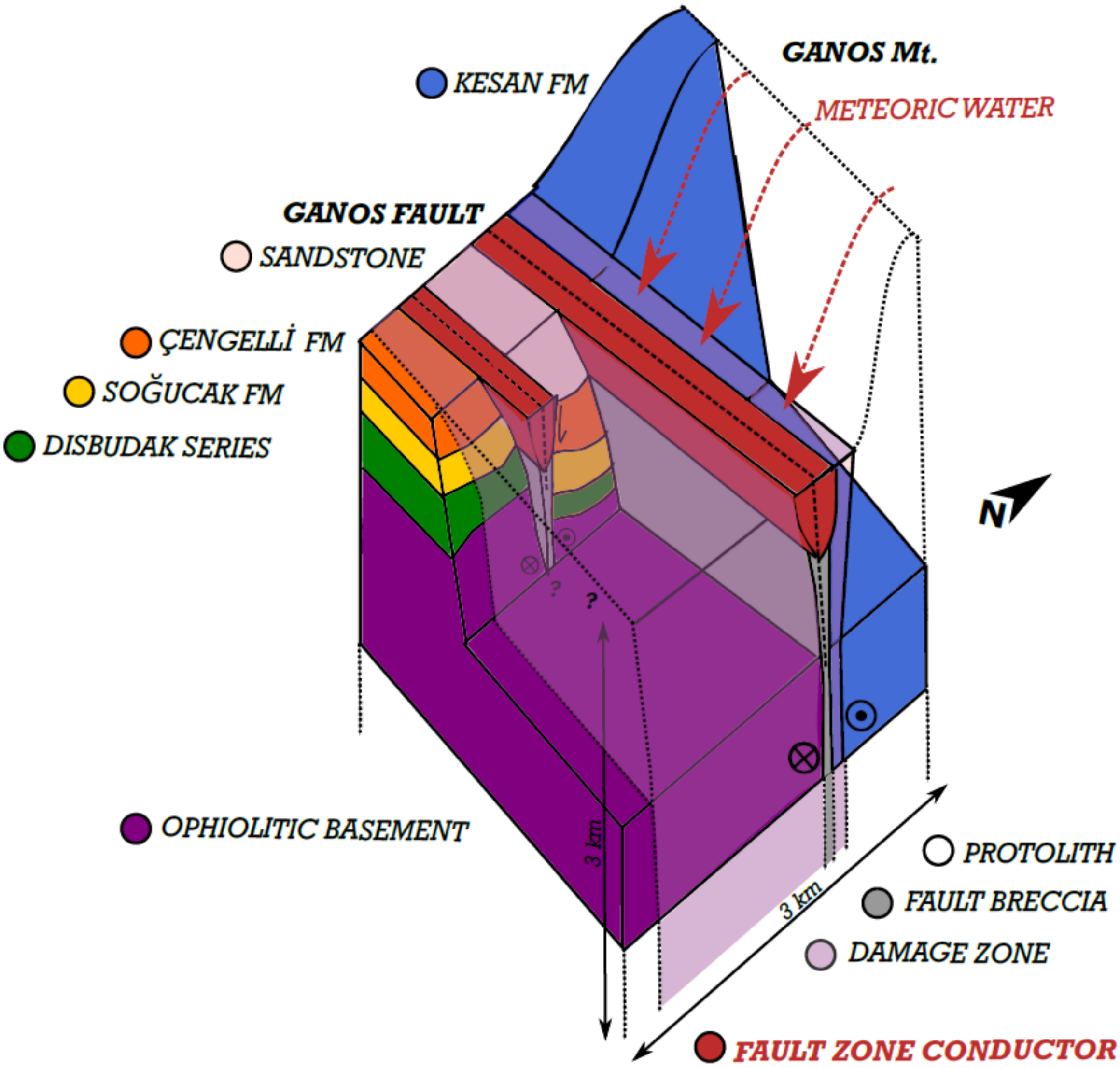

Figure 5.1. Conceptual sketch of geological interpretations of the magnetotelluric study results. A fluid-bearing asymmetric damage zone representative of resistivity models is drawn around Ganos fault. The possible flower structure formed by main strand and oblique subsidiary fault on the south are illustrated.

6. CONCLUSION

In this thesis, first systematic MT investigation was performed on Ganos Fault, at the vicinity of the epicenter of 1912 Mürefte Earthquake ($M_w = 7.4$). Dimensionality analysis and two- and three-dimensional inversions for both AMT and wide-band MT datasets were evaluated to decipher the conductivity structure and yielded the results presented here. In addition to two-dimensional attempts, applying the analysis in three-dimension allowed to detect highly varying lateral conductance values along the Ganos Fault. Ganos Fault consists of numerous subsidiary fracture zones around the main fault, that were identified with individual fault zone conductors. Widely extending damage zone of Ganos Fault contains these fault zone conductors and demonstrate an asymmetric damage zone which is concentrated on the south where the younger formations create a reservoir for meteoric water. A distributed conduit behavior for the fluid flow at the vicinity of Ganos Fault is revealed by considering the spatial attributes. Calculations of the geo-electric strike angle with different approaches resulted in a good agreement with geological strike angles and follow a N70°E trend. In addition to mechanically strong-resistive media at the both sides of the fault, absence of fluid pathways derived from greater depths might indicate a locked state for the fault and this situation signifies an important potential to produce a large earthquake in the future.

APPENDIX A: FITTING CURVES OF AMT DATA FOR THREE-DIMENSIONAL MODELING

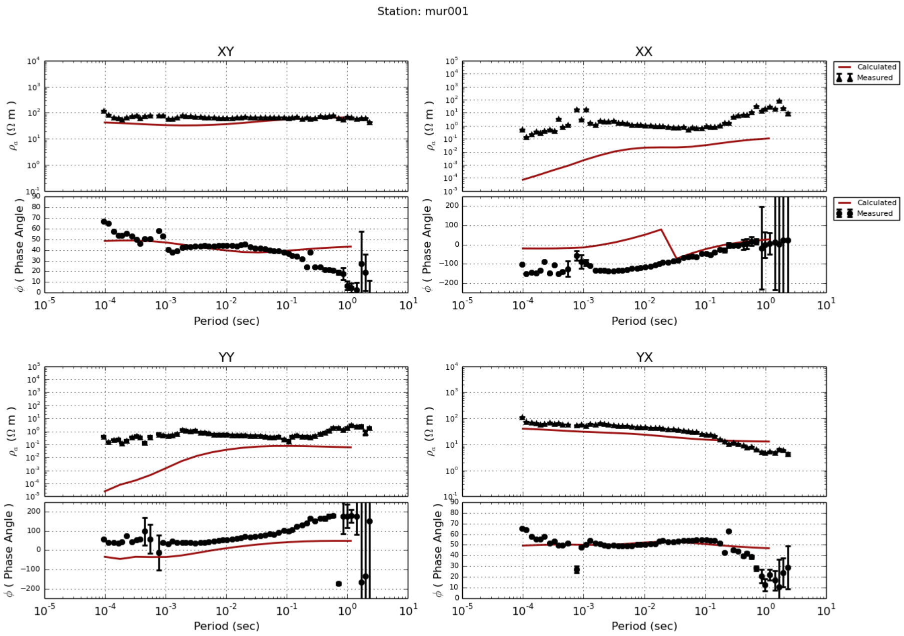

Figure A.1. Apparent resistivity and phase fitting curves of station MUR001, attained from WSINV3DMT for all components.

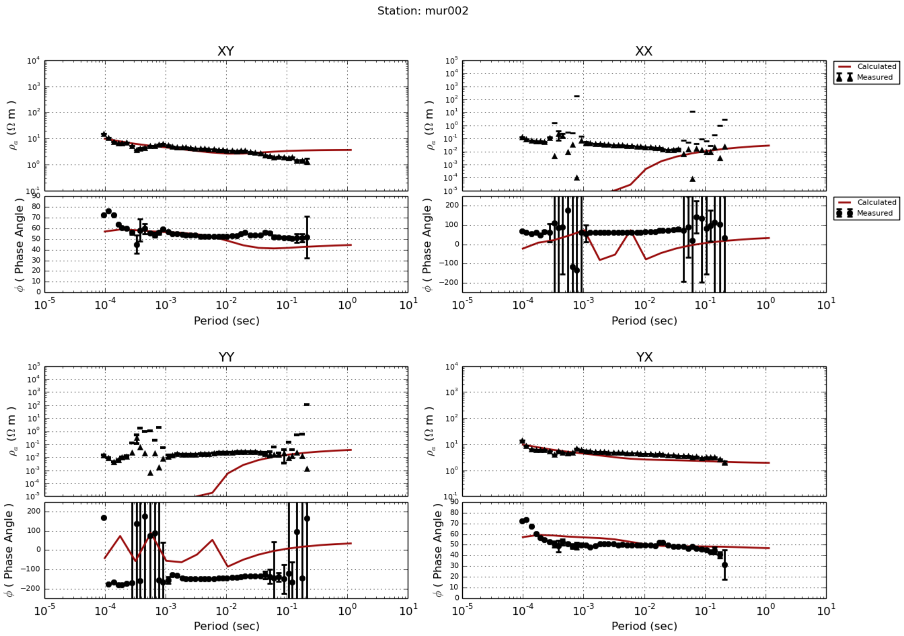

Figure A.2. Apparent resistivity and phase fitting curves of station MUR002, attained from WSINV3DMT for all components.

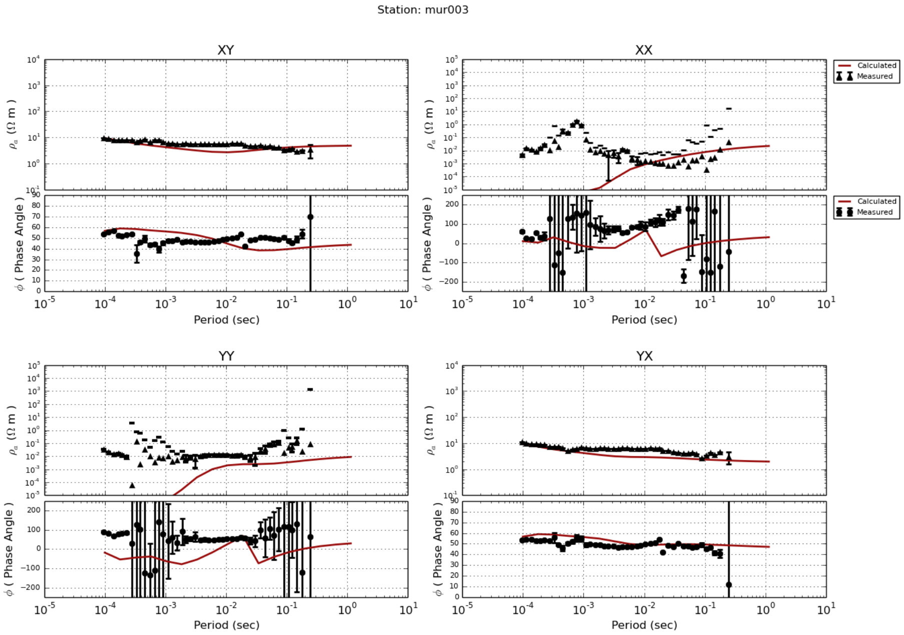

Figure A.3. Apparent resistivity and phase fitting curves of station MUR003, attained from WSINV3DMT for all components.

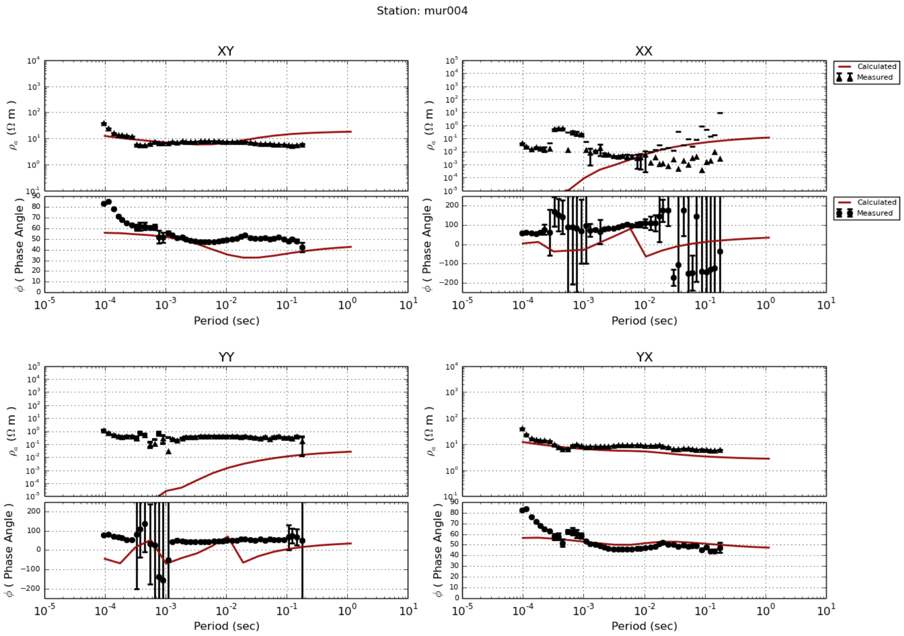

Figure A.4. Apparent resistivity and phase fitting curves of station MUR004, attained from WSINV3DMT for all components.

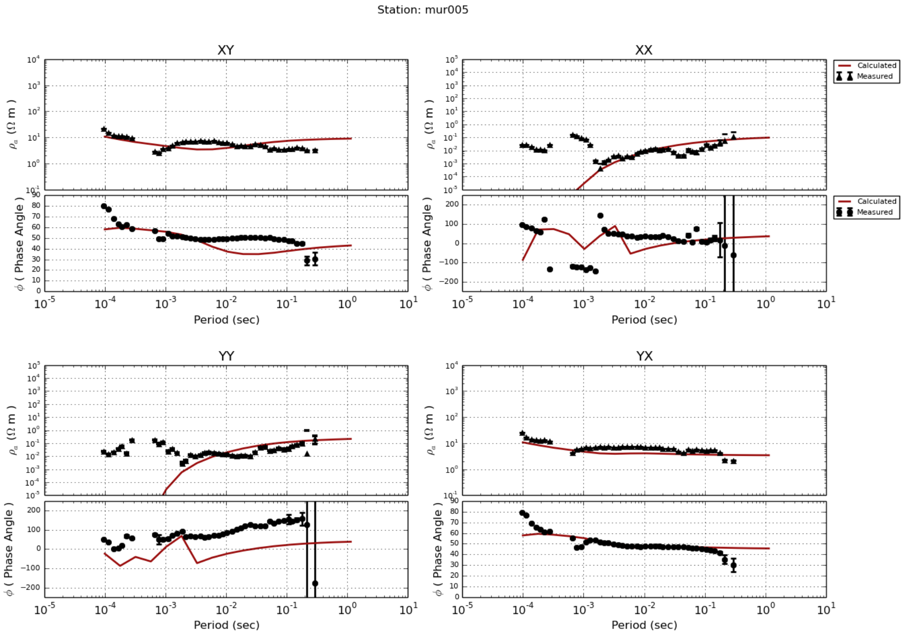

Figure A.5. Apparent resistivity and phase fitting curves of station MUR005, attained from WSINV3DMT for all components.

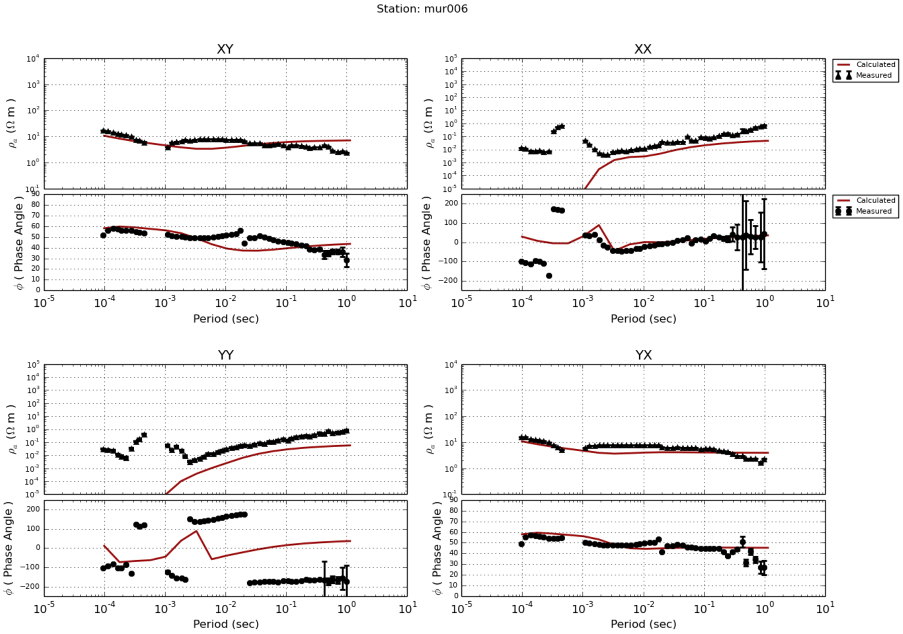

Figure A.6. Apparent resistivity and phase fitting curves of station MUR006, attained from WSINV3DMT for all components.

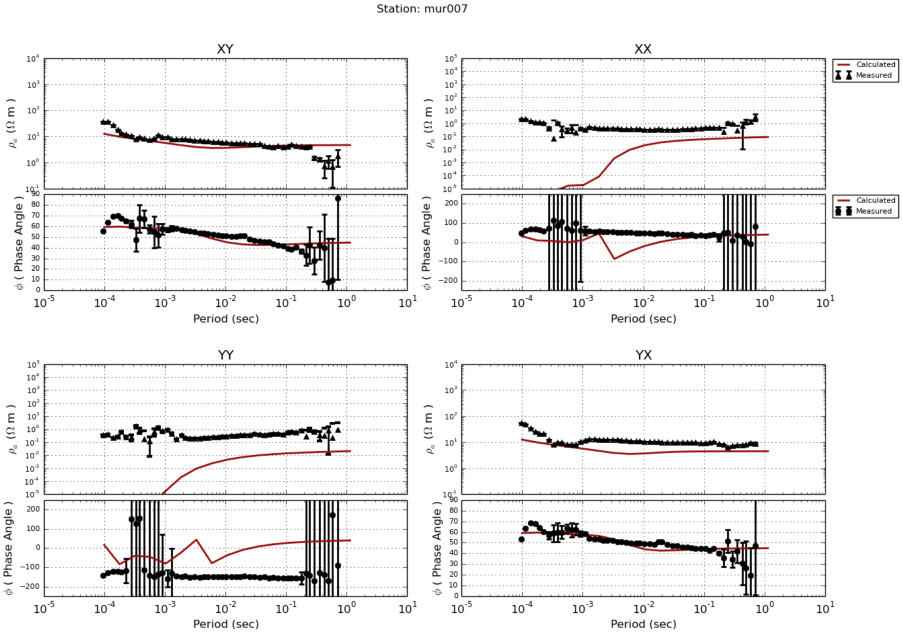

Figure A.7. Apparent resistivity and phase fitting curves of station MUR007, attained from WSINV3DMT for all components.

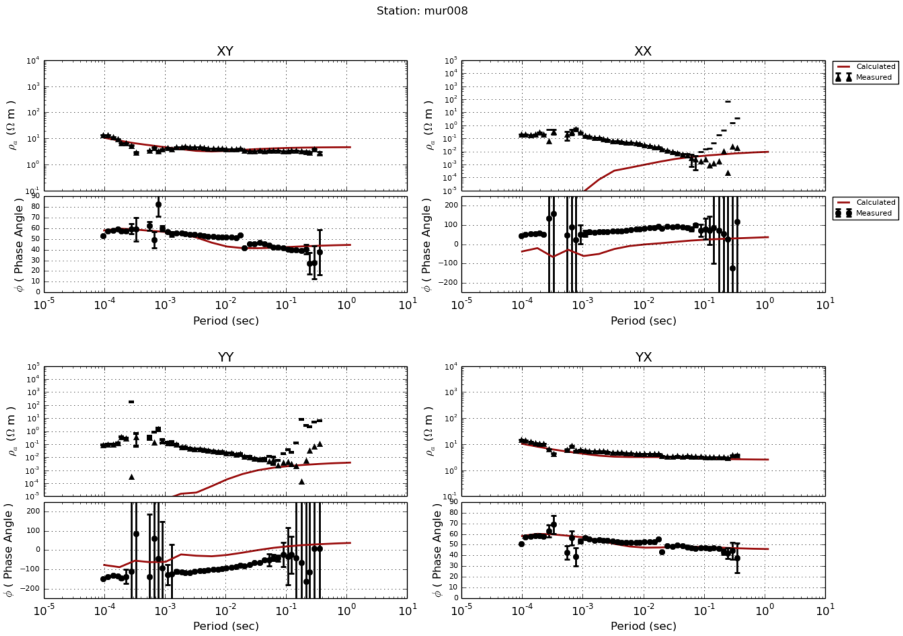

Figure A.8. Apparent resistivity and phase fitting curves of station MUR008, attained from WSINV3DMT for all components.

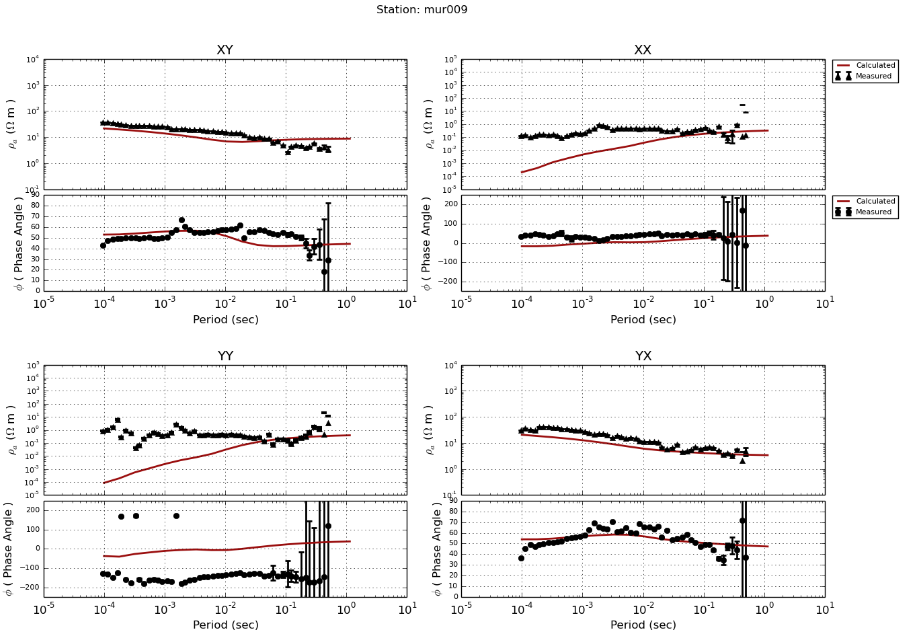

Figure A.9. Apparent resistivity and phase fitting curves of station MUR009, attained from WSINV3DMT for all components.

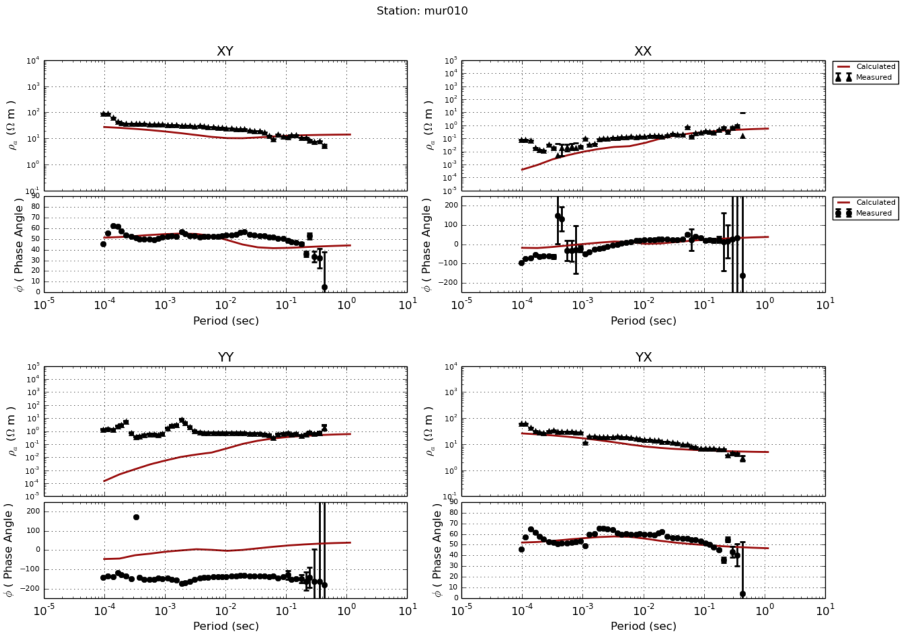

Figure A.10. Apparent resistivity and phase fitting curves of station MUR010, attained from WSINV3DMT for all components.

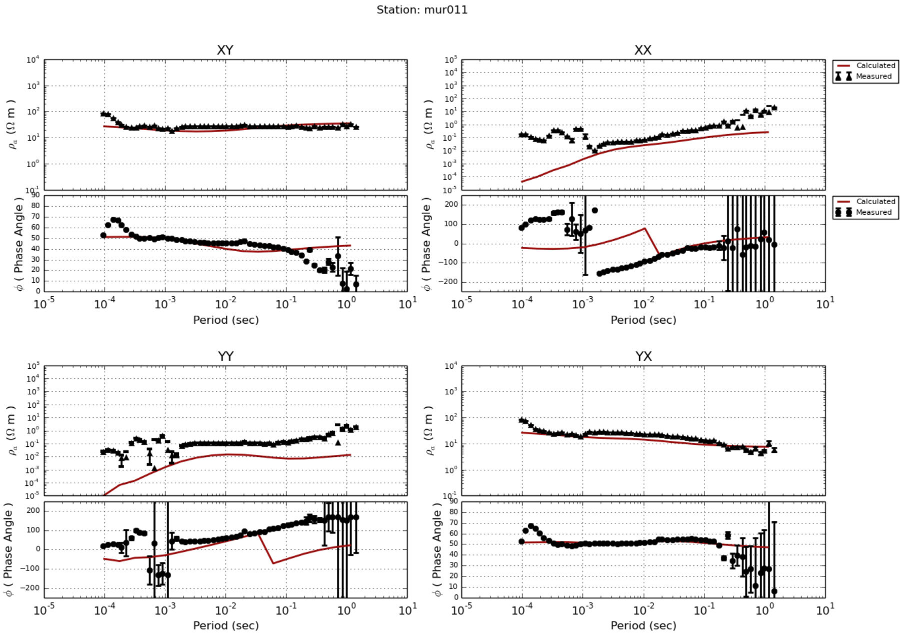

Figure A.11. Apparent resistivity and phase fitting curves of station MUR011, attained from WSINV3DMT for all components.

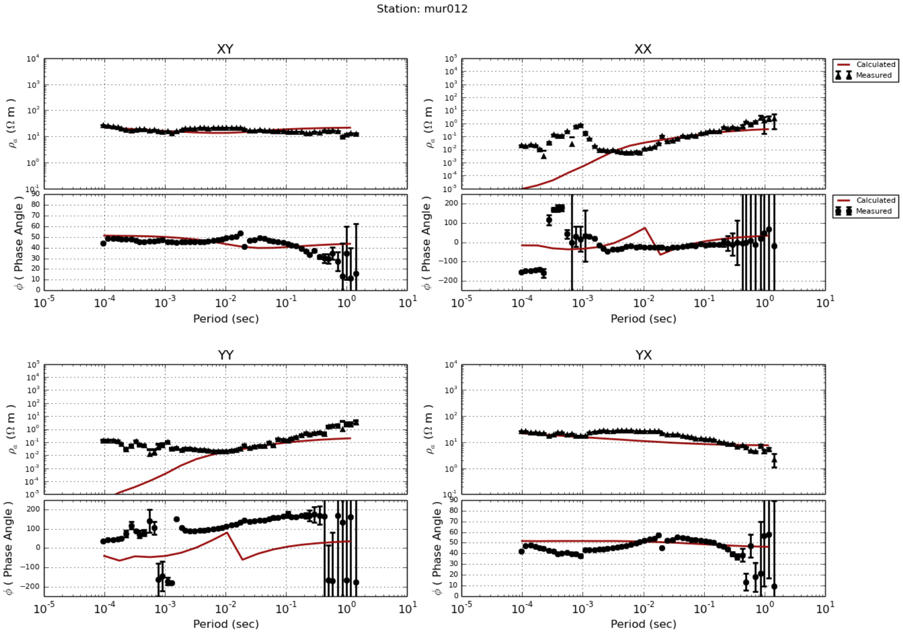

Figure A.12. Apparent resistivity and phase fitting curves of station MUR0012, attained from WSINV3DMT for all components.

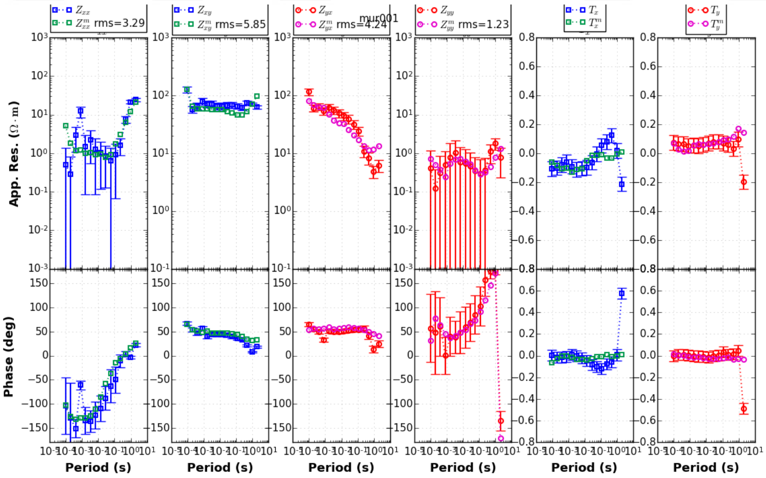

Figure A.13. Apparent resistivity and phase fitting curves of station MUR001, attained from ModEM for all components.

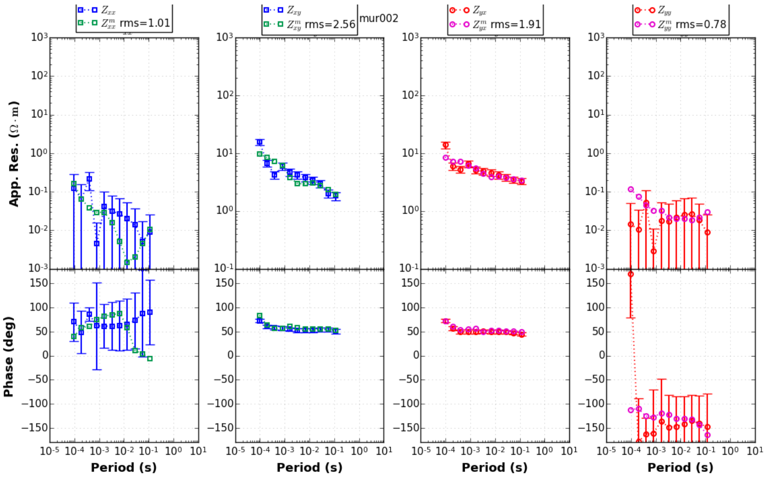

Figure A.14. Apparent resistivity and phase fitting curves of station MUR002, attained from ModEM for all components.

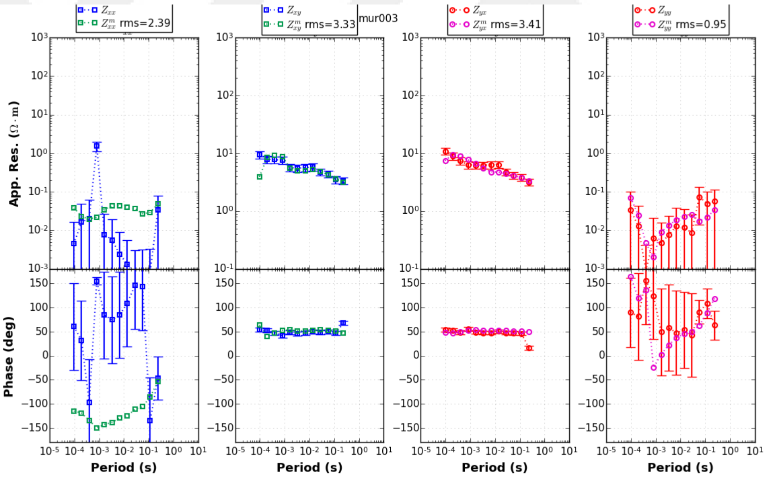

Figure A.15. Apparent resistivity and phase fitting curves of station MUR003, attained from ModEM for all components.

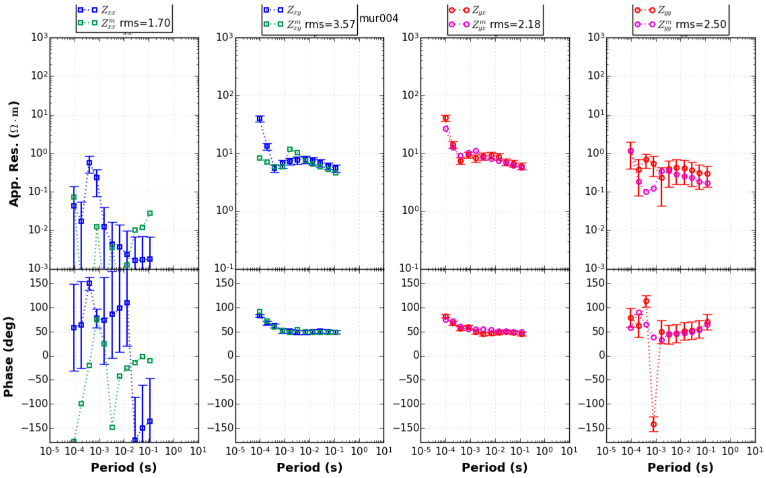

Figure A.16. Apparent resistivity and phase fitting curves of station MUR004, attained from ModEM for all components.

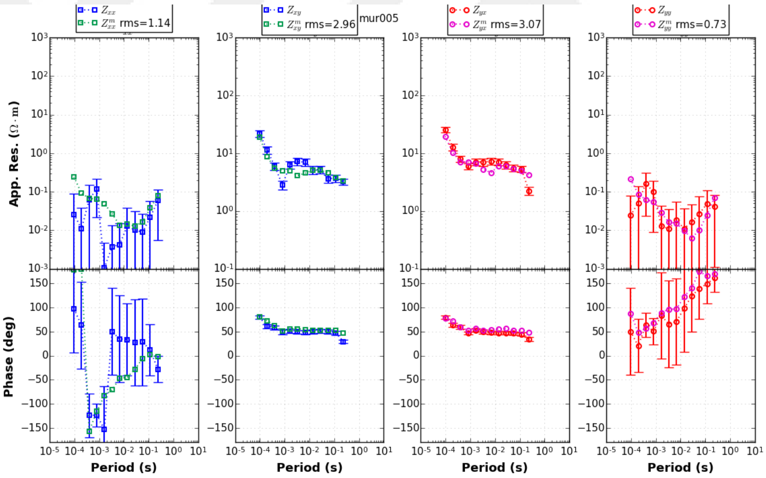

Figure A.17. Apparent resistivity and phase fitting curves of station MUR005, attained from ModEM for all components.

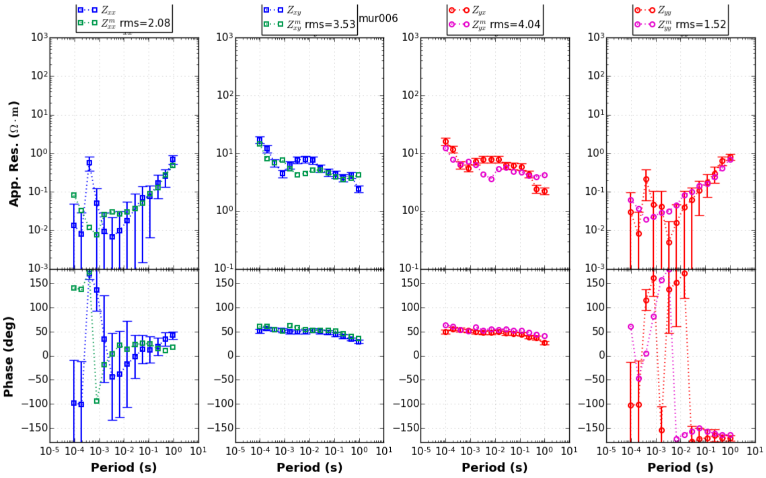

Figure A.18. Apparent resistivity and phase fitting curves of station MUR006, attained from ModEM for all components.

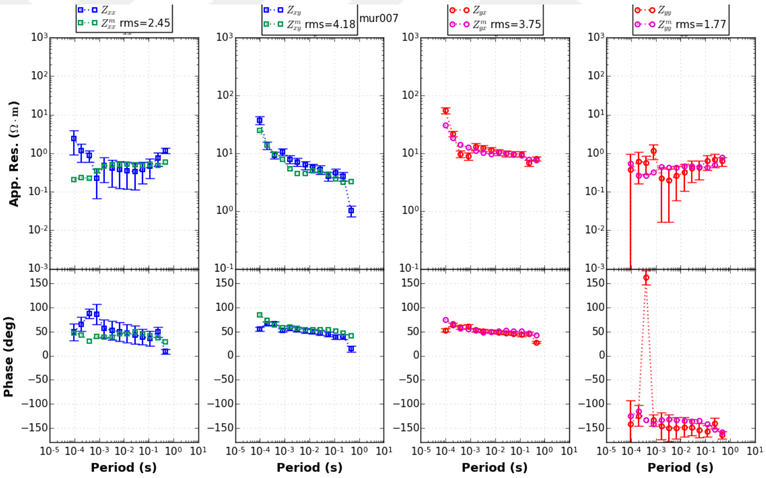

Figure A.19. Apparent resistivity and phase fitting curves of station MUR007, attained from ModEM for all components.

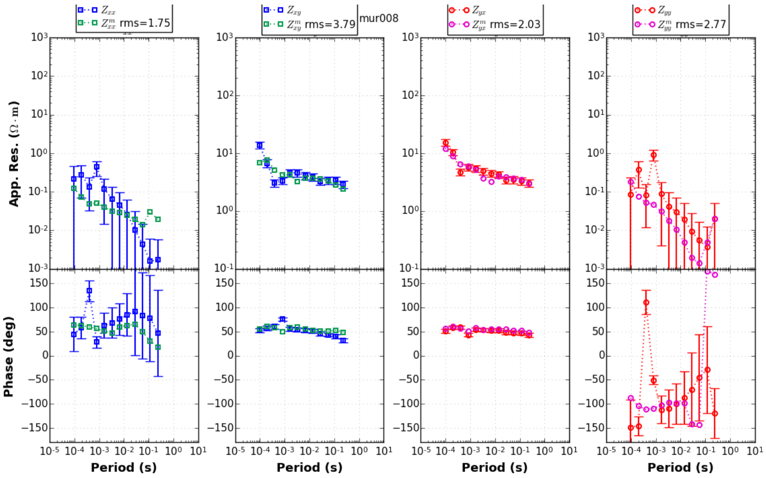

Figure A.20. Apparent resistivity and phase fitting curves of station MUR008, attained from ModEM for all components.

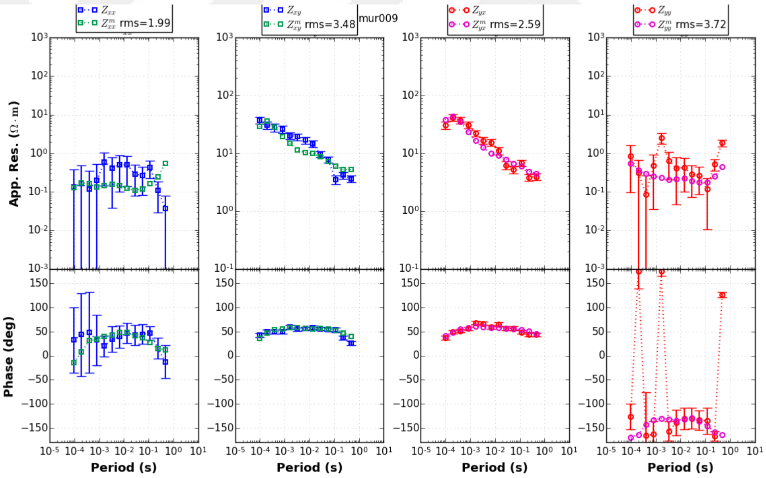

Figure A.21. Apparent resistivity and phase fitting curves of station MUR009, attained from ModEM for all components.

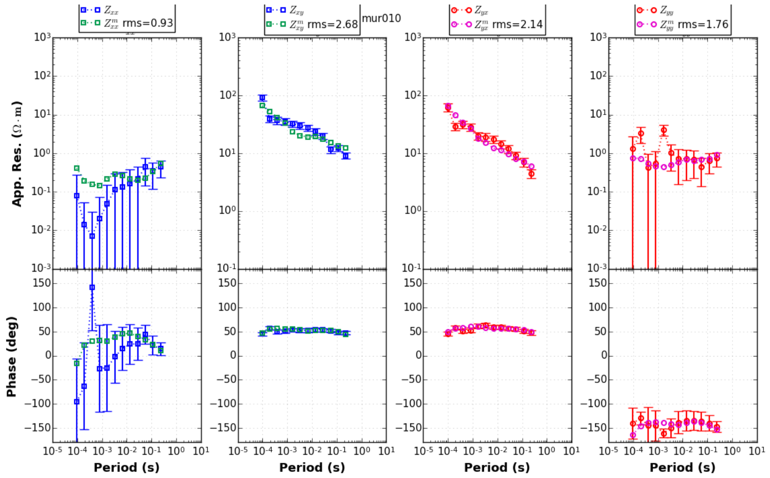

Figure A.22. Apparent resistivity and phase fitting curves of station MUR010, attained from ModEM for all components.

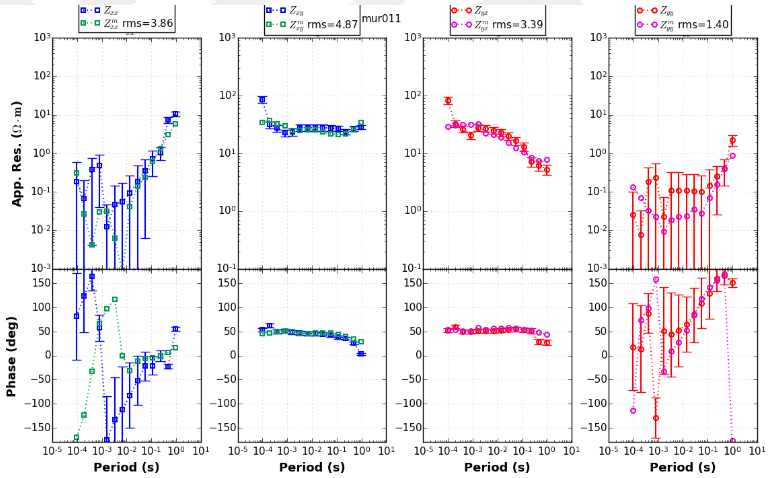

Figure A.23. Apparent resistivity and phase fitting curves of station MUR011, attained from ModEM for all components.

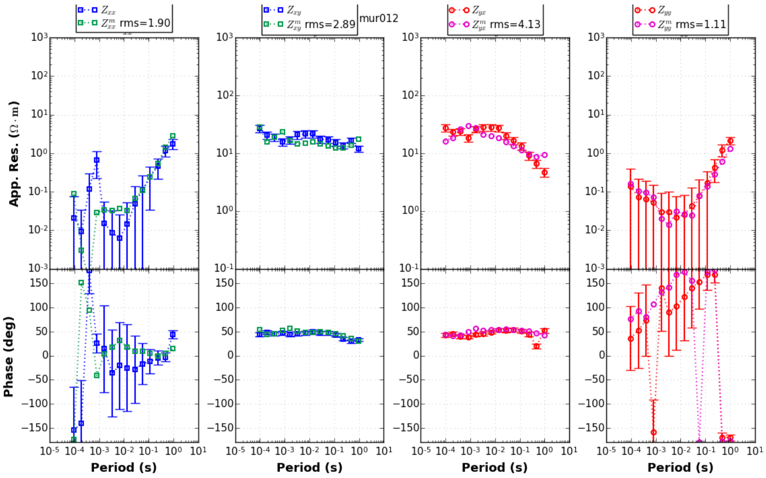

Figure A.24. Apparent resistivity and phase fitting curves of station MUR0012, attained from ModEM for all components.

APPENDIX B: FITTING CURVES OF WIDE-BAND MT DATA FOR THREE-DIMENSIONAL MODELING

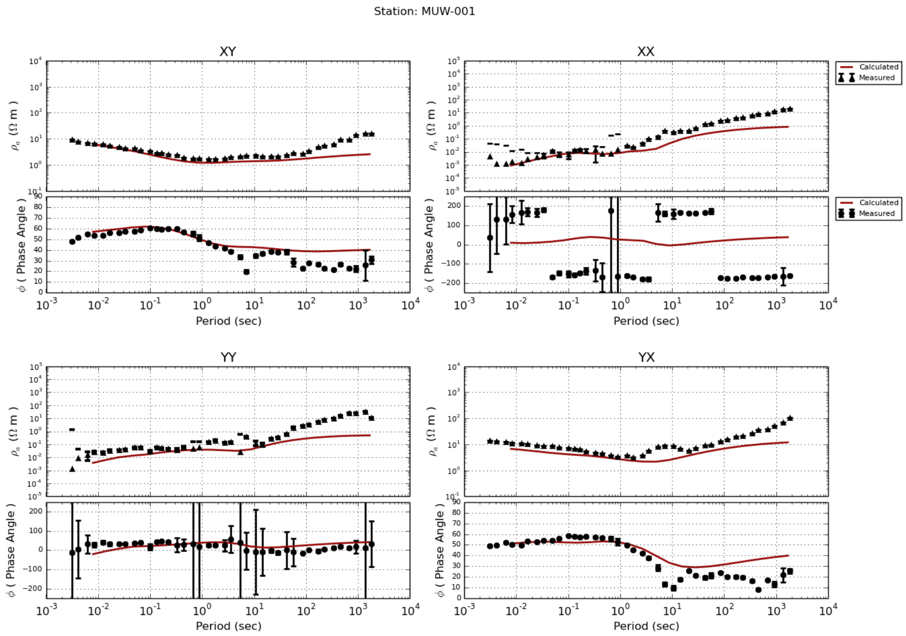

Figure B.1. Apparent resistivity and phase fitting curves of station MUW-001, attained from WSINV3DMT for all components.

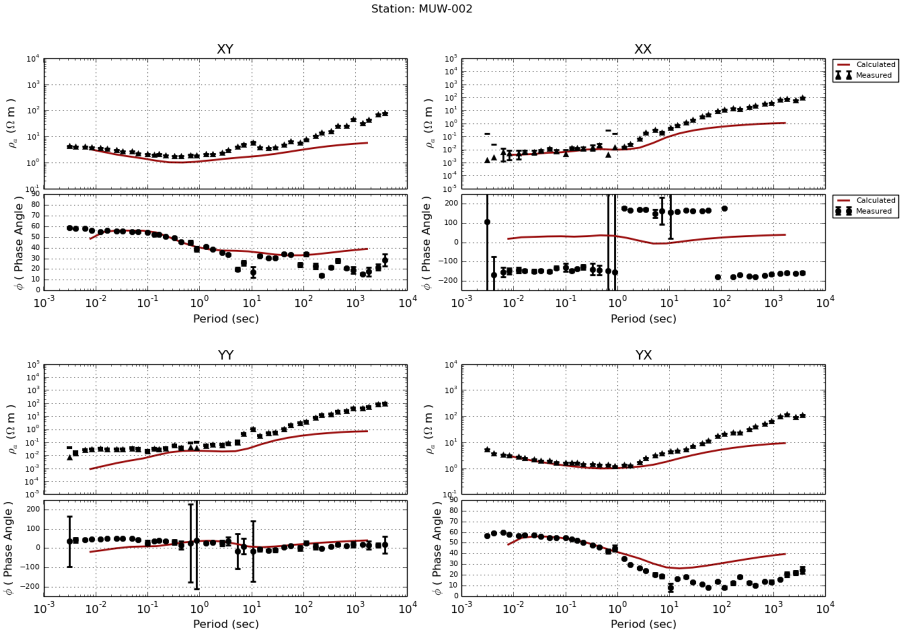

Figure B.2. Apparent resistivity and phase fitting curves of station MUW-002, attained from WSINV3DMT for all components.

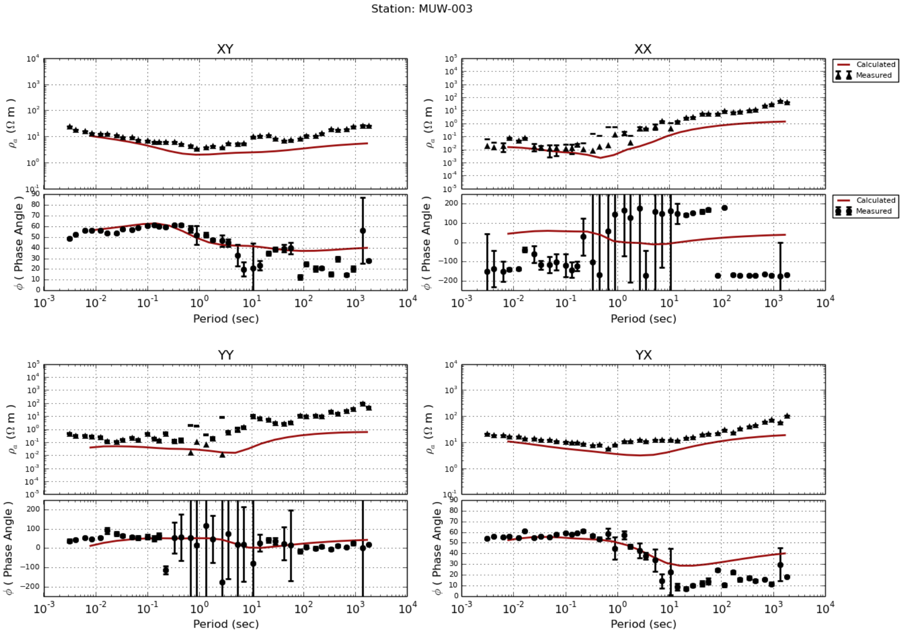

Figure B.3. Apparent resistivity and phase fitting curves of station MUW-003, attained from WSINV3DMT for all components.

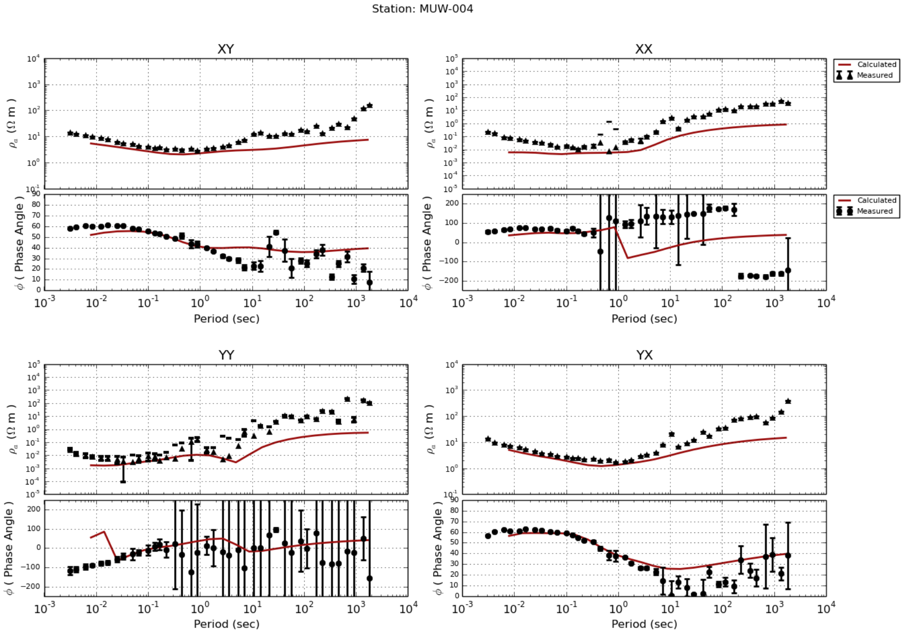

Figure B.4. Apparent resistivity and phase fitting curves of station MUW-004, attained from WSINV3DMT for all components.

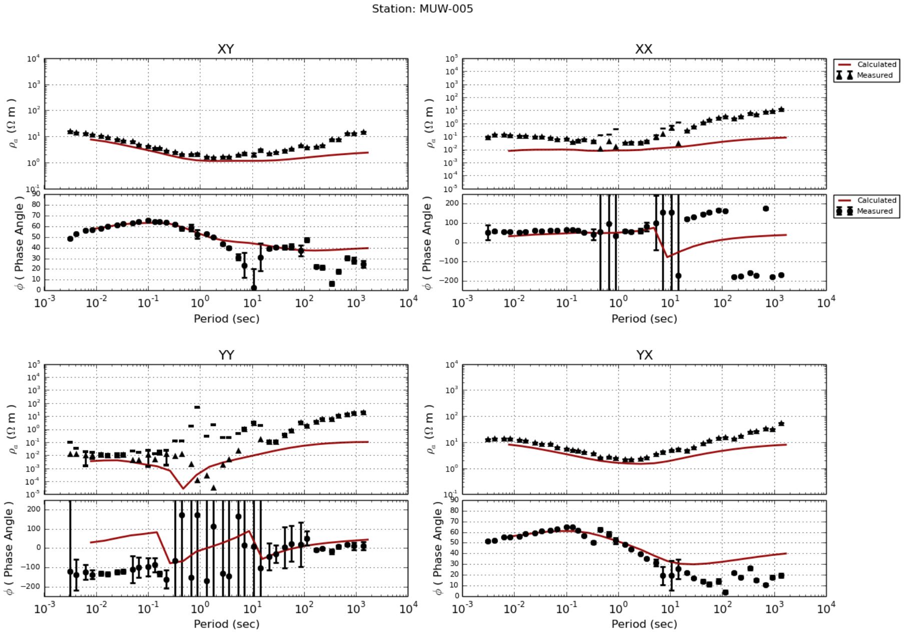

Figure B.5. Apparent resistivity and phase fitting curves of station MUW-005, attained from WSINV3DMT for all components.

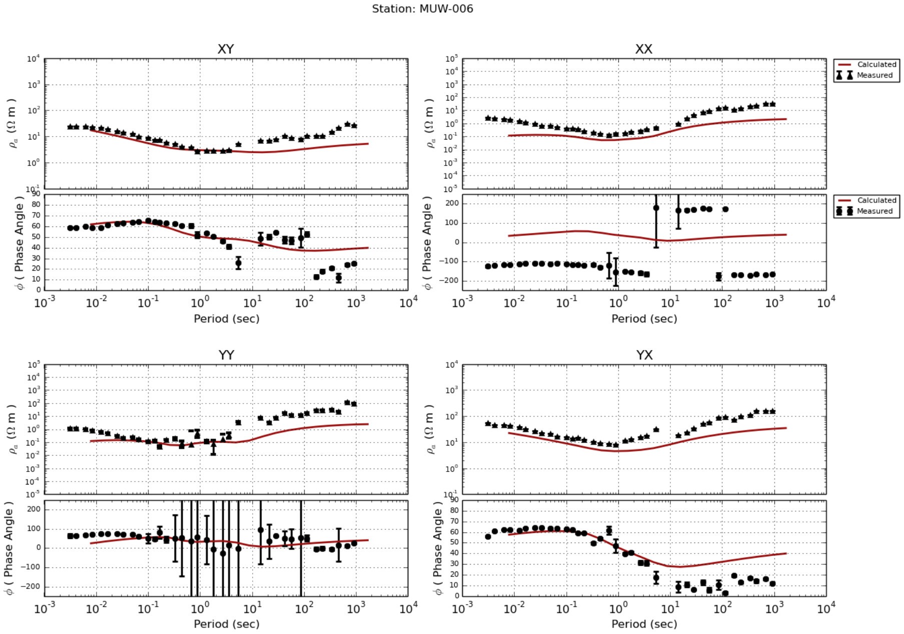

Figure B.6. Apparent resistivity and phase fitting curves of station MUW-006, attained from WSINV3DMT for all components.

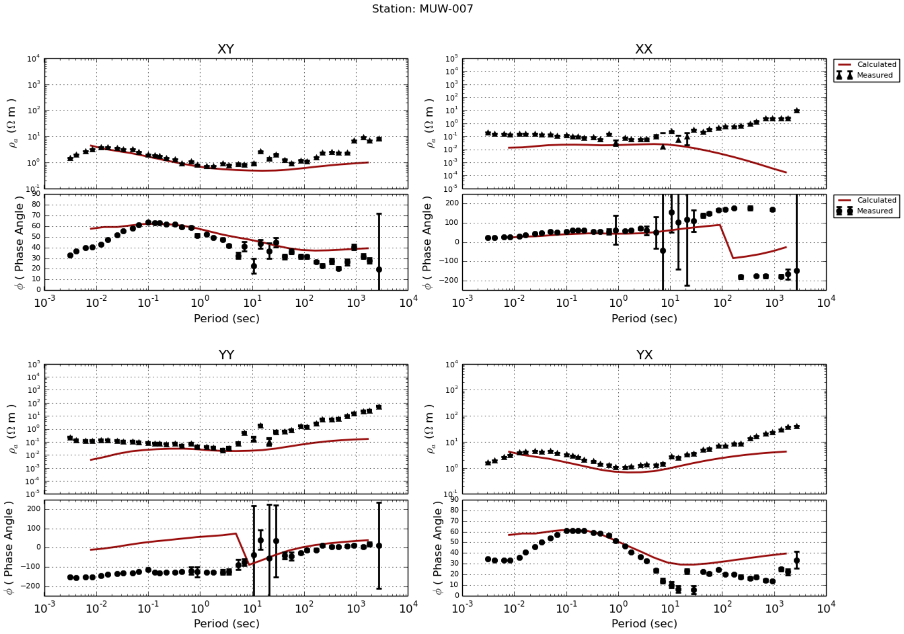

Figure B.7. Apparent resistivity and phase fitting curves of station MUW-007, attained from WSINV3DMT for all components.

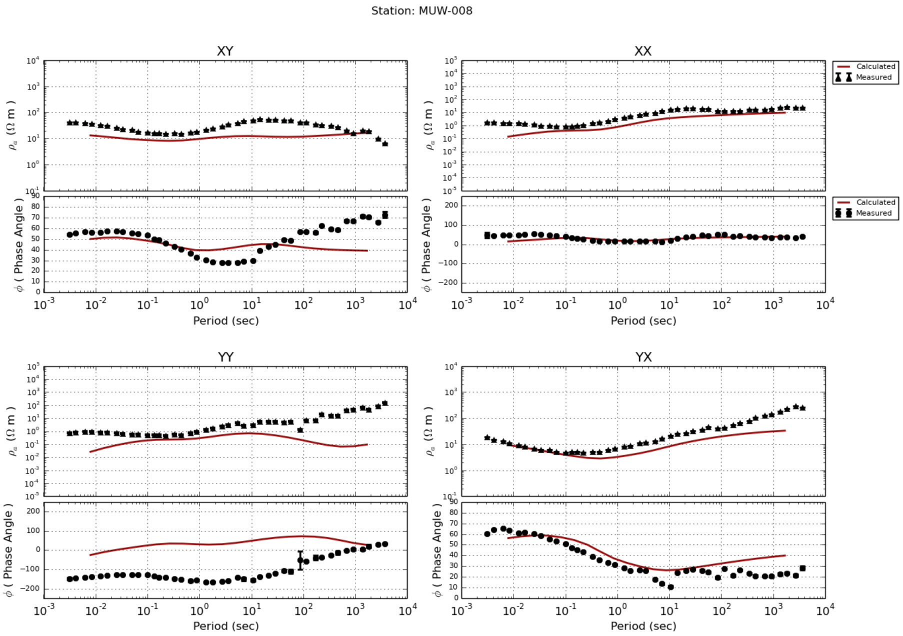

Figure B.8. Apparent resistivity and phase fitting curves of station MUW-008, attained from WSINV3DMT for all components.

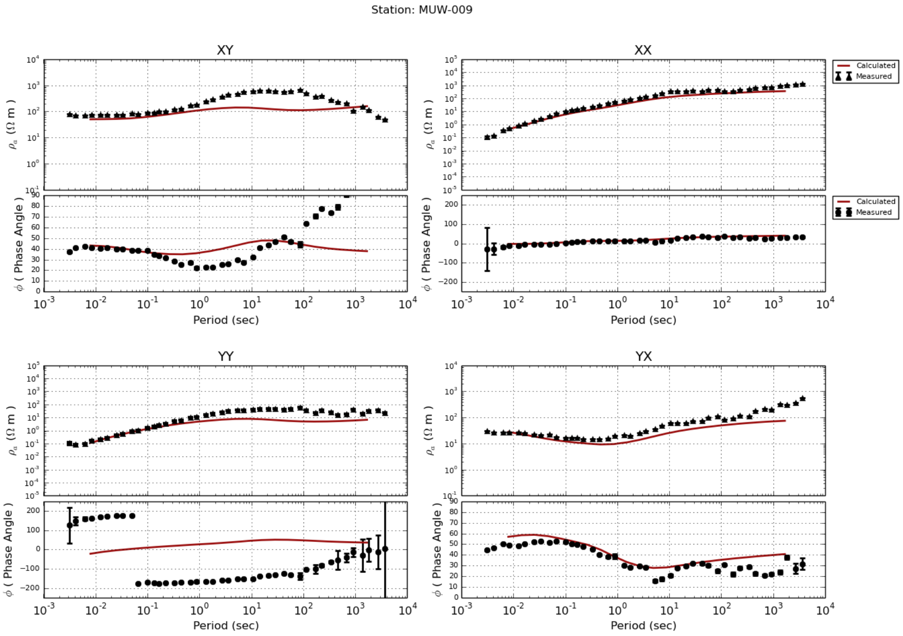

Figure B.9. Apparent resistivity and phase fitting curves of station MUW-009, attained from WSINV3DMT for all components.

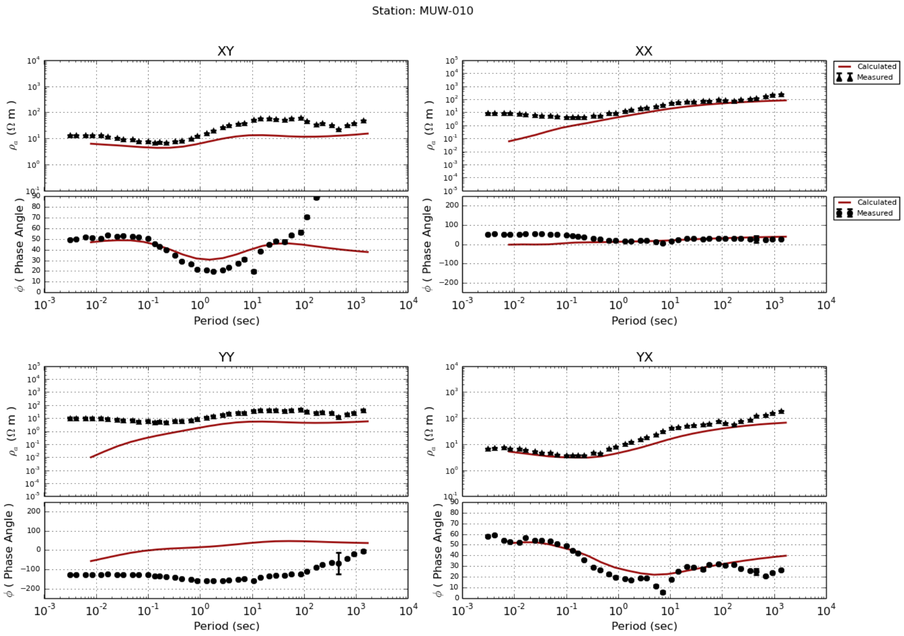

Figure B.10. Apparent resistivity and phase fitting curves of station MUW-010, attained from WSINV3DMT for all components.

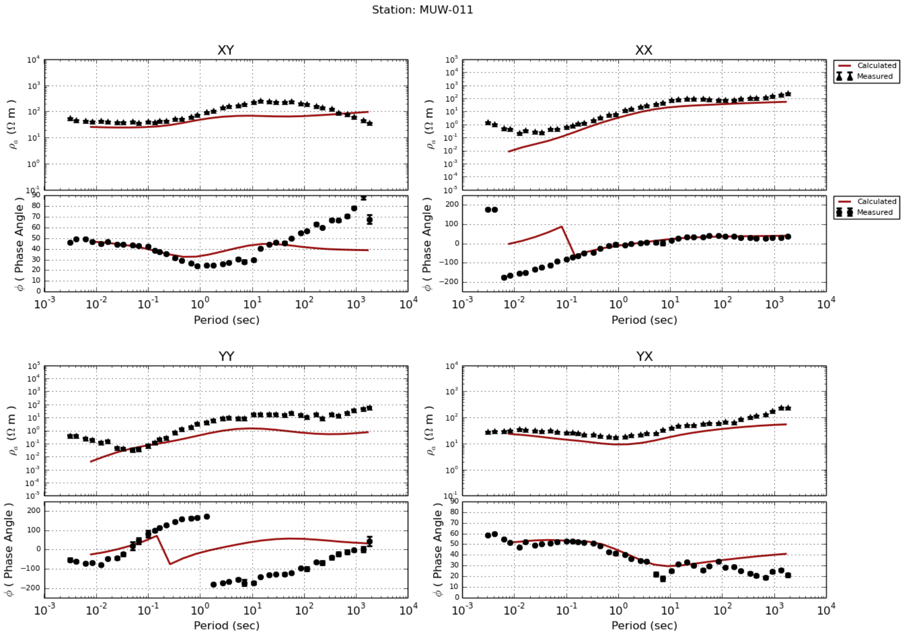

Figure B.11. Apparent resistivity and phase fitting curves of station MUW-011, attained from WSINV3DMT for all components.

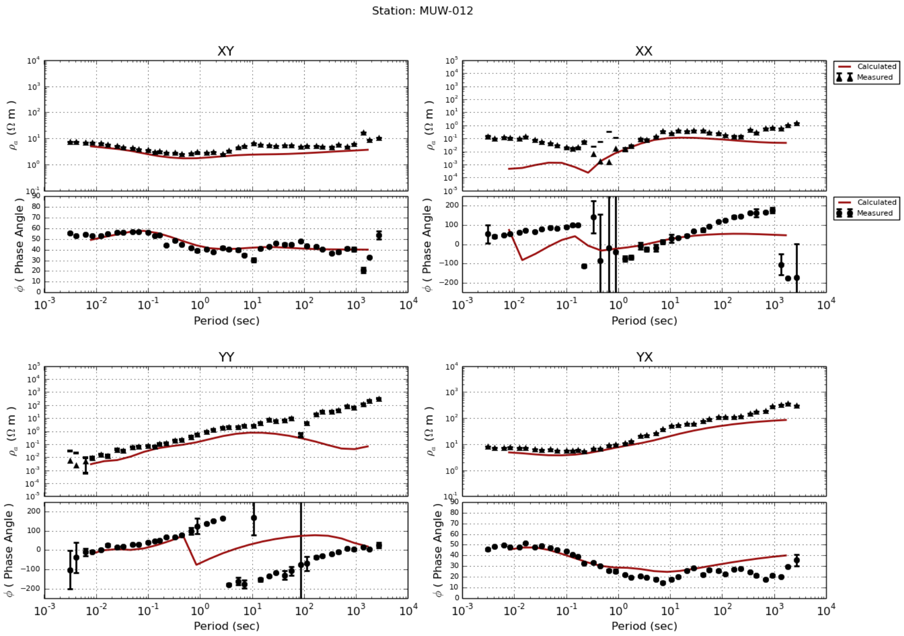

Figure B.12. Apparent resistivity and phase fitting curves of station MUW-012, attained from WSINV3DMT for all components.

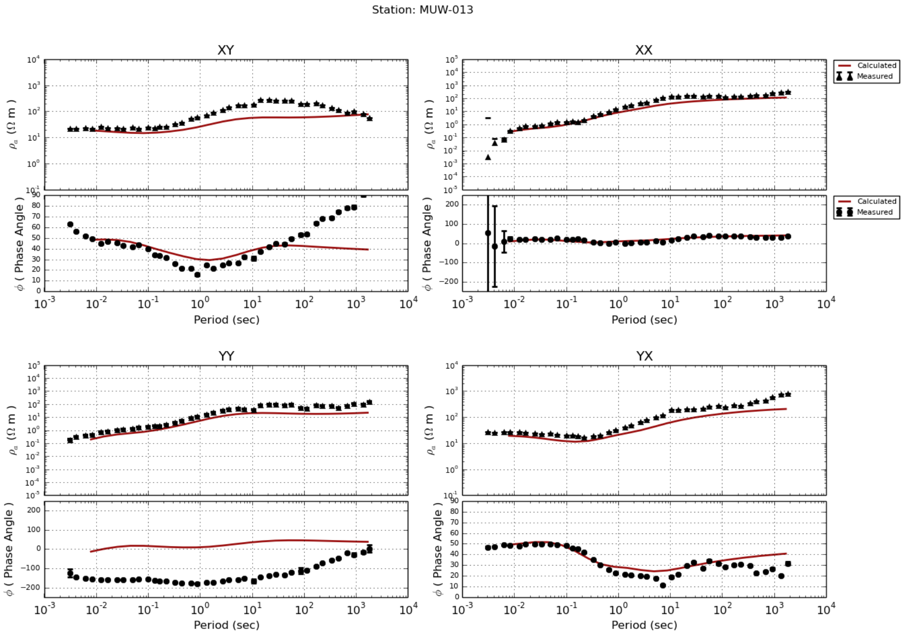

Figure B.13. Apparent resistivity and phase fitting curves of station MUW-013, attained from WSINV3DMT for all components.

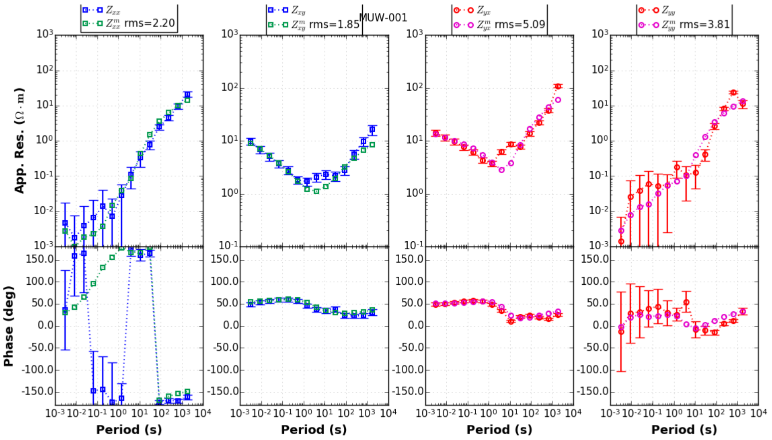

Figure B.14. Apparent resistivity and phase fitting curves of station MUW-001, attained from ModEM for all components.

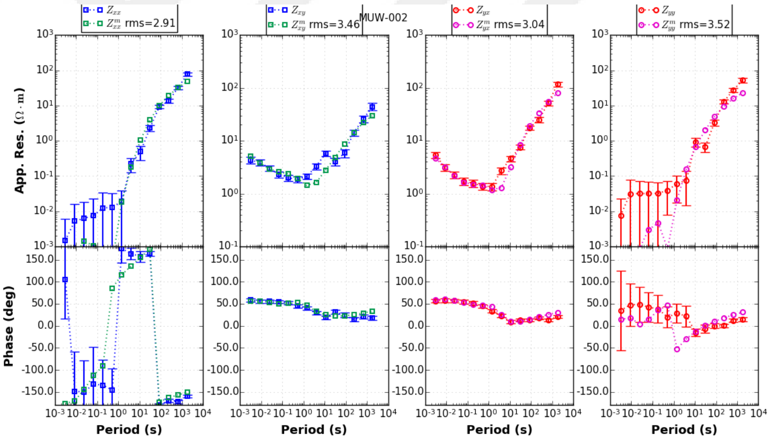

Figure B.15. Apparent resistivity and phase fitting curves of station MUW-002, attained from ModEM for all components.

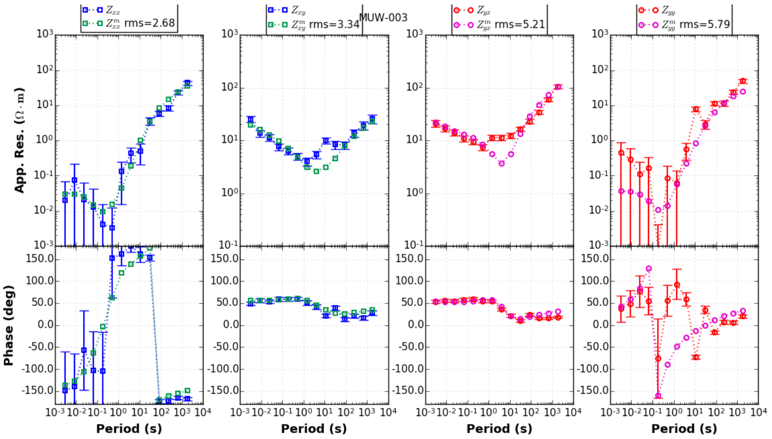

Figure B.16. Apparent resistivity and phase fitting curves of station MUW-003, attained from ModEM for all components.

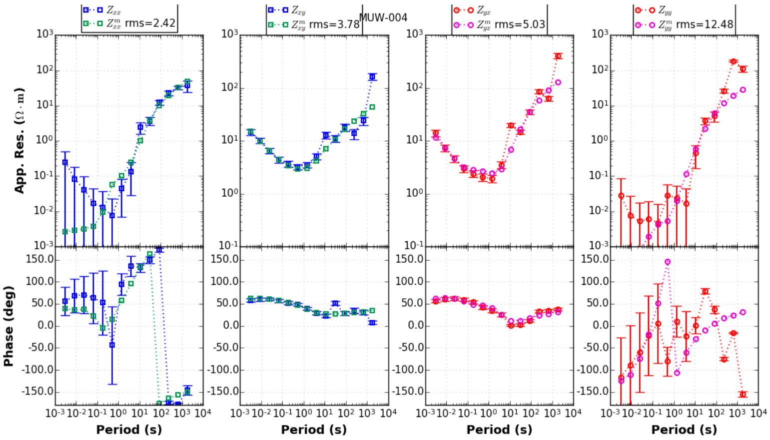

Figure B.17. Apparent resistivity and phase fitting curves of station MUW-004, attained from ModEM for all components.

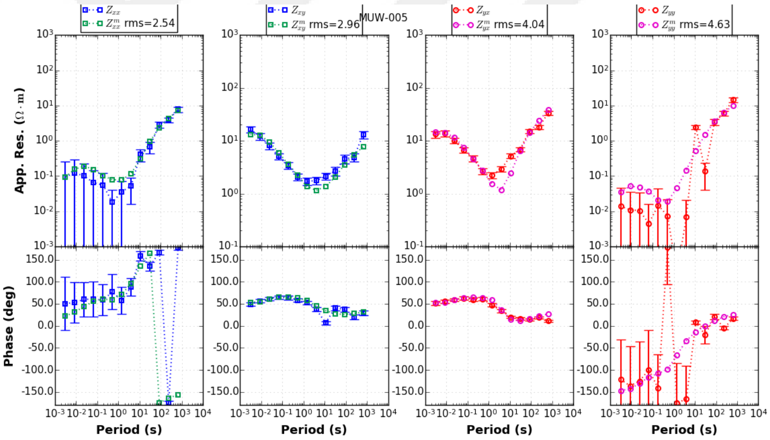

Figure B.18. Apparent resistivity and phase fitting curves of station MUW-005, attained from ModEM for all components.

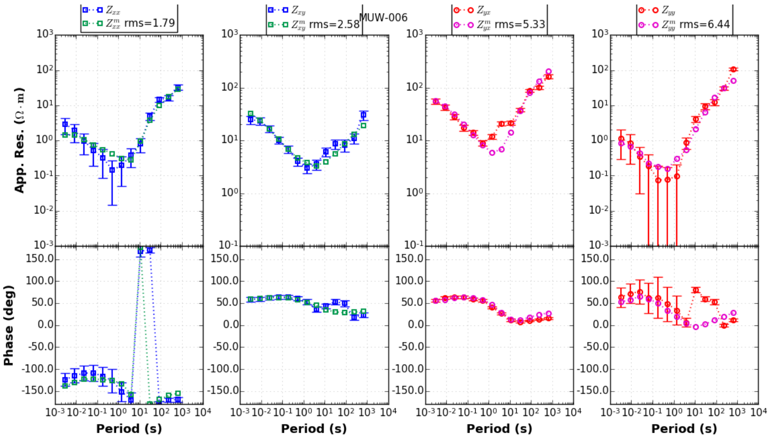

Figure B.19. Apparent resistivity and phase fitting curves of station MUW-006, attained from ModEM for all components.

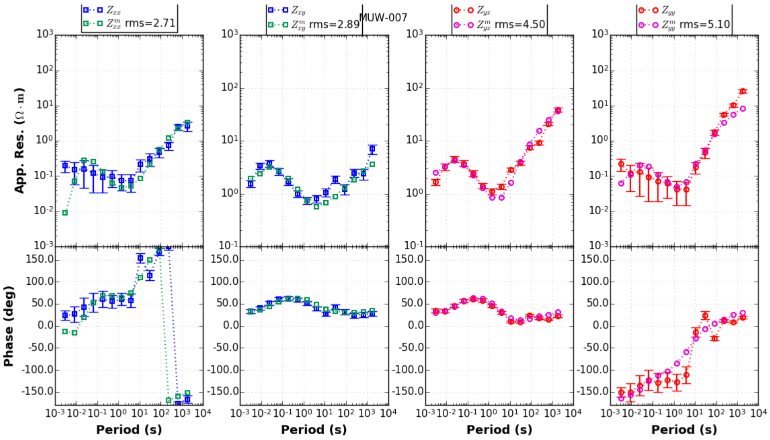

Figure B.20. Apparent resistivity and phase fitting curves of station MUW-007, attained from ModEM for all components.

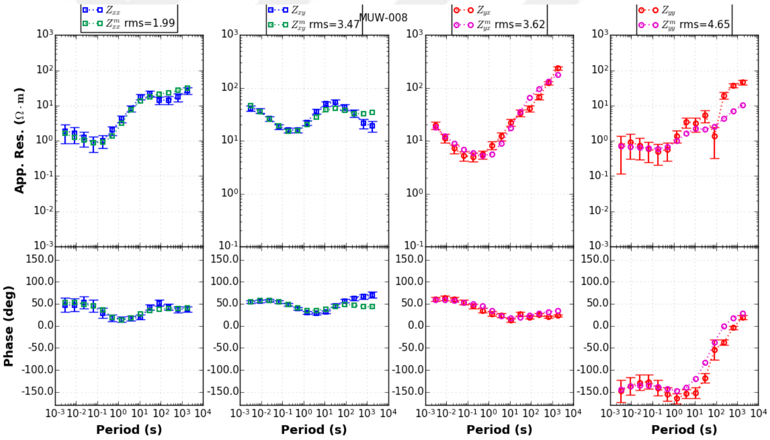

Figure B.21. Apparent resistivity and phase fitting curves of station MUW-008, attained from ModEM for all components.

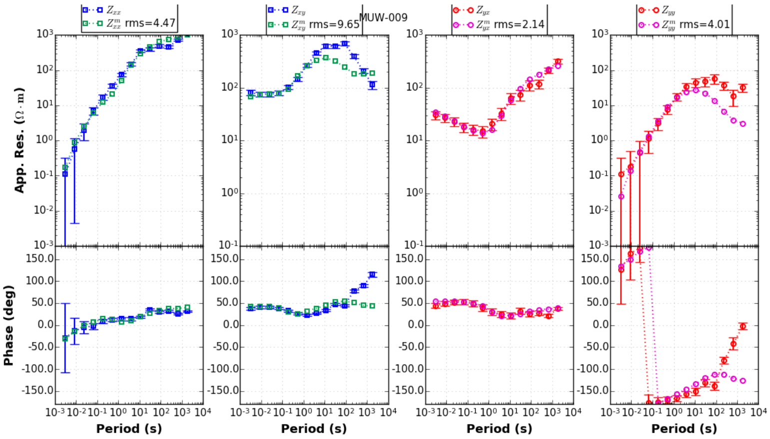

Figure B.22. Apparent resistivity and phase fitting curves of station MUW-009, attained from ModEM for all components.

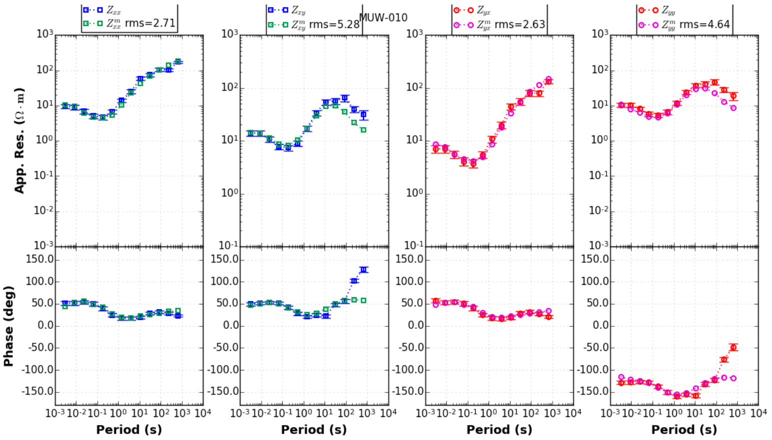

Figure B.23. Apparent resistivity and phase fitting curves of station MUW-010, attained from ModEM for all components.

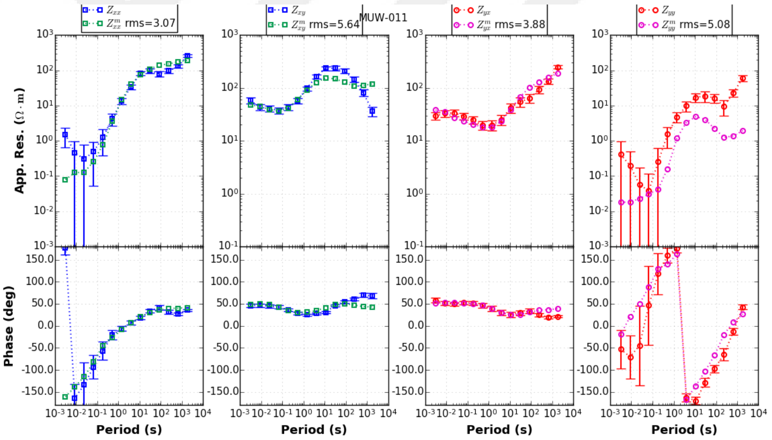

Figure B.24. Apparent resistivity and phase fitting curves of station MUW-011, attained from ModEM for all components.

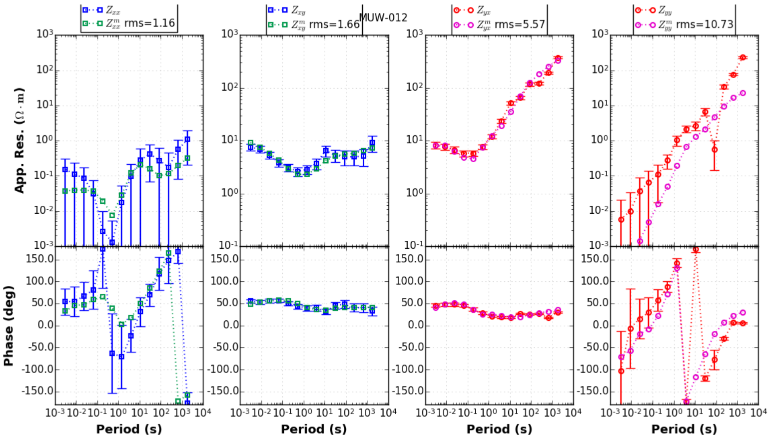

Figure B.25. Apparent resistivity and phase fitting curves of station MUW-012, attained from ModEM for all components.

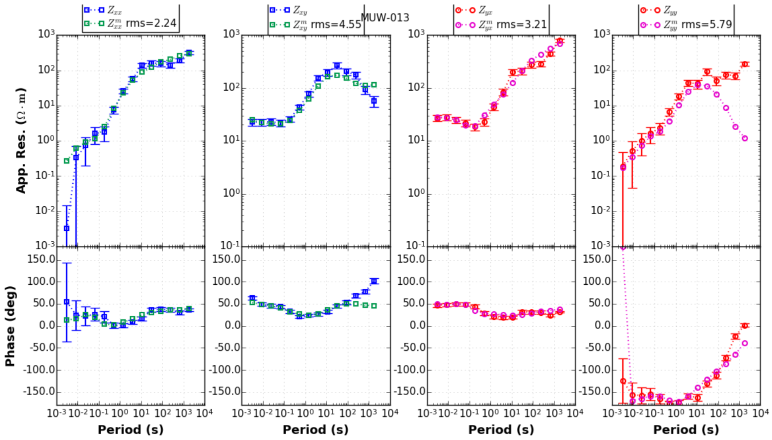

Figure B.26. Apparent resistivity and phase fitting curves of station MUW-013, attained from ModEM for all components.

REFERENCES

Aksoy, M. E., M. Meghraoui, M. Vallée, and Z. Çakır, "Rupture characteristics of the AD 1912 Mürefte (Ganos) earthquake segment of the North Anatolian fault (western Turkey)", *Geology*, 38(11), 991-994, 2010.

Ambraseys, N. N., and C.F. Finkel, “The Saros–Marmara earthquake of 9 August 1912”, *Earthquake engineering and structural Dynamics*, 15(2), 189-211, 1987.

Ambraseys, N., “The seismic activity of the Marmara Sea region over the last 2000 years”, *Bulletin of the Seismological Society of America*, 92(1), 1-18, 2002.

Becken, M., O. Ritter, S. K. Park, P. A. Bedrosian, U. Weckmann, and M. Weber, “A deep crustal fluid channel into the San Andreas Fault system near Parkfield, California”, *Geophysical Journal International*, 173(2), 718-732, 2008.

Becken, M., O. Ritter, P. A. Bedrosian, and U. Weckmann, “Correlation between deep fluids, tremor and creep along the central San Andreas fault”, *Nature*, 480(7375), 87-90, 2011.

Becken, M., and O. Ritter, “Magnetotelluric studies at the San Andreas Fault Zone: implications for the role of fluids” *Surveys in geophysics*, 33(1), 65-105, 2012.

Bedrosian, P. A., M. J. Unsworth, and G. Egbert, “Magnetotelluric imaging of the creeping segment of the San Andreas Fault near Hollister”, *Geophysical Research Letters*, 29(11), 2002.

Bedrosian, P. A., M. J. Unsworth, G.D. Egbert, and C. H. Thurber, “Geophysical images of the creeping segment of the San Andreas fault: implications for the role of crustal fluids in the earthquake process”, *Tectonophysics*, 385(1), 137-158, 2004.

Bedrosian, P. A., "MT+, integrating magnetotellurics to determine earth structure, physical state, and processes", *Surveys in geophysics*, 28(2-3), 121-167, 2007.

Berdichevskiĭ, M. N., and M. S. Zhdanov, *Advanced theory of deep geomagnetic sounding* (No. 19). Elsevier Science Ltd., 1984.

Bott, M. H. P., "Interior of the earth: its structure, constitution and evolution", *Interior of the earth: its structure, constitution and evolution., by Bott, MHP. Second edition. London (UK): Edward Arnold*, 416 p., 1, 1982.

Brodsky, E. E., and H. Kanamori, "Elastohydrodynamic lubrication of faults", *Journal of Geophysical Research: Solid Earth*, 106(B8), 16357-16374, 2001.

Byerlee, J. D., "Model for episodic flow of high-pressure water in fault zones before earthquakes", *Geology*, 21(4), 303-306, 1993.

Caine, J. S., J. P. Evans, and C. B. Forster, "Fault zone architecture and permeability structure", *Geology*, 24(11), 1025-1028, 1996.

Cagniard, L., "Basic theory of the magneto-telluric method of geophysical prospecting", *Geophysics*, 18(3), 605-635, 1953.

Caldwell, T. G., H. M. Bibby, and C. Brown, C, "The magnetotelluric phase tensor", *Geophysical Journal International*, 158(2), 457-469, 2004.

Cavazza, W., A. I. Okay, and M. Zattin, "Rapid early-middle Miocene exhumation of the Kazdağ Massif (western Anatolia)", *International Journal of Earth Sciences*, 98(8), 1935-1947, 2009.

Chave, A. D., and A. G. Jones, *The magnetotelluric method: Theory and practice*, Cambridge University Press, 2012.

Constable, S. C., R. L. Parker, and C. G. Constable, “Occam’s inversion: A practical algorithm for generating smooth models from electromagnetic sounding data”, *Geophysics*, 52(3), 289-300, 1987.

Egbert, G. D., and A. Kelbert, “Computational recipes for electromagnetic inverse problems”, *Geophysical Journal International*, 189(1), 251-267, 2012.

Electromagnetic Research Group for the Active Fault, “Low electrical resistivity along an active fault”, *Journal of Geomagnetism and Geoelectricity*, 34, 103–127, 1982.

Evans, J. P., “Thickness-displacement relationships for fault zones”, *Journal of Structural Geology*, 12(8), 1061-1065, 1990.

Faulkner, D. R., A.C. Lewis, and E. H. Rutter, “On the internal structure and mechanics of large strike-slip fault zones: field observations of the Carboneras fault in southeastern Spain”, *Tectonophysics*, 367(3), 235-251, 2003.

Gamble, T., W. M. Goubau, and J. Clarke, “Magnetotellurics with a remote magnetic reference”, *Geophysics*, 44(1), 53-68, 1979.

Goto, T. N., Y. Wada, N. Oshiman, and N. Sumitomo, “Resistivity structure of a seismic gap along the Atotsugawa Fault, Japan”, *Physics of the Earth and Planetary Interiors*, 148(1), 55-72, 2005.

Groom, R. W., and R. C. Bailey, “Decomposition of magnetotelluric impedance tensors in the presence of local three-dimensional galvanic distortion”, *Journal of Geophysical Research: Solid Earth*, 94(B2), 1913-1925, 1989.

Gürer, A., and M. Bayrak, “Relation between electrical resistivity and earthquake generation in the crust of West Anatolia, Turkey”, *Tectonophysics*, 445(1), 49-65, 2007.

Hickman, S., R. Sibson, and R. Bruhn, “Introduction to special section: Mechanical involvement of fluids in faulting”, *Journal of Geophysical Research: Solid Earth*, 100(B7), 12831-12840, 1995.

Hoffmann-Rothe, A., O.Ritter, and C. Janssen, “Correlation of electrical conductivity and structural damage at a major strike-slip fault in northern Chile”, *Journal of Geophysical Research: Solid Earth*, 109(B10), 2004.

Honkura, Y., A. M. Işikara, N. Oshiman, A. Ito, B. Üçer, Ş. Bariş, M. K. Tunçer, M. Matsushima, R. Pektaş, C. Çelik, S. B. Tank, F. Takahashi, M. Nakanishi, R. Yoshimura, Y. Ikeda, and T. Komut, “Preliminary results of multidisciplinary observations before, during and after the Kocaeli (Izmit) earthquake in the western part of the North Anatolian Fault Zone”, *Earth, planets and space*, 52(4), 293-298, 2000.

Honkura, Y., N. Oshiman, M. Matsushima, Ş. Barış, M. K. Tunçer, S. B. Tank, C. Çelik, and E. T. Çiftçi, “Rapid changes in the electrical state of the 1999 Izmit earthquake rupture zone”, *Nature communications*, 4, 2013.

Irwin, W. P., and I. Barnes, “Effect of geologic structure and metamorphic fluids on seismic behavior of the San Andreas fault system in central and northern California”, *Geology*, 3(12), 713-716, 1975.

Janssen, C., M. Bohnhoff, Y. Vapnik, E. Görgün, F. Bulut, B. Plessen, D. Pohl, M. Aktar, A. I. Okay, and G. Dresen, ”Tectonic evolution of the Ganos segment of the North Anatolian Fault (NW Turkey)”, *Journal of Structural Geology*, 31(1), 11-28, 2009.

Jiracek, G. R., “Geoelectromagnetics charges on”, *Reviews of geophysics*, 33(S1), 169-176, 1995.

Johnson, P. A., and T. V. McEvilly, (1995). “Parkfield seismicity: Fluid-driven?”, *Journal of Geophysical Research: Solid Earth*, 100(B7), 12937-12950, 1995.

Jones, F. W., and A.T. Price, “The perturbations of alternating geomagnetic fields by conductivity anomalies”, *Geophysical Journal International*, 20(3), 317-334, 1970.

Jödicke, H., “Water and graphite in the Earth’s crust—an approach to interpretation of conductivity models”, *Surveys in Geophysics*, 13(4-5), 381-407, 1992.

Kalafat, D., . *Study of the tectonic structures in Anatolian based on fault mechanism solutions*, Ph.D. Thesis, University of Istanbul, 217 pp. (in Turkish), 1995.

Kaufman, A. A. and G. V. Keller, *The magnetotelluric sounding method*, Elsevier, Amsterdam, 1981.

Kaya, T., S. B. Tank, M. K. Tunçer, I. I. Rokoityansky, E. Tolak, and T. Savchenko, “Asperity along the North Anatolian Fault imaged by magnetotellurics at Düzce, Turkey”, *Earth, planets and space*, 61(7), 871-884, 2009.

Kaya, T., T. Kasaya, S. B. Tank, Y. Ogawa, M. K. Tunçer, N. Oshiman, Y. Honkura, and M. Matsushima, “Electrical characterization of the North Anatolian Fault Zone underneath the Marmara Sea, Turkey by ocean bottom magnetotellurics”, *geophysical journal international*, ggt025, 2013.

Krieger, L., and J. R. Peacock, “MTpy: A Python toolbox for magnetotellurics”, *Computers and Geosciences*, 72, 167-175, 2014.

Ledo, J., P. Queralt, and J. Pous, “Effects of galvanic distortion on magnetotelluric data over a three-dimensional regional structure”, *Geophysical Journal Internationa*l, 132(2), 295-301, 1998.

Ledo, J., “2-D versus 3-D magnetotelluric data interpretation”, *Surveys in Geophysics*, 26(5), 511-543, 2005.

Madden, T., and P. Nelson, “A defense of Cagniard’s magnetotelluric method, *Magnetotelluric methods*, 89-102, 1964.

McNeice, G. W., and A. G. Jones, “Multisite, multifrequency tensor decomposition of magnetotelluric data”, *Geophysics*, 66(1), 158-173, 2001.

Meghraoui, M., M. E. Aksoy, H. S. Akyüz, M. Ferry, A. Dikbaş, and E. Altunel, “Paleoseismology of the North Anatolian fault at Güzelköy (Ganos segment, Turkey): Size and recurrence time of earthquake ruptures west of the Sea of Marmara”, *Geochemistry, Geophysics, Geosystems*, 13(4), 2012.

Meqbel, N., U. Weckmann, G. Muñoz, and O. Ritter, “Crustal metamorphic fluid flux beneath the Dead Sea Basin: Constraints from 2D and 3D magnetotelluric modelling”, *Geophysical Journal International*, ggw359, 2016.

Mitsuhata, Y., Y. Ogawa, M. Mishina, T. Kono, T. Yokokura, and T. Uchida, “Electromagnetic heterogeneity of the seismogenic region of 1962 M6. 5 Northern Miyagi Earthquake, northeastern Japan”, *Geophys. Res. Lett*, 28(23), 4371-4374, 2001.

Motagh, M., J. Hoffmann, B. Kampes, M. Baes, and J. Zschau, “Strain accumulation across the Gazikoy–Saros segment of the North Anatolian Fault inferred from Persistent Scatterer Interferometry and GPS measurements”, *Earth and Planetary Science Letters*, 255(3), 432-444, 2007.

Ogawa, Y., and T. Uchida, “A two-dimensional magnetotelluric inversion assuming Gaussian static shift”, *Geophysical Journal International*, 126(1), 69-76, 1996.

Ogawa, Y., M. Mishina, T. Goto, H. Satoh, N. Oshiman, T. Kasaya, Y. Takahashi, T. Nishitani, S. Sakanaka, M. Uyeshima, Y. Takahashi, Y. Honkura, and M. Matsushima, "Magnetotelluric imaging of fluids in intraplate earthquake zones, NE Japan back arc", *Geophys. Res. Lett*, 28(19), 3741-3744, 2001.

Okay, A. I., E. Demirbağ, H. Kurt, N. Okay, and İ. Kuşçu, "An active, deep marine strike-slip basin along the North Anatolian Fault in Turkey", *Tectonics*, 18(1), 129-147, 1999.

Okay, A. I., O. Tüysüz, and Ş. Kaya, "From transpression to transtension: changes in morphology and structure around a bend on the North Anatolian Fault in the Marmara region", *Tectonophysics*, 391(1), 259-282, 2004.

Okay, A. I., E. Özcan, W. Cavazza, N. Okay, and G. Less, "Basement types, Lower Eocene series, Upper Eocene olistostromes and the initiation of the southern Thrace Basin, NW Turkey", *Turkish Journal of Earth Sciences*, 19(1), 1-25, 2010.

Oshiman, N., Y. Honkura, M. Matsushima, S. Baris, C. Celik, M. K. Tuncer, and A. M. Isikara, "Deep resistivity structure around the fault associated with the 1999 Kocaeli earthquake, Turkey", *Seismotectonics in Convergent Plate Boundary*, 293-303, 2002.

Özcan, E., G. Less, A. I. Okay, M. Báldi-Beke, K. Kollányi, and İ. Ö. Yılmaz, "Stratigraphy and larger foraminifera of the Eocene shallow-marine and olistostromal units of the southern part of the Thrace Basin, NW Turkey", *Turkish Journal of Earth Sciences*, 19(1), 27-77, 2010.

Öztürk, Y. K., N. M. Özel, and A. D. Özbakir, "States of local stresses in the Sea of Marmara through the analysis of large numbers of small earthquakes", *Tectonophysics*, 665, 37-57, 2015.

Parkinson, W. D., "Directions of rapid geomagnetic fluctuations", *Geophysical Journal International*, 2(1), 1-14, 1959.

Parsons, T., S. Toda, R. S. Stein, A. Barka, and J. H. Dieterich, “Heightened odds of large earthquakes near Istanbul: An interaction-based probability calculation”, *Science*, 288(5466), 661-665, 2000.

Price, A. T., “The theory of magnetotelluric methods when the source field is considered”, *Journal of Geophysical Research*, 67, 1907-1918, 1962.

Rodi, W., and R. L. Mackie, “Nonlinear conjugate gradients algorithm for 2-D magnetotelluric inversion”, *Geophysics*, 66(1), 174-187, 2001.

Rikitake, T., “Note on the electromagnetic induction within the earth”, *Bull. Earthq. Res. Inst., Univ. Tokyo*, 24, 1–9, 1948.

Rikitake, T., “Westward drift of the equatorial component of the earth’s magnetic dipole”, *Journal of geomagnetism and geoelectricity*, 18(3), 383-392, 1966.

Ritter, O., A. Hoffmann-Rothe, P. A. Bedrosian, U. Weckmann, and V. Haak, “Electrical conductivity images of active and fossil fault zones”, *Geological Society, London, Special Publications*, 245(1), 165-186, 2005.

Rockwell, T., A. Barka, T. Dawson, S. Akyuz, and K. Thorup, “Paleoseismology of the Gazikoy-Saros segment of the North Anatolia fault, northwestern Turkey: Comparison of the historical and paleoseismic records, implications of regional seismic hazard, and models of earthquake recurrence”, *Journal of Seismology*, 5(3), 433-448.

Schulz, S. E., and J. P. Evans, “Mesoscopic structure of the Punchbowl Fault, Southern California and the geologic and geophysical structure of active strike-slip faults”, *Journal of Structural Geology*, 22(7), 913-930, 2000.

Schmucker, U., “Regional induction studies: a review of methods and results”, *Physics* *of the Earth and Planetary Interiors*, 7(3), 365-378, 1973.

Seeber, L., O. Emre, M. H. Cormier, C. C. Sorlien, C. M. G. McHugh, A. Polonia, N. Ozer, and N. Cagatay, “Uplift and subsidence from oblique slip: the Ganos–Marmara bend of the North Anatolian Transform, Western Turkey”, *Tectonophysics*, 391(1), 239-258, 2004.

Sengör, A. M. C., “The North Anatolian transform fault: its age, offset and tectonic significance”, *Journal of the Geological Society*, 136(3), 269-282, 1979.

Sengör, A. M. C., O. Tüysüz, C. Imren, M. Sakinç, H. Eyidogan, N. Görür, X. Le Pichon, and C. Rangin, “The North Anatolian fault: A new look”, *Annu. Rev. Earth Planet. Sci.*, 33, 37-112, 2005.

Simpson, F., and K. Bahr, *Practical magnetotellurics*, Cambridge University Press, 2005.

Siripunvaraporn, W., and G. Egbert, “An efficient data-subspace inversion method for 2-D magnetotelluric data”, *Geophysics*, 65(3), 791-803, 2000.

Siripunvaraporn, W., G. Egbert, Y. Lenbury, and M. Uyeshima, “Three-dimensional magnetotelluric inversion: data-space method”, *Physics of the Earth and planetary interiors*, 150(1), 3-14, 2005.

Siripunvaraporn, W., G. Egbert, and M. Uyeshima, “Interpretation of two-dimensional magnetotelluric profile data with three-dimensional inversion: synthetic examples”, *Geophysical Journal International*, 160(3), 804-814, 2005.

Siripunvaraporn, W., “Three-dimensional magnetotelluric inversion: an introductory guide for developers and users”, *Surveys in Geophysics*, 33(1), 5-27, 2012.

Swift Jr. C. M., *A magnetotelluric investigation of an electrical conductivity anomaly in the southwestern United States*, Ph.D. Thesis, Massachusetts Inst. of Tech. Cambridge Geophysics Lab., 1967.

Tank, S. B., Y. Honkura, Y. Ogawa, N. Oshiman, M. K. Tunçer, M. Matsushima, C. Çelik, E. Tolak, E., and A. M. Işıkara, "Resistivity structure in the western part of the fault rupture zone associated with the 1999 Izmit earthquake and its seismogenic implication", *Earth, planets and space*, 55(7), 437-442, 2003.

Tank, S. B., Y. Honkura, Y. Ogawa, M. Matsushima, N. Oshiman, M. K. Tunçer, C. Çelik, E. Tolak, E., and A. M. Işıkara, "Magnetotelluric imaging of the fault rupture area of the 1999 Izmit (Turkey) earthquake", *Physics of the Earth and Planetary Interiors*, 150(1), 213-225, 2005.

Tank, S. B., "Fault zone conductors in Northwest Turkey inferred from audio frequency magnetotellurics" *Earth, planets and space*, 64(9), 729-742, 2012.

Thomas, A. M., R. M. Nadeau, and R. Bürgmann, "Tremor-tide correlations and near-lithostatic pore pressure on the deep San Andreas fault", *Nature*, 462(7276), 1048-1051, 2009.

Tikhonov, A. N., "On determining electrical characteristics of the deep layers of the Earth's crust". *In Doklady* (Vol. 73, No. 2, pp. 295-297), 1950.

Tikhonov, A. N., and V. I. Arsenin, *Solutions of ill-posed problems (Vol. 14)*, Washington, DC: Winston, 1977.

Türkoğlu, E., M. Unsworth, İ. Çağlar, V. Tuncer, and Ü. Avşar, "Lithospheric structure of the Arabia-Eurasia collision zone in eastern Anatolia: Magnetotelluric evidence for widespread weakening by fluids?", *Geology*, 36(8), 619-622, 2008.

Tüysüz, O., A. Barka, and E. Yiğitbaş, “Geology of the Saros graben and its implications for the evolution of the North Anatolian fault in the Ganos–Saros region, northwestern Turkey”, *Tectonophysics*, 293(1), 105-126, 1998.

Unsworth, M. J., P.E. Malin, G. D. Egbert, and J. R. Booker, “Internal structure of the San Andreas fault at Parkfield, California”, *Geology*, 25(4), 359-362, 1997.

Unsworth, M.J., G. Egbert, and J. Booker, “High-resolution electromagnetic imaging of the San Andreas fault in central California”. *Journal of Geophysical Research: Solid Earth*, 104(B1), 1131-1150, 1999.

Unsworth, M.J., P. Bedrosian, M. Eisel, G. Egbert, G., and W. Siripunvaraporn, “Along strike variations in the electrical structure of the San Andreas Fault at Parkfield, California”, *Geophysical Research Letters*, 27(18), 3021-3024, 2000.

Unsworth, M.J., and P. A. Bedrosian, “Electrical resistivity structure at the SAFOD site from magnetotelluric exploration”, *Geophysical research letters*, 31(12), 2004.

Vozoff, K., “The magnetotelluric method in the exploration of sedimentary basins”, *Geophysics*, 37(1), 98-141, 1972.

Vozoff, K., “The magnetotelluric method”, *in Nabighian, M. N., Ed.,Electromagnetic methods in applied Geophysics: Volume 2, Application, Parts A and B, SEG*, 641-711, 1991.

Wait, J. R., “On the relation between telluric currents and the earth’s magnetic field”, *Geophysics*, 19, 281-289, 1954.

Wannamaker, P. E., T. G. Caldwell, W. M. Doerner, and G. R. Jiracek, “Fault zone fluids and seismicity in compressional and extensional environmen inferred from electrical conductivity: the New Zealand Southern Alps and US Great Basin”, *Earth, planets* *and space*, 56(12), 1171-1176, 2004.

Wannamaker, P. E., T. G. Caldwell, G. R. Jiracek, V. Maris, G. J. Hill, Y. Ogawa, H. M. Bibby, S. L. Bennie, and W. Heise, “Fluid and deformation regime of an advancing subduction system at Marlborough, New Zealand”, *Nature*, 460(7256), 733-736, 2009.

Ward, S. E., and G. W. Hohmann, ”Electromagnetic Theory for Geophysical Applications”, *Electromagnetic Methods in Applied Geophysics Vol.1*, pp. 130-311, 1987.

Weckmann, U., O. Ritter, and V. Haak, “A magnetotelluric study of the Damara Belt in Namibia: 2. MT phases over 90 reveal the internal structure of the Waterberg Fault/Omaruru Lineament”, *Physics of the Earth and Planetary Interiors*, 138(2), 91-112, 2003.

Weidelt, P., “The inverse problem of geomagnetic induction”, *J. Geophys.*, 38, 257-289, 1972.

Wiese, H., “Geomagnetische Tiefentellurik Teil II: die Streichrichtung der Untergrundstrukturen des elektrischen Widerstandes, erschlossen aus geomagnetischen Variationen”, *Pure and applied geophysics*, 52(1), 83-103, 1962.

Yaltırak, C., and B. Alpar, “Kinematics and evolution of the northern branch of the North Anatolian Fault (Ganos Fault) between the Sea of Marmara and the Gulf of Saros”, *Marine Geology*, 190(1), 351-366, 2002.

Zattin, M., A. I. Okay, and W. Cavazza, “Fission-track evidence for late Oligocene and mid-Miocene activity along the North Anatolian Fault in south-western Thrace” *Terra Nova*, 17(2), 95-101, 2005.

Zhang, X., D. J. Sanderson, and A. J. Barker, “Numerical study of fluid flow of deforming fractured rocks using dual permeability model”, *Geophysical Journal International*, 151(2), 452-468, 2002.

Zhdanov, M. S., and G. V. Keller, *The geoelectrical methods in geophysical exploration (Vol. 31)* Elsevier Science Limited, 1994.